The Dissertation Committee for Michalis Hadjioannou Certifies that this is the approved version of the following dissertation:

Large-Scale Testing and Numerical Simulations of Composite Floor Slabs Under Progressive Collapse Scenarios

Committee:

Eric B. Williamson, Supervisor

Michael D. Engelhardt, Co-Supervisor

James O. Jirsa

Todd A. Helwig

Stelios Kyriakides

Large-Scale Testing and Numerical Simulations of Composite Floor Slabs Under Progressive Collapse Scenarios

by

Michalis Hadjioannou, Dipl.; M.S.E.

Dissertation

Presented to the Faculty of the Graduate School of

The University of Texas at Austin

in Partial Fulfillment

of the Requirements

for the Degree of

Doctor of Philosophy

The University of Texas at Austin

May 2015

Dedication

To my parents, for their love and support

Acknowledgements

This dissertation is the final product of continuous effort supported by a great number of people. Primarily, I would like to express my special thanks and appreciation to my supervisors Eric Williamson and Michael Engelhardt for giving me the opportunity to work on this research project. Their dedication and support of my efforts during the course of this research program and beyond is invaluable, and I have tremendously benefited from working with them, both as a researcher and as a person. They both acted as parents and provided me with lifelong lessons that will guide me in the future.

Special thanks to the other members of my committee, Todd Helwig, James Jirsa, and Stelios Kyriakides for their participation and for their valuable feedback throughout this project. Additionally, over the past five years, a number of graduate students participated in the research team, and their efforts have contributed to the successful completion of this work. Firstly, I would like to thank Sean Donahue who helped me to adjust smoothly to the research laboratory. His input on the design, erection, and testing of the large-scale specimens was very valuable. The generous help of George Moutsanidis at the laboratory, including the erection and testing of the specimens, is also greatly appreciated. Lindsay Hull's assistance with the instrumentation and testing should not go unmentioned. Thanks also to Will Shekarchi for helping with the construction, and Umit Can Oksuz who also contributed to the project.

Also thanks to other members of the research team; Hamed Zolghadr Jahromi, Izzudin Bassam, David Nethercor from Imperial College London, David Stevens and Kirk Marchand from Protection Engineering Consultants, and Mark Waggoner from Walter P. Moore, for their continuous support and for sharing their precious experience and knowledge.

For the financial support that made this project feasible, I would like to thank the Department of Homeland Security. I also want to honor the staff of the Ferguson Structural Engineering Laboratory. Without their help, this research project could not have been completed. Thanks to Andrew Valentine, Blake Stasney, David Bradley, Dennis Fillip, Eric Schell, and Mike Wason, who assisted me and provided their expertise to the benefit of the project.

Last but not least, I want to thank my friends and classmates who contributed in making my attendance at UT interesting and adventurous. I want to thank Kostas Belivanis for the countless hours of inspiring discussions on technical aspects of the project and beyond, George Zalachoris for his unlimited positive attitude during hard times, and Vasilis Samaras for his wise advice. Thanks also to Stergios Koutrouvelis and Apostolis Psaros for being supportive. I am also thankful to my old friend Margarita Takou who was always there to listen when I needed an ear. I also want to mention all my close overseas friends from Cyprus and Greece that were supportive all these years. Thank you all, I am proud that I have such great people around me. Without you, I would not have been able to fulfill my dreams and achieve my goals.

Large-Scale Testing and Numerical Simulations of Composite Floor Slabs Under Progressive Collapse Scenarios

Michalis Hadjioannou, Ph.D.

The University of Texas at Austin, 2015

Supervisors: Eric B. Williamson, Michael D. Engelhardt

Two full-scale composite floor slabs were tested at Ferguson Structural Engineering Laboratory at The University of Texas at Austin under two different column removal scenarios. The removal of a column and the associated response of a structure is an index of its resiliency under abnormal loads, such as those due to a terrorist attack or a vehicle collision. Previous computational studies have shown that floor slab contributions are extremely important in mitigating collapse, but the limited experimental data currently available provide inconsistent results. The aim of the experimental testing program was to identify basic behaviors of floor slabs and to estimate their ultimate capacity under the absence of a critical column. The two test specimens were representative of isolated sections of the gravity-load resisting system of a typical steel-framed building. Thus, all steel members were joined using simple connections. During testing, the critical column was statically removed under service loads. Next, the load on the floor slab was increased at a slow rate until the specimens completely collapsed. Overall, the ultimate load carrying capacity of the two specimens under the absence of a single column exceeded the required capacity from progressive collapse provisions.

Detailed finite element models were developed and validated against the collected experimental data in which all the components of the floor system were explicitly

modeled. The explicit nonlinear finite element software LS-DYNA® was employed to simulate the response of the experimental tests. Initially, individual components of the floor system were modeled and validated against experimental data available in the literature. The two specimens were modeled using a similar approach. The main components of the floor system were modeled using three-dimensional solid elements for the concrete and steel members, shell elements for the corrugated steel deck, and beam elements for the shear studs and reinforcement in the slab. Bolts and other connection components were explicitly modeled using solid elements, and contact was specified to account for the interaction among the connected parts. Good agreement was found between the tests and numerical simulations. Further analyses provided information about the sensitivity of the numerical models to several design parameters.

Table of Contents

List of Tables

List of Figures

CHAPTER 1

INTRODUCTION

1.1 INTRODUCTION

This dissertation documents an investigation into the response of steel-concrete composite floor systems following the loss of an individual column. Local failures to load-bearing components usually occur after abnormal loading, which can be due to such events as blast, collision, earthquake, or fire. These types of events are sometimes able to trigger progressive collapse in which local failures propagate to cause failure of neighboring components, which in turn may trigger other failures. Also failures of structural components are considered during the design of buildings that require enhanced structural resiliency, and special analysis methods are followed to evaluate their response after the failure of structural components.

This study is divided into two major parts: (1) large-scale physical testing of composite floor slabs and (2) high-fidelity modeling and simulation of composite floor slabs using the general purpose, multi-physics code LS-DYNA (Hallquist 2013). Two large-scale specimens were constructed and tested at the Ferguson Structural Engineering Laboratory (FSEL) at The University of Texas at Austin under an interior and an exterior (façade) column removal scenario. Detailed finite element (FE) models were developed and validated against the collected experimental data. Further analysis of the validated FE models provided information about influential parameters that affect response. The specimens were representative sections of typical composite floor systems with simple shear connections, commonly comprising the gravity load resisting system of steel-

framed buildings. The gravity columns in these buildings are relatively small compared to the columns of the lateral load resisting system because they are not designed for large flexural moments. Consequently, gravity columns may be more susceptible to damage than columns comprising the lateral force resisting system.

A description of composite floors, along with an introduction to extreme loading events and load redistribution are given in the subsequent sections. The motivation for this research study and a summary of the main objectives are presented subsequently. The last section provides a brief review of the remaining chapters of this dissertation.

1.1.1 Steel-Concrete Composite Floors

Floors in steel-framed buildings are typically made of cast-in-place concrete supported by steel beams. Steel decking is used as permanent formwork and as external reinforcement for the concrete slab. Additionally, non-structural reinforcement in the form of wire mesh is present to control concrete creep and shrinkage. Figure 1.1 shows the main components of a typical floor system. It is noted that the floor system described here has two levels of composite action; one is between the concrete slab and the steel beams and the other is between the concrete slab and the steel deck. The former is obtained using shear studs, and the latter is obtained from embossments in the steel deck. The beam-to-column connections are either simple shear connections or moment-resisting connections depending upon whether the frame is part of the gravity system or lateral system. In general, the vast majority of connections in a typical structure will be simple connections that are assumed to have negligible moment capacity (Hewitt 2006, Tamboli 2010).

Construction practices vary around the world. Typically, after the erection of the steel frame, the steel deck is placed over the steel grillage of the supporting beams as shown in Figure 1.2. The deck panels are fastened to the steel grillage with self-tapping screws or spot-welding (SDI 2006). Adjacent panels overlap on their perimeter and are attached to each other with similar fastening methods, creating side-laps and longitudinal-laps between the adjacent panels. Once the shear studs are welded through the deck to the top flange of the beams, the wire mesh reinforcement is placed over the entire area of the slab. Because each bay of the floor slab is typically designed assuming it is simply supported, limited cracking often develops at the ends of each bay due to the development of negative moments in the concrete topping, which is actually continuous over the floor system. To control the cracking in these regions, reinforcing bars are also placed close to the top face of the concrete slab. Finally, the concrete topping is cast.

The floor systems investigated in this dissertation are similar to the description given in this section. Other variations of composite floor systems exist, but they are beyond the scope of this study (Mullett 1998).

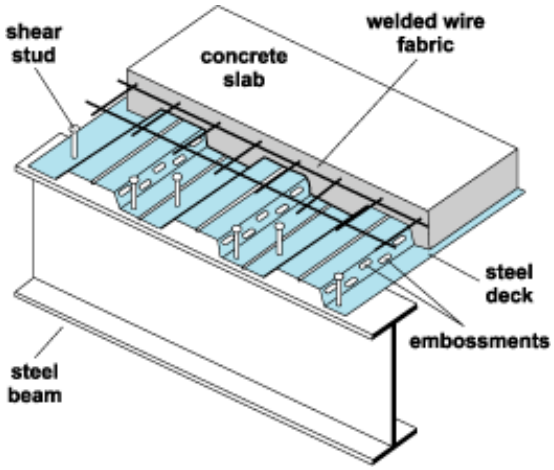

Figure 1.1: Components of a typical composite floor system (from Arthur and McGraw-Hill (2005))

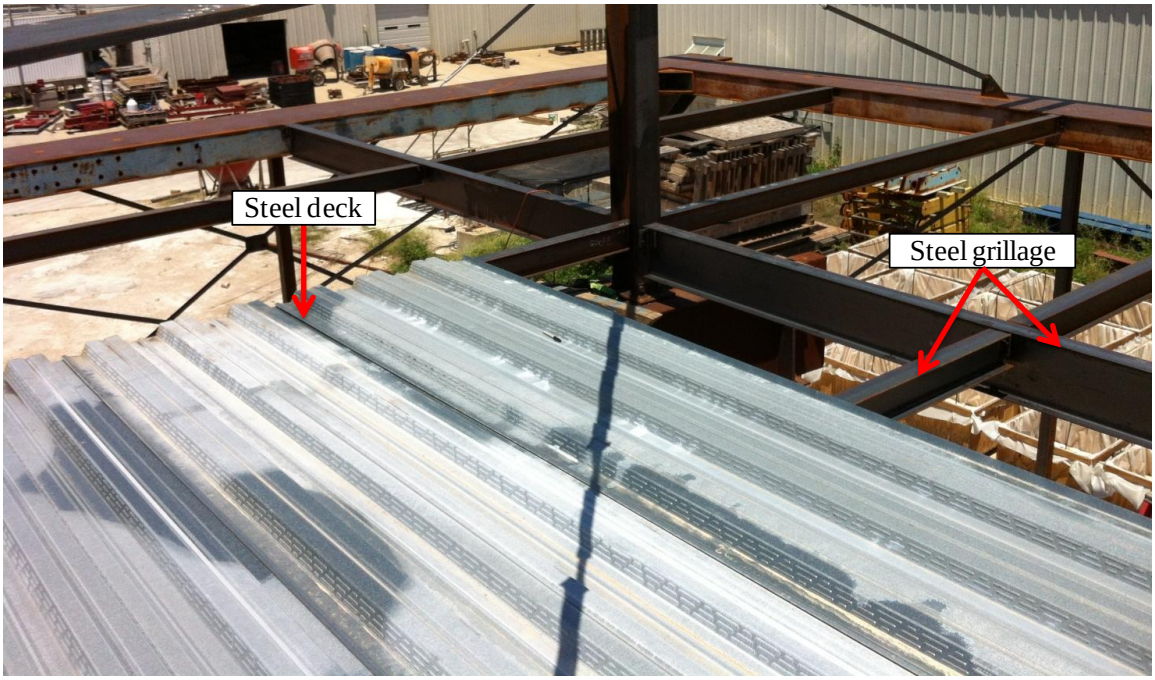

Figure 1.2: Placement of the steel deck over the steel grillage

1.1.2 Extreme Loading Events

The vulnerability of buildings to extreme loading events has increased in interest throughout the US and worldwide. These events include, but are not limited to, intentional blasts (e.g., malevolent bombings), unintentional blasts (e.g., gas pipeline explosions), and collisions with structural members. A common feature of these events is the localized damage to a relatively small portion of a building that causes failures to a few load-bearing members. The bombing of the Alfred P. Murrah Building in Oklahoma City in 1995 (FEMA 1996), the bombing of the US embassy in Nairobi in 1998, and the attack against the World Trade Center in New York in 2001 (Shyam-Sunder 2005) demonstrate that localized failures may propagate, resulting in collapse of a larger portion, if not the entire structure. Such propagating failure sequences are often described as *progressive collapse*. An alternative term is *disproportionate collapse* because of the disproportionality between the damage from the triggering event and the final damage. Figure 1.3 depicts the three initially damaged ground floor exterior columns on the north side of the Alfred P. Murrah Building in Oklahoma City. These columns were severely damaged from the detonation of an explosive device contained in a truck parked along the north side of the building. The quantity of explosives was estimated to be equivalent to 1820 kg of TNT (Sozen*, et al.* 1998). The initial damage propagated, causing the collapse of more than 50% of the building. Although such events occur rarely, the consequences are high, including fatalities and major financial loses.

The damage in such events occurs in two "phases." First, there is damage associated with the actual event (e.g., the damage caused from an airblast in the case of an explosion). The second phase includes the potential propagation of this damage to the

remaining portions of a structure, which might eventually cause progressive collapse. When such failures occur, most of the fatalities and financial losses are caused from the latter "phase" (FEMA 1996). As a result, eliminating the propagation of the initial localized damage is desirable.

Figure 1.3: Alfred P. Murah Building bombing in Oklahoma City, 1995 (FEMA 1996)

1.1.3 Load Redistribution

An essential behavior that follows the initial failure of a few load-bearing members is the redistribution of loads to the remaining portions of a building. Initially damaged load-bearing members may consist of one or a few columns. The loads previously carried by these columns must now follow an alternate load path through the adjacent structural members (i.e., beams and slabs). The beams framing into the damaged columns and the supported slabs are required to bridge over a larger span than originally configured and eventually transfer the loads to the intact columns of a structure. If the initially undamaged members have sufficient capacity to carry the extra loads,

progressive collapse may be arrested; otherwise, damage continues to propagate. An example where progressive collapse was arrested and the initial damage remained localized is the Bankers Trust Building (Wisniewski and Peraza 2008). Falling debris from the World Trade Center collapse in 2001 caused the loss of an exterior column on the north side of the building. As shown in Figure 1.4, the damage to the building was primarily caused by falling debris and did not propagate.

Figure 1.4: Bankers Trust Building damage, 2001 (FEMA 2002)

1.2 RESEARCH NEED AND OBJECTIVES

1.2.1 Research Need

Current design guides for progressive collapse mitigation, such as the Department of Defense criteria (DoD 2013) or the General Services Administration guidelines (GSA 2013), are believed to provide conservative design solutions. Engineers have been critical of these documents for being vague in terms of analyzing buildings for their progressive collapse potential. Part of the reason for this lack of clear guidance stems from the limited amount of experimental test data available on how structures perform following the failure of a critical component. Therefore, more experimental data should be obtained to provide a better understanding of the behavior of buildings under column loss scenarios. These data can be used to determine the suitability of existing design guidelines. Also, the DoD (2013) guidelines require that only 3D computational models be used for collapse evaluations. These models are usually more complex than the 2D models used in engineering practice. Consequently, validation of computational models against experimental data is required to ensure they provide acceptable predictions of the progressive collapse potential of buildings.

It is evident that during progressive collapse scenarios, floor slabs, beams, and columns all contribute to response. These three components participate in load redistribution from the damaged parts of a building to the intact portions. Characterization of contributions and mechanisms associated with the response of these structural elements will assist the efforts for the development of efficient and affordable design solutions that will make new and existing structures safer and more resilient.

In parallel, computational tools that can predict the behavior of buildings have to be developed and verified against actual collapse events. The progressive collapse assessment of buildings is a challenging field because of the relatively large deformations and material non-linearities associated with severely loaded structural components. Previous analytical and numerical research has given an improved understanding of the response of different structural systems under collapse scenarios and has identified key mechanisms that are developed following localized damage of a few load-bearing members. At the same time, state-of-the-art numerical tools have the capability of simulating and predicting the response of structures in extreme loading events. Nonetheless, these tools need further verification against structures that are physically tested under extreme loading conditions before they can be used in everyday practice.

1.2.2 Research Objective

The first objective of this research study is to identify basic behaviors and ductility limits associated with two different column removal scenarios—an interior column loss and an exterior column loss—through physical testing of steel-concrete composite floor slabs. The second objective is to use the experimental data gathered from the tests to support the validation of numerical simulations using state-of-the-art computer software. These validated models can then be used to develop comprehensive modeling techniques that accurately predict the remaining capacity of a damaged structure. The third objective is to use these techniques to identify influential parameters that have the greatest impact on collapse resistance.

1.3 OUTLINE OF DISSERTATION

The remainder of this dissertation gives a thorough description of the experimental studies performed along with the development and evaluation of detailed computational models. A review of previous research associated with progressive collapse is given in Chapter 2. Chapter 3 provides a description of the design, testing, and response of the experimental tests. Chapter 4 gives a detailed description of the development of FE models that are capable of simulating the response of the test specimens. A comparison between the predicted response of the specimens with the FE models is given in that chapter. Chapter 4 closes with a sensitivity study that was performed to identify influential parameters affecting the response of composite floor systems. Finally, conclusions and recommendations for future research are given in Chapter 5.

CHAPTER 2

PROJECT BACKGROUND

2.1 INTRODUCTION

Researchers have been working to develop systematic approaches for evaluating the progressive collapse potential of existing structures and for designing new structures with improved structural integrity. A common analysis approach is the "alternative load path" (ALP) method. The ALP method is considered threat-independent by evaluating the response of a structure to a specific case of initial local damage, ensuring that the damage will not propagate and lead to progressive collapse. Thus, the majority of research efforts in progressive collapse focus on characterizing the response of a structure or structural components under the removal of load-bearing members. The local damage is usually implemented with the removal of one column (or possibly a few columns), where the cause of this column failure is not considered directly (hence the designation as a threat-independent method). Both the General Services Administration (GSA 2013) and the Department of Defense guidelines for progressive collapse (DoD 2013) include the ALP method of analysis. This approach is comparable with actual incidences of progressive collapse in which the initial loss of a few columns triggered collapse of a larger portion or of the entire structure (FEMA 1996, FEMA 2002).

Research on the progressive collapse of structures can be divided into two broad categories. One category is research on individual structural components, and the other category is investigations on system-level response. The former category focuses on behavior of isolated building substructures, such as planar frames or beam-to-column

connections under conditions aiming to mimic progressive collapse scenarios. These studies provide a good understanding of behaviors and mechanisms associated with progressive collapse. The latter category, which focuses on the response of entire structural systems, proves to be more informative because interactions among the different structural components of an entire structure significantly affect the overall structural response. Extensive numerical studies have been performed, but there are limited experimental studies that can validate the computed results. Physical tests of large-scale structures and in-situ evaluation of the response of actual buildings to progressive collapse scenarios are limited, mainly because of the high costs and practical limitations. The few tests that have been performed demonstrate appreciable levels of resiliency in various structural systems, but they do not provide information on their ultimate capacity before experiencing progressive collapse.

The literature review in this chapter provides an overview of previous progressive collapse research for reinforced concrete (RC) and steel structures, describing the main findings and identifying further research needs. Many of the findings have led to the development of design provisions for progressive collapse, which are presented in the last section of this chapter.

2.2 TERMINOLOGY

The most common nomenclature used for research related to progressive collapse is presented in this section. Many of these terms are used differently in various documents. The most suitable definition for each term is given based on definitions found in the available references addressing the topic.

Abnormal Loads – **"**Loads other than conventional design loads (dead, live, wind, seismic, etc.) for structures such as air blast pressures generated by an explosion or impact by vehicles, etc." (GSA 2003)

Collapse – "Loss of structural integrity of a building or bridge that is caused from an extreme loading event such as blast, impact, earthquake, etc"

Collapse Resistance – "Insensitivity to accidental circumstances, which are low probability events and unforeseeable incidences." (Starossek 2006)

Progressive Collapse – "Progressive collapse is a situation where local failure of a primary structural component leads to the collapse of adjoining members which, in turn, leads to additional collapse. Hence, the total damage is disproportionate to the original cause." (GSA 2003)

Progressive Collapse Scenario – An initial damage scenario of load-bearing members that may trigger progressive collapse.

Structural Redundancy – "The extent of degradation the structure can suffer without losing some specific elements of its functionality." (Kanno and Ben-Haim 2011)

Structural Robustness – "Robustness is the ability of a structure to withstand events like fire, explosions, impact, or the consequences of human error, without being damaged to an extent disproportionate to the original cause." (ECS 2006)

2.3 TESTS ON ENTIRE STRUCTURES

A direct approach to evaluate the collapse response of buildings is by testing existing structures or by large-scale testing of entire structural systems in which load-bearing members are deliberately removed. This approach can be very informative

because it can directly capture the response of an actual structure and provide valuable information about load redistribution and behaviors associated with progressive collapse scenarios. However, these tests are costly and time-consuming, and in-situ tests are usually limited to older buildings prior to their demolition. Also, practicalities associated with the application of gravity-loads to multi-story buildings cannot easily provide quantitative data about the required load that a structure can sustain under a specific damage scenario before damage will propagate and cause progressive collapse. Large-scale tests of entire structural systems performed in a controlled testing environment can provide important information about their limit states, but such tests are extremely limited.

2.3.1 Tests on Actual Buildings

A series of in-situ tests (Sasani*, et al.* 2007, Sasani and Sagiroglu 2010, Sasani*, et al.* 2011, Sasani and Sagiroglu 2008, Sasani 2008) were performed on older RC structures to evaluate their progressive collapse potential. A ground floor column was explosively removed in different locations for several different buildings (Sasani*, et al.* 2007, Sasani and Sagiroglu 2010). Another test examined the removal of two adjacent columns, one of which was a corner column (Sasani and Sagiroglu 2008). Yet another case considered the removal of four adjacent columns and two second-floor perimeter deep beam segments (Sasani*, et al.* 2011). In all cases, the buildings absorbed the initial damage, and the remaining structure remained intact. Vertical deformations in the location of the deliberately damaged areas were relatively small (i.e., less than two inches). Vierendeel action of the structural frame above the locations of the removed

column/columns was a dominating mechanism for load redistribution, a finding that is supported by the analytical study of Liu, *et al.* (2005) for steel frames. The infill walls and the floor slabs in the vicinity of the damaged columns were also identified as key components for the response of the buildings to the instantaneous column removals.

Although the only loads present during the tests were the self-weight of the buildings, predictions of their behavior including live loads were made using numerical tools. The predictions indicated that the buildings were still able to arrest the initial damage. Considering the various assumptions and the complexities associated with computational modeling of structures, it would be valuable to verify these predictions against additional physical testing. Furthermore, none of these studies identified the ultimate load that the structures could carry before the initial damage would propagate and trigger the collapse of a larger portion of the structure, something that occurred in the bombing of the Alfred P. Murrah Building in Oklahoma City in 1995 (FEMA 1996). Identification of the ductility limits in these cases would give a better understanding of behaviors associated with the propagation of initial damage to the remaining building. An estimate of the residual capacity of a structure following the initial damage of a few load-bearing members would also provide valuable information to immediate responders and potentially help save human lives.

A series of in-situ tests were also performed on steel-framed structures (Giriunas and Sezen 2011, Song and Sezen 2013). In both tests, the buildings withstood the removal of four exterior columns with minor visible damage and maximum vertical displacements less than one inch. The effects of the live load on the response of the building were not evaluated because only the self-weight of the structural and non-

structural components was present at the time of testing. Figure 2.1 shows the condition of one of the test buildings before and after the removal of four exterior columns (Song and Sezen 2013). The buildings in this study demonstrated excellent resiliency because they were able to sustain the column removals. Nonetheless, further analysis identifying critical factors contributing to the response have not been performed.

Figure 2.1: Removal of four exterior columns in a steel-frame building (Song and Sezen 2013): (a) before, (b) after

2.3.2 Large-Scale Tests

Xiao, *et al.* (2013) performed a series of first-story sudden column removals in a three-story half-scale RC structure. Figure 2.2(a) shows a plan view of the structure, and the series of the tests performed are depicted with numbers as follows:

Test 1: Removal of columns A1 and B1

Test 2: Removal of columns D2 and D3

Test 3: Removal of column B3

In addition to the self-weight of the concrete members, a 20 kN/m^2 uniformly distributed load was applied to the tributary area of all three stories for the columns

removed. The structure successfully sustained the instantaneous removal of the columns of Test 1 and Test 3. In Test 2, when the two side columns along the long side of the structure were removed, the deformations increased considerably, and the frame was falling in a free fall form. It eventually collapsed on a steel shoring column. The steel shoring column was placed at the ground floor, a few feet below the slab level to prevent collapse of the frame and allow more tests. The lack of lateral restraint from the adjacent corner columns did not allow the beams framing into the removed columns to develop catenary action. Although the structure did not collapse due to the presence of the steel shoring column, it is speculated that collapse would occur if the shoring support was not present. This test demonstrates the importance of lateral restraint that the intact portions of a structure must provide for the development of catenary action, which is important in redistributing loads to adjacent bays. The gravity loads on these tests were sufficient to demonstrate some of the limit states associated with column removal scenarios, something that the in-situ tests failed to demonstrate due to the lack of any superimposed gravity loads on the buildings.

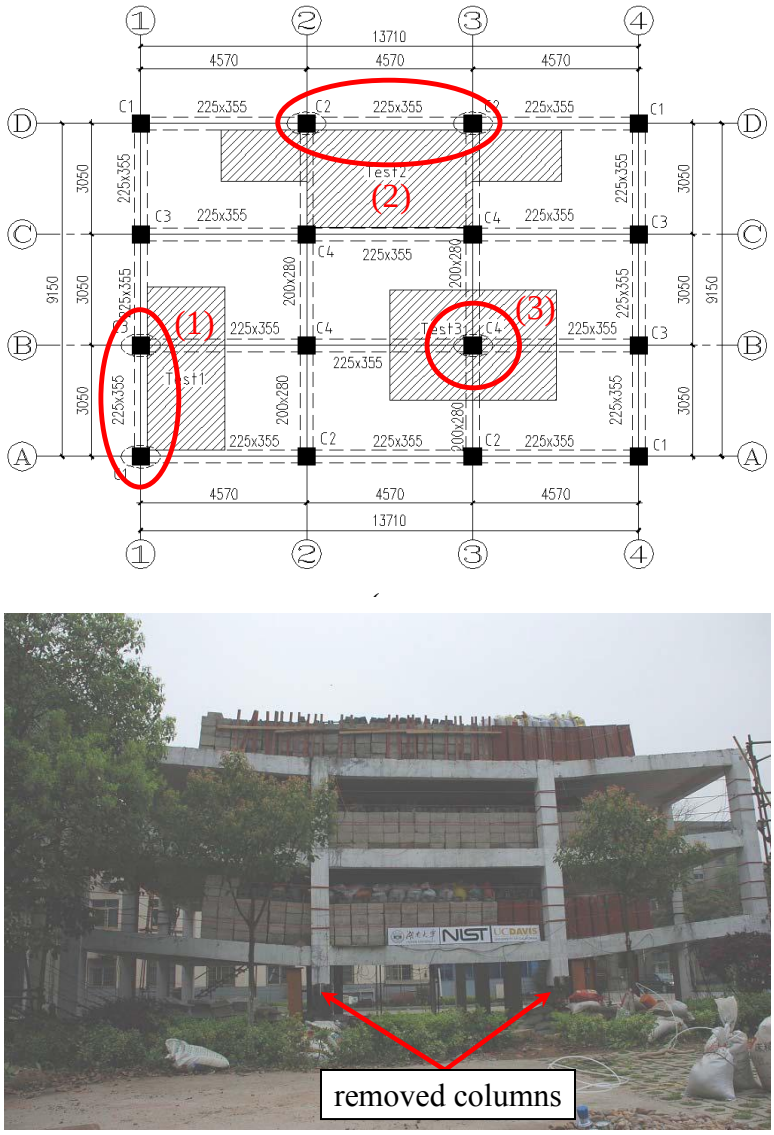

Figure 2.2: RC frame structure under a series of column removal scenarios (Xiao*, et al.* 2013): (a) Plan view, (b) Failure of the structure following the removal of two exterior columns

Chen *et al.* (2011) experimentally investigated the collapse resistance of a full-scale, small-span, two-story steel moment frame after the sudden removal of a perimeter

column. Through computational validation, they also verified the significant role of floor slabs for load redistribution after the removal of the column.

2.3.3 General Observations

The relatively small deflections measured during tests on actual structures, and the absence of any visible damage following the removal of load-bearing members, suggests the previously tested buildings could sustain higher levels of load before experiencing significant damage and collapse. In addition to the structural frame, the experimental data indicate that the in-fill walls and the floor slabs make considerable contributions to the response of the buildings, but experimental investigations quantifying their contributions are limited. Sasani and Kropelnicki (2008) have numerically demonstrated the importance of realistic modeling of floor slabs because they affect the predicted response of a structure and the demands on the beams. Similar findings were obtained from Tsai and Huang (2013) for the contributions of in-fill walls. Limited large-scale tests further support the importance of floor slabs, which, in conjunction with the development of catenary action, can help mitigate progressive collapse after localized failure of load-bearing members.

2.4 BUILDING SUBSTRUCTURES

Due to practicalities associated with testing entire building structures by deliberately removing columns, several research studies have tried to characterize the response of isolated components extracted from prototypical buildings. Building components usually consist of planar beam-column assemblies constructed symmetrically about a middle unsupported column stub, which is loaded until reaching its ultimate

capacity. Figure 2.3 shows a typical beam-column substructure. The behavior of these assemblies under increasing displacements is characterized by three stages:

(a) Flexural action

(b) Compressive arching action

(c) Catenary action

Figure 2.4 shows the load versus displacement curve typically obtained from such tests. The last two stages of this behavior exist only if sufficient lateral restraint is provided at the ends of the substructure. In an actual building configuration, the degree of lateral restraint provided to such components depends on their location. Thus, a direct correlation between the response of these sub-assemblies and the response of the entire structure is not always feasible, which was demonstrated on a previous full-scale test (Xiao*, et al.* 2013). Other studies focus on the characterization of beam-to-column connections under load combinations developed during progressive collapse scenarios.

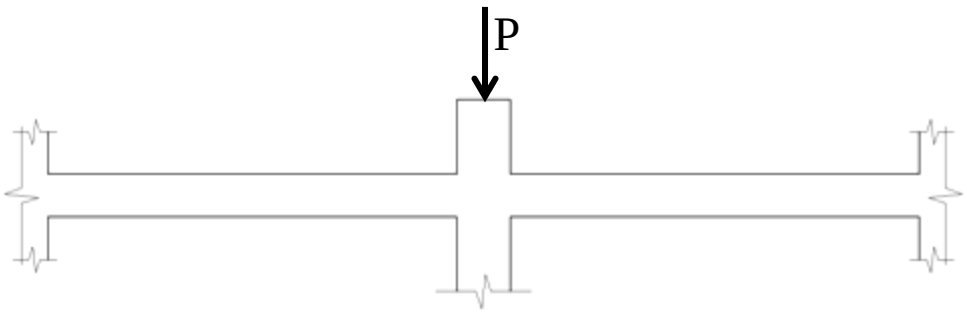

Figure 2.3: Typical beam-column substructure

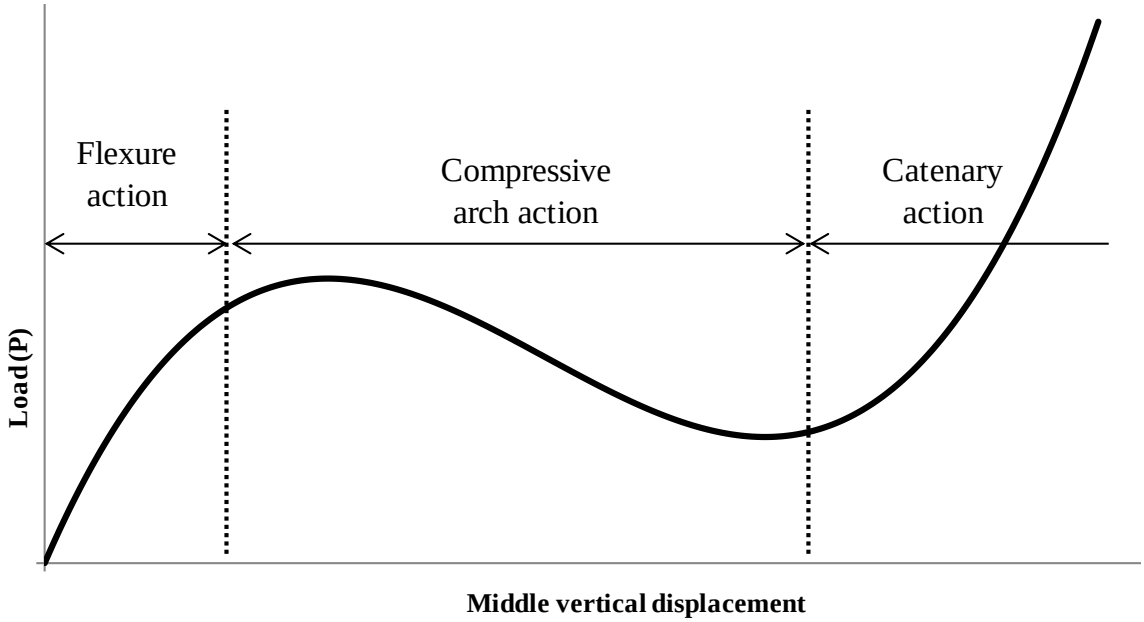

Figure 2.4: Load-displacement curve of beam-column/slab substructure with edges fully restrained

2.4.1 Reinforced Concrete

Yu and Tan (2013) performed tests on RC beam-column sub-assemblies simulating a middle column removal scenario. The half-scale specimens consisted of two beams and three column stubs as shown in Figure 2.5(a). Vertical displacement was enforced at the center column stub using a hydraulic actuator. The prescribed motion was intended to simulate a column loss. As deformations increased, the loads applied from the actuator were redistributed to the end columns mainly through catenary action (i.e., tensile forces in the beams). Catenary action dominated at a vertical deformation approximately equal to the beam depth. Upon reaching the specimen's ultimate capacity, rebar fracture at the joint interfaces was the controlling failure mode. This study highlights the importance of lateral restraint for the development of catenary action. In

the absence of lateral restraint, catenary action cannot be developed, resulting in a significant drop in the ultimate load carrying capacity. The results and failure modes from these tests are in good agreement with similar tests by Yi, *et al.* (2008), Sasani and Kropelnicki (2008), and Sadek, *et al.* (2011). Kai and Li (2012) conducted tests on one-third scale substructures simulating the instantaneous loss of a corner column as shown in Figure 2.5(b). Due to the absence of lateral restraint, the dominant load transfer mechanism in this case was flexural action in the beams. Although the specimens performed well, the authors indicate that the absence of RC slabs in their tests had a significant impact on the capacity of the RC frame.

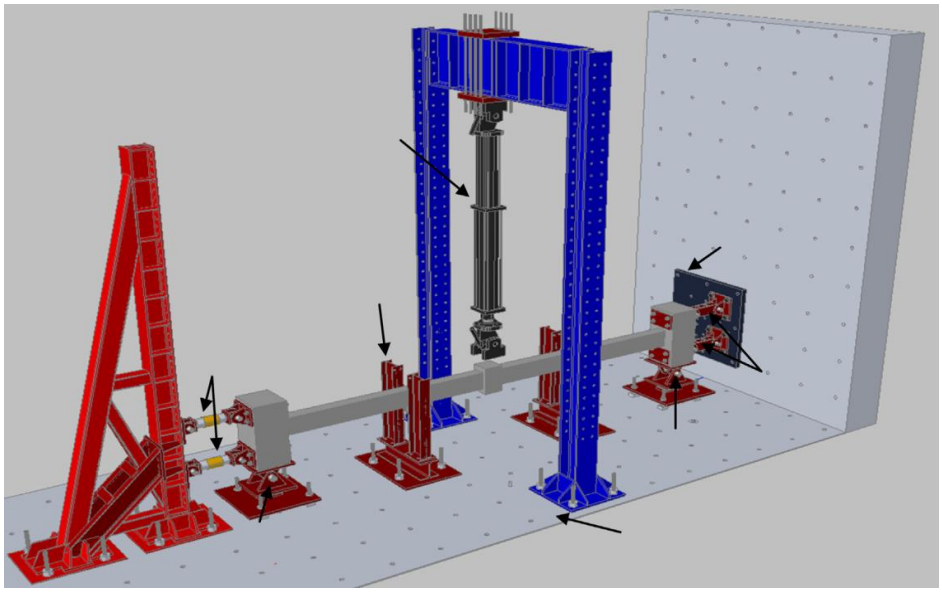

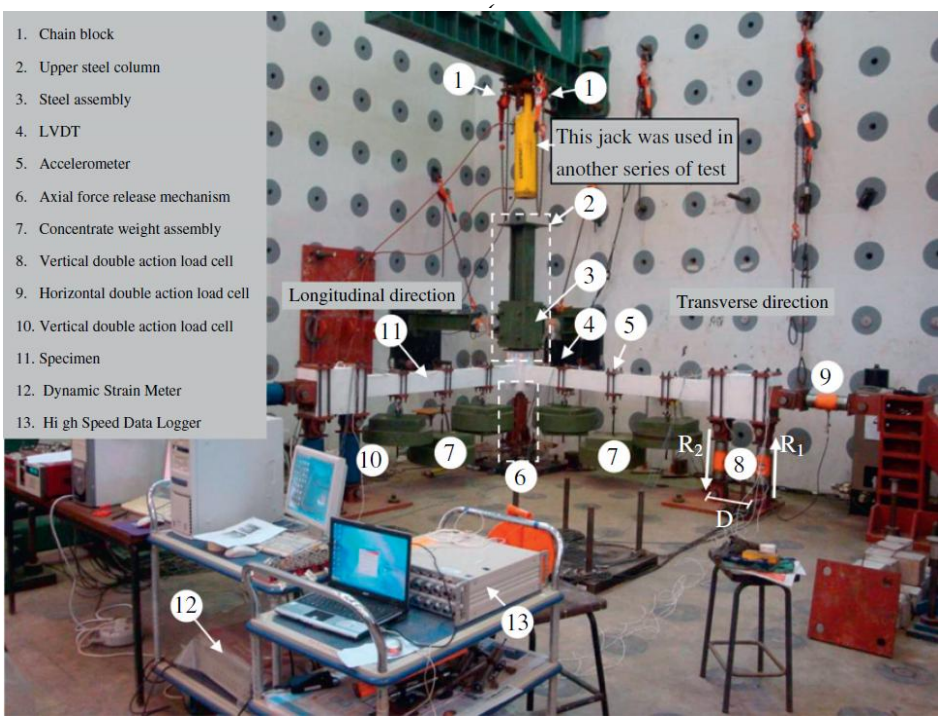

Figure 2.5: Tests in RC substructures: (a) Middle column loss (Yu and Tan 2013), (b) Corner column loss (Kai and Li 2012)

2.4.2 Steel Structures

Tsitos (2009) performed quasi-static tests on two-dimensional, one-third scale, three-story steel moment frames by applying vertical load to the middle column of two-span frames as shown in Figure 2.6(a). The tests aimed to evaluate the effectiveness of earthquake resistant detailing in mitigating progressive collapse. The researchers concluded the frames had adequate capacity to bridge over a damaged column as a part of an actual structure. Nonetheless, if these frames were part of a building, they would have different boundary conditions, which is something that would potentially alter their response. This hypothesis is supported by the observation that the inward movement of the columns prevented the development of catenary action. In an attempt to simulate appropriate boundary conditions in isolated substructures, Sadek *et al.* (2010) performed similar tests on steel beam-column assemblies with moment resisting connections, simulating middle column loss scenarios. The tests were specially designed so that inward displacement was not allowed as shown in Figure 2.6(b). The response at the early stages of vertical displacement was dominated by flexural action. At increasing vertical displacements, the primary load-resisting mechanism was through catenary action, which eventually caused the beams to fracture close to their end connections. Because lateral restraint was provided, significant hardening was observed in this case compared to previous tests (Tsitos 2009). The importance of lateral restraint for the development of catenary action was also identified in similar tests by Guo, *et al.* (2013) on a two-dimensional, steel-concrete composite frame with moment connections. Guo, *et al.* (2013) concluded that the composite moment frames had sufficient capacity to resist progressive collapse.

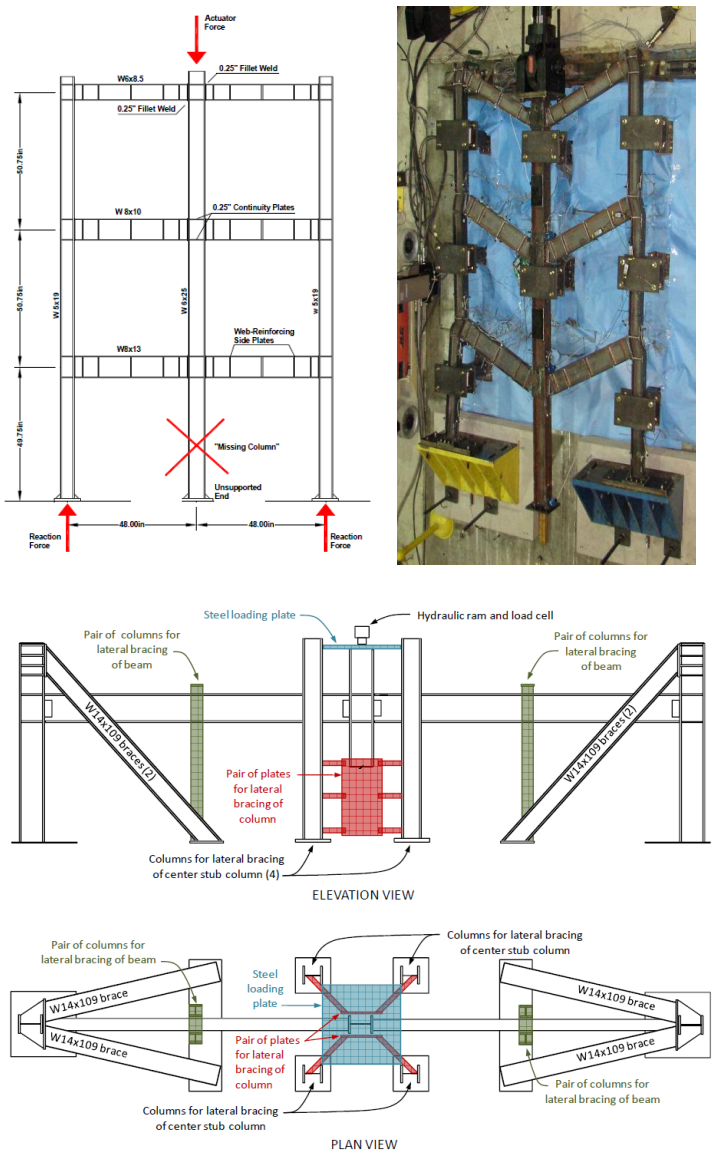

Figure 2.6: Tests in steel substructures with moment connections: (a) 2D frame (Tsitos 2009), (b) beam-column assembly (Sadek, *et al.* 2010)

In contrast with the good performance of steel frames with moment connections, experimental studies of simple shear connections tested under column removal scenarios

demonstrate that their ability to resist progressive collapse is questionable. Weigand and Berman (2013) performed a series of tests on single plate shear connections extracted from a prototypical steel-framed building. The connections were loaded under combinations of tensile and shear force aiming to characterize their response under column removal scenarios. Analyses of the experimental results showed that the connections did not have adequate capacity to carry the specified design shear strength. The authors suggested that the resistance of the composite floor slab, present in an actual building configuration, might be essential to resisting collapse. In a related project, Yang and Tan (2013) performed a series of tests on double-angle shear connections to characterize their response under tensile loads. Similar failure modes were observed in both test programs, as shown in Figure 2.7.

Figure 2.7: Failure modes observed in simple shear connections under tensile loads: (a) Single plate shear connection (Weigand and Berman 2013), (b) Double angle shear connection (Yang and Tan 2013)

The poor behavior of simple shear connections under large deformations can be attributed to their limited ability to develop catenary forces. In simple shear connections, only a part of the web is engaged for the development of tensile forces, whereas in moment-resisting connections the entire section contributes. Comparison of the failure

modes between moment and simple connections further supports this argument. As shown in Figure 2.8 and Figure 2.9, failure in moment-resisting connections under a simulated middle column removal scenario is usually due to fracture of the beam section adjacent to the connection. On the contrary, under similar loading conditions, failure modes in simple connections, shown in Figure 2.7, occur within the connection components and are associated with bolt fracture or fracture of the connection plates or angles.

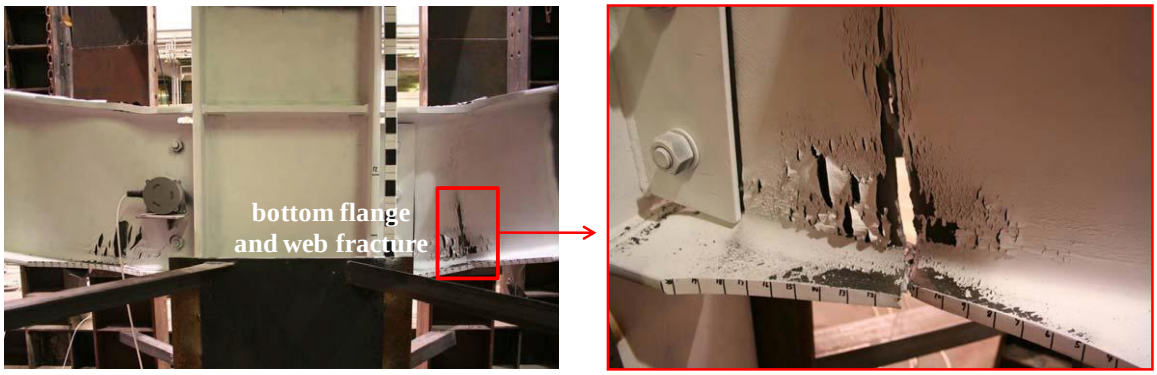

Figure 2.8: Failure modes in bare-steel moment frame under middle column loss scenario (Sadek, *et al.* 2010)

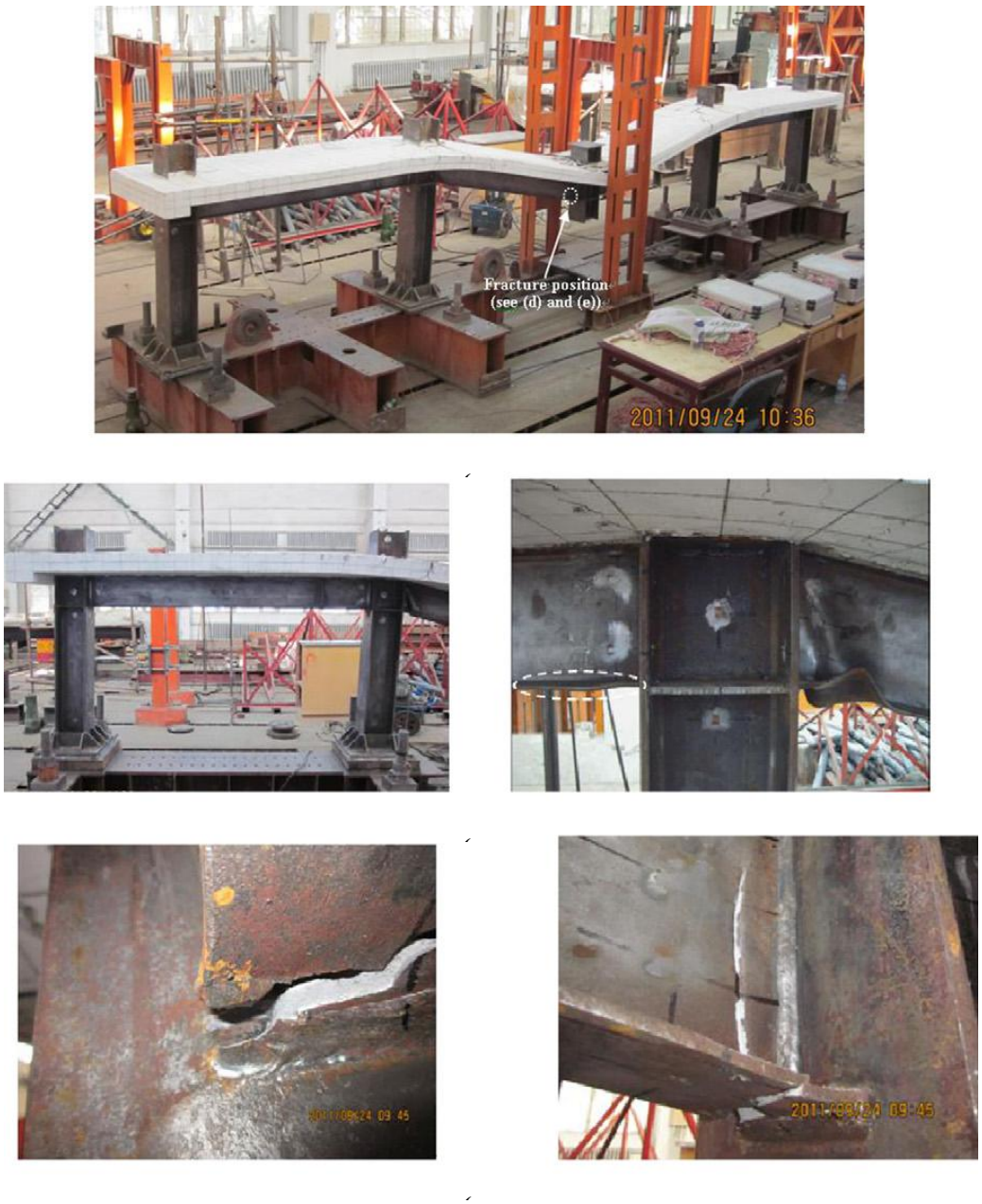

Figure 2.9: Failure modes in composite moment frame under middle column loss scenario (Guo, *et al.* 2013): (a) Overall condition of the specimen after the test, (b) Localized beam buckling, (c) Bottom flange and web fracture

2.4.3 General Observations

Results from the studies described above highlight that structural systems with the ability to develop catenary action demonstrate increased resiliency under progressive collapse scenarios compared to cases in which catenary action cannot develop (e.g., corner column removal scenario). The development of catenary action requires sufficient lateral restraint that prevents inward displacement of the beam ends and allows the beams to develop tensile forces under large deformations. RC and steel frames with moment-resisting connections perform well under a simulated column loss because of their high ductility limits and their ability to resist gravity loads under large deformations through the development of catenary action. In fact, special moment-resisting frames used to resist seismic loads perform well under column removal scenarios because of the continuity and high-ductility requirements they meet. On the contrary, frames with simple shear connections, which are typically used as part of the gravity-load resisting system of steel buildings, perform poorly under column removal scenarios, and experimental tests on simple beam-to-column connections suggest they cannot absorb the loss of a column (Weigand and Berman 2013).

The majority of these past research studies acknowledge that the contributions of floor slabs are significant and can potentially help prevent progressive collapse. Therefore, investigations of floor slab contributions, particularly in frames with simple shear connections, demonstrate that their contributions are sometimes sufficient to prevent progressive collapse as Williamson and Stevens (2009) showed in preliminary numerical studies.

2.5 COMPOSITE FLOOR SLAB CONTRIBUTIONS

Alashker *et al.* (2011) demonstrated through computational analyses the importance of including floor slabs when assessing the potential for progressive collapse. Slabs provide continuity to a structure's frame, and their response after local damage to a load-bearing element may eliminate, or possibly allow, the spread of damage. Uncontrolled spreading of damage can lead to progressive collapse. The importance of floor slab contributions is also acknowledged in the latest version of the DoD guidelines (2013) because floor systems are considered to be primary structural components that are expected to carry the horizontal tie forces supporting the development of alternative load paths after the loss of a column.

The behavior of RC slabs under large deformations and column loss scenarios has been extensively investigated through numerous studies such as (Park 1964a, Park 1964b, Mitchell and Cook 1984, Yi*, et al.* 2014). These studies demonstrate that the tensile capacity of the reinforcement of RC slabs is able to develop tensile membrane action under increasing deformations. The findings from these studies are not directly applicable to composite floor slabs commonly found in steel buildings. Composite floor slabs are usually lightly reinforced because the steel deck, which is usually used as permanent formwork for the concrete topping, acts as external reinforcement. Because of the different arrangements of the steel elements that can be found in actual structures, the degree of tensile membrane action that can develop is questionable. Research regarding the contributions of composite floor slabs is limited and is presented in this section.

2.5.1 Numerical Studies

Research regarding the contribution of floor slabs under progressive collapse scenarios is mostly computational and has not been validated adequately with experimental data. Various research studies have demonstrated the increased capacity of composite floor slabs and the importance of membrane action developed in the steel deck under a column loss scenario. For example, Li and El-Tawil (2012) found that slab-beam composite action plays a significant role in the response of a building after a column loss. Foley *et al.* (2007) showed that a composite floor system is able to sustain a center column loss under dead and service live loads, but they did not fully account for dynamic effects. Conversely, Sadek *et al.* (2008) suggested that their prototype composite floor system was not able to sustain a center column loss. Sadek *et al.* (2008) emphasized the significant contribution of membrane action that is developed through the steel deck of such floor systems, which was later confirmed by the work of Alashker *et al.* (2010). Figure 2.10 shows the results from the numerical studies by Sadek *et al.* (2008) and the enhanced capacity of a composite floor system with shear connections when explicitly modeling the floor slab. Sadek *et al.* (2008) acknowledge the discrepancies between their conclusions and those of Foley *et al.* (2007), and they attribute the differences, among other reasons, to the modeling assumptions employed. These discrepancies in the research literature highlight the need for more experimental data on the response of composite floor systems under column loss scenarios so that modeling techniques can be validated.

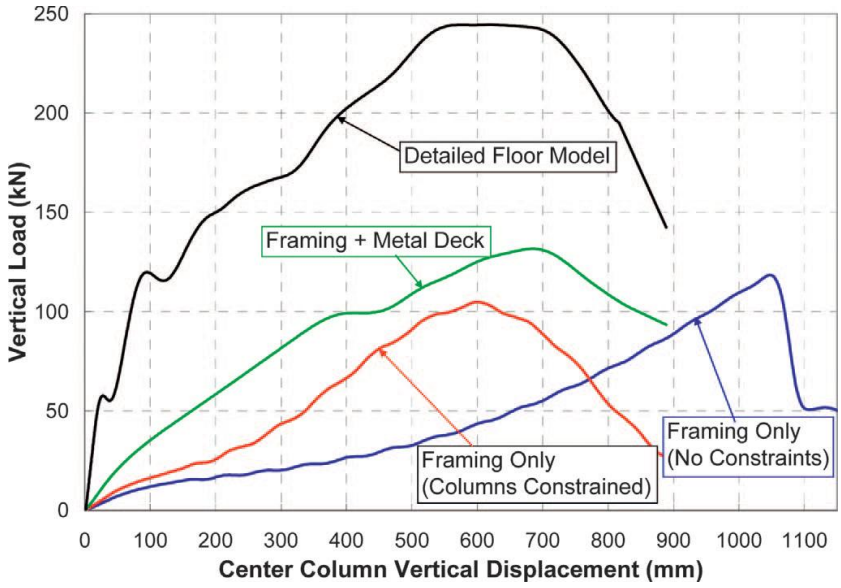

Figure 2.10: Load versus center vertical displacement of a steel-concrete composite floor slab with simple connections (Sadek, *et al.* 2008)

2.5.2 Experimental Studies

Experimental studies on full-scale composite floor systems under a column loss scenario are extremely limited. Tan and Astaneh-Asl (2003) tested a composite floor slab with typical shear tab connections under a middle perimeter column removal scenario by imposing a concentrated load at the location of the removed column. The researchers concluded that a steel-concrete composite floor slab with single-plate shear connections was able to resist progressive collapse after the removal of a façade column and acknowledged the beneficial effect of the concrete slab on the performance of the specimen. Tan and Astaneh-Asl (2003) performed additional tests to evaluate the efficiency of post-installed cables to prevent progressive collapse. Using computational models, Alashker *et al.* (2010) demonstrated that imposing a concentrated load can potentially alter the response of the slab as compared to the application of a uniformly

distributed load. Also, the specimen tested by Astaneh-Asl, *et al.* (2003) had a lightweight concrete topping, but it is also common practice to use normal-weight concrete. One limitation of these studies is that only a perimeter column removal scenario was considered, and no experimental data are available for an interior column loss scenario. Also, neither of these studies identified the ductility limits of such floor systems by loading them to total collapse.

Recently, a series of large-scale experimental tests was performed at the University of Illinois at Urbana-Champaign (Johnson 2014) on a one-story 3-bay × 3-bay steel gravity frame with composite floor slabs as shown in Figure 2.11. The steel frame was half-scale with 15-ft long square bays. It was tested under a series of single column removal scenarios, which are summarized in Table 2.1. The tests included a corner column loss, an edge column loss with spandrel beams, an edge column loss with spandrel girders, and an interior column loss. The locations of these columns are depicted in Figure 2.11. It is interesting that none of these four tests sustained the code defined extreme load combination of 135 psf (Table 2.1), which is inconsistent with the previous experimental results reported by Astaneh-Asl, *et al.* (2003) and the computational studies by Foley, *et al.* (2007). Johnson (2014) acknowledged that the interior column loss case had a low capacity because of damage incurred from the previous tests. These discrepancies highlight the need for a better understanding of behaviors associated with the response of such floor systems under column removal scenarios and for valid predictions of their ultimate capacities after the loss of a column. Additional experimental tests dealing with these issues would provide valuable information for the validation of

comprehensive modeling procedures that can accurately predict the response of floor slabs up to their ultimate load-carrying capacity.

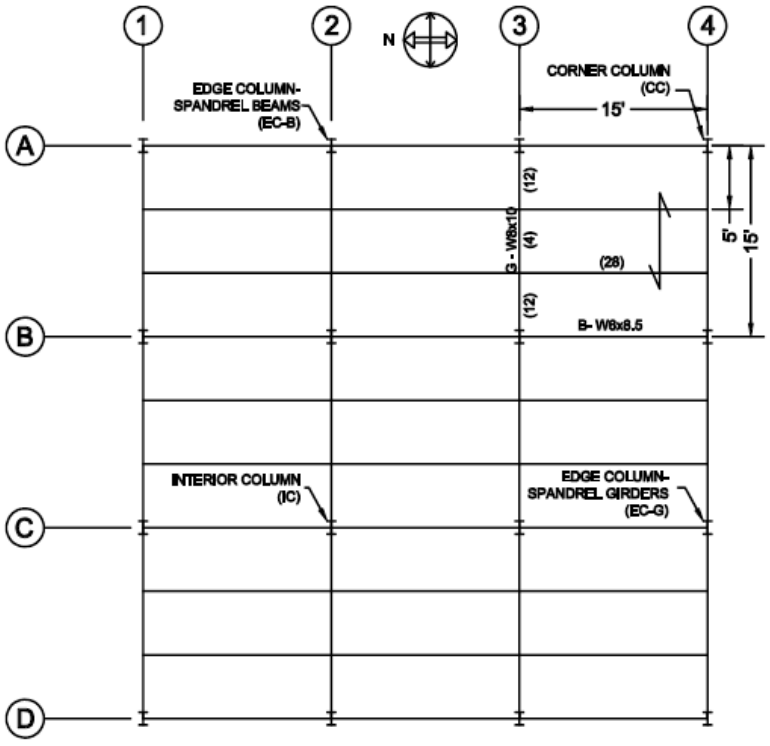

Figure 2.11: Floor system layout with the locations of the column removals (Johnson 2014)

Configuration	Max. Sustained Load	Displacement at Max. Load
Corner Column	60 psf	8.25 in.
Edge Column-Spandrel Beams	83 psf	13 in.
Edge Column-Spandrel Girders	84 psf	6.25 in.
Interior Column*	67 psf	5.5 in.
Extreme Event Load: 1.2D+0.5L	135 psf	N/A

*IC test capacity was greatly reduced due to floor damage from prior tests

Table 2.1: Summary of experimental results (Johnson 2014)

2.6 GUIDELINES FOR PROGRESSIVE COLLAPSE

Guidelines for progressive collapse analysis and design of structures can be found in various documents in the United States (US) and other international codes. The design basis in most of these codes is that the final damage, following the initial local damage from abnormal loads, should not be disproportionate to the initial local failure (Mohamed 2006). Therefore, the initial damage of a few load-bearing members should not trigger damage to a larger portion of the structure. The main provisions in the US for progressive collapse are documents from the General Services Administration (2013) "Alternative Path Analysis and Design Guidelines for Progressive Collapse" and from the Unified Facilities Criteria (UFC) (2013) "UFC 4-023-03: Design of Buildings to Resist Progressive Collapse." These documents have many similarities and provide guidelines for analysis methodologies under specific loads and damage scenarios. The UFC

guidelines (2013) provide three design methodologies to increase the resiliency of new and existing structures:

(a) Tie force method

(b) Alternate load path method (ALP)

(c) Enhanced local resistance

The implementation of these design methodologies depends on the occupancy category of the building being evaluated, as described in the document. All analyses are performed under a uniform floor load of:

$$1.2D + 0.5L$$

where D is the dead load and L is the live load.

The "Tie force" method is used to mechanically tie a building together, ensuring that the loss of a main load-carrying member will be arrested as a result of the continuity provided from the longitudinal and transverse ties and/or peripheral ties. The ties are placed usually in the structure before casting the concrete. The existing steel reinforcement of the structure can be considered as part of the required ties. Figure 2.12 shows a schematic representation of the three kinds of ties that are required. The presence of ties will provide an alternative load path for the redistribution of loads to the intact portion of a building and eventually to the foundation with the help of the vertical ties. Implementation of this method is relatively easy because it does not require detailed analyses. The required strength of ties is a function of the floor loads and the spans of the members. Although this method is considered conservative, some engineers have been critical of its implementation because using this approach often leads to increased costs

and difficulty during construction because of the significant amount of additional reinforcement that must be added to the floor system.

The ALP method is a direct design approach. It requires analysis of the structure under various column removal scenarios, demonstrating that the frame has sufficient capacity to bridge over a damaged column. For each case, one column is removed, but the joints at the column ends remain intact. Although this initial damage scenario might not be what actually happens in a real building, the intent of this design approach is to have a consistent procedure for evaluating whether or not damage propagates and to determine if the overall structural system is capable of sustaining some level of damage. Four analysis methods can be followed: (a) Linear Static, (b) Nonlinear Static, (c) Linear Dynamic, and (d) Nonlinear Dynamic. For the static analyses, guidance is provided for dynamic increase factors (DIF) to account for the inertial effects associated with the instantaneous removal of a column. Acceptance criteria and modeling parameters are adopted from ASCE 41 (ASCE 2007), which provides guidance for designing structures that experience large deformations due to dynamic loadings.

The "Enhanced Local Resistance" method requires designing perimeter columns and walls on the first and second story with enhanced resistance. The enhanced local resistance ensures that these members and their end connections will not fail under the loads anticipated from a specific threat. Because of the uncertainty associated with the design-basis threat, this provision also requires that members will fail in a ductile manner in case they are overloaded. Therefore, columns and walls are designed so that their shear capacity is equal to or greater than the peak shear demand associated with their flexural resistance. This ensures that brittle failure modes are avoided. A comprehensive

description for the development of the UFC guidelines is provided by (Stevens, *et al.* 2011), and an overview of international design guidelines for progressive collapse is provided by (Mohamed 2006, Arup 2011).

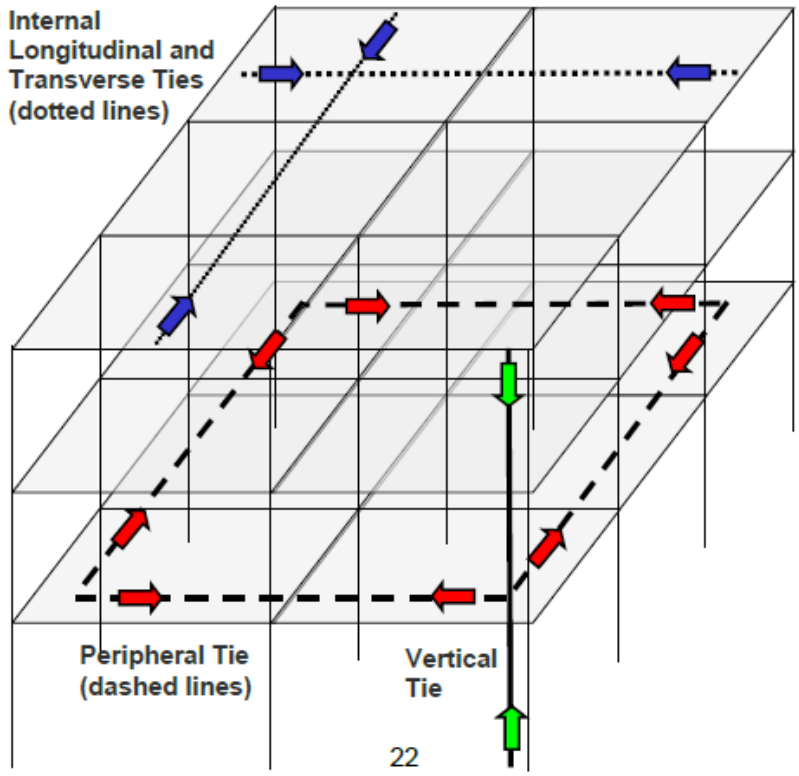

Figure 2.12: Tie forces in a frame structure (DoD 2013)

2.7 CHAPTER SUMMARY

This chapter provided a review of relevant literature on progressive collapse of structures. A summary of common terminology for progressive collapse was given. Research on progressive collapse has focused primarily on the ALP method, which tries to characterize the response of a structure following a specific initial damage scenario. Typically, this scenario involves the removal of one or possibly a few columns, and investigations are made regarding the response of the building following the initial damage. The main objective is to ensure that this initial damage will not propagate and cause damage to a disproportionately large portion of a structure.

Using this approach as a basis, a number of in-situ tests were performed on older RC and steel structures before their demolition. Columns were deliberately removed at various locations on these buildings. The buildings performed well and were able to sustain the initial damage. Nonetheless, the gravity load in the test buildings did not include any live load. The presence of a portion of the live load would be a more realistic scenario and would be more consistent with the recommended floor load for progressive collapse (DoD 2013). Numerical studies have identified that Vierendeel action of the frame, in addition to the contribution of in-fill walls and floor slabs, contributes significantly to the overall response of the buildings after the removal of one or more columns. Large-scale experimental tests on small-scale multi-story structures have also identified the significant contributions of the floor slabs during the redistribution of loads and the importance of lateral restraint for the development of catenary action during progressive collapse scenarios.

A number of studies have also focused on individual component response of building substructures, usually consisting of planar frames of RC and steel structures. Frames with moment-resisting connections, especially those detailed to satisfy seismic design provisions, demonstrate significant ductility and resiliency under large deformations. Simple shear connections commonly found in steel-framed buildings, however, were shown to perform poorly, and experimental studies indicate that a bare steel frame consisting of simple connections cannot successfully sustain the removal of one column. Researchers in most of these studies acknowledge that the absence of the floor slabs that exist in actual buildings might alter and potentially increase the overall capacity of the frame.

Extensive research studies on the response of RC slabs demonstrate their resiliency under column removal scenarios due to their ability to transfer loads to adjacent bays through the development of catenary action. For these components, catenary action develops because of the presence of steel reinforcement. The contributions of composite floor slabs that are usually used in steel-framed structures with simple connections, however, have not been extensively investigated. Results from numerical studies indicate that such floor systems have appreciable amounts of inherit capacity, but these results have not been validated against experimental data. One large-scale test performed on an isolated composite floor slab with simple shear connections further supports the idea that these floor systems have significant resiliency, but the test did not provide any information about the ultimate capacity of the floor slab under a column loss. Further, the test did not show the dominant failure modes that occur prior to collapse. Identifying ultimate capacities and collapse mechanisms before the onset of

failure is essential because it gives a better understanding of how the initial damage might potentially propagate to a larger portion of a structure.

The research study presented in this dissertation provides valuable experimental data regarding the response and ultimate capacity of composite floor slabs under a single column loss scenario. The following chapter provides a description of large-scale experimental tests that were performed at The University of Texas at Austin, aiming to characterize the response of typical composite floor systems under two different column loss scenarios; namely an interior column loss and an exterior column loss scenario. These tests provide information about the response of typical floor systems used in steel-framed buildings during the removal of a single column. Following the removal of that column, the specimens were loaded until total collapse occurred.

CHAPTER 3[1]

EXPERIMENAL PROGRAM

3.1 INTRODUCTION

The experimental program included testing of two different specimens, each with its own unique column removal case. Due to practical limitations and budget constraints associated with testing an entire building with multiple bays under different column loss scenarios, two sections from a typical steel-framed building were isolated and tested independently. The design of the specimens was based on the prototype building depicted in Figure 3.1. Both specimens were constructed and tested at the Ferguson Structural Engineering Laboratory (FSEL) of the University of Texas at Austin. The first specimen, referred to as the ICL specimen, was an interior 2-bay×2-bay section that was tested under an interior column loss scenario. The second specimen, referred to as the ECL specimen, was an exterior 2-bay×1-bay section tested under an exterior column loss scenario. Both specimens utilized simple shear connections to represent isolated portions of the gravity frame of the prototype building. The specimens were tested under a center column removal scenario. The column was statically removed while the slab was uniformly loaded under service load conditions. Because each specimen survived the column removal stage of response, the floor slab was subsequently loaded with uniformly

[1] Hamed Zolghadr Jahromi, Bassam A. Izzuddin, David A. Nethercot, Sean Donahue, Michalis Hadjioannou, Eric B. Williamson, Michael Engelhardt, David Stevens, Kirk Marchand, and Mark Waggoner (2012). "Robustness Assessment of Building Structures under Explosion." *Buildings*, 2(4), 497-518. The author of this dissertation mainly contributed to the sections related to the experimental program described in the article. Co-authors have equally contributed in all the other sections of this article.

distributed load until total collapse was achieved. The tests demonstrated the significant capacity of such floor systems following a column loss. The two specimens were constructed using a specially designed perimeter beam (Figure 3.2), intended to represent the restraints provided from surrounding bays in an actual building.

This chapter provides details for the design of the testing frame and the two specimens. In addition, the response of the two specimens is described in detail.

3.2 PROTOTYPE BUILDING

The design of the specimens was based on a prototype building representative of typical low- to mid-rise steel office buildings (Figure 3.1). The building was designed by Walter P. Moore (WPM), a structural engineering design firm with clients throughout the US and worldwide. The prototype building was a typical 7-story steel-framed structure with steel-concrete composite floors. The structure did not include enhancements for seismic resistance or progressive collapse mitigation. The design loads were based on ASCE 7-10 (2010) for a 90-mph wind speed and for seismic design category A. The design of the steel frame and the composite beams was based on AISC 360-05 (2005), and these members conformed with the serviceability criteria of AISC Design Guide 3 (1990) and the floor vibration criteria of AISC Design Guide 11 (1997). This building incorporated typical connections, steel deck, serviceability considerations for deflections and vibrations, and fire protection.

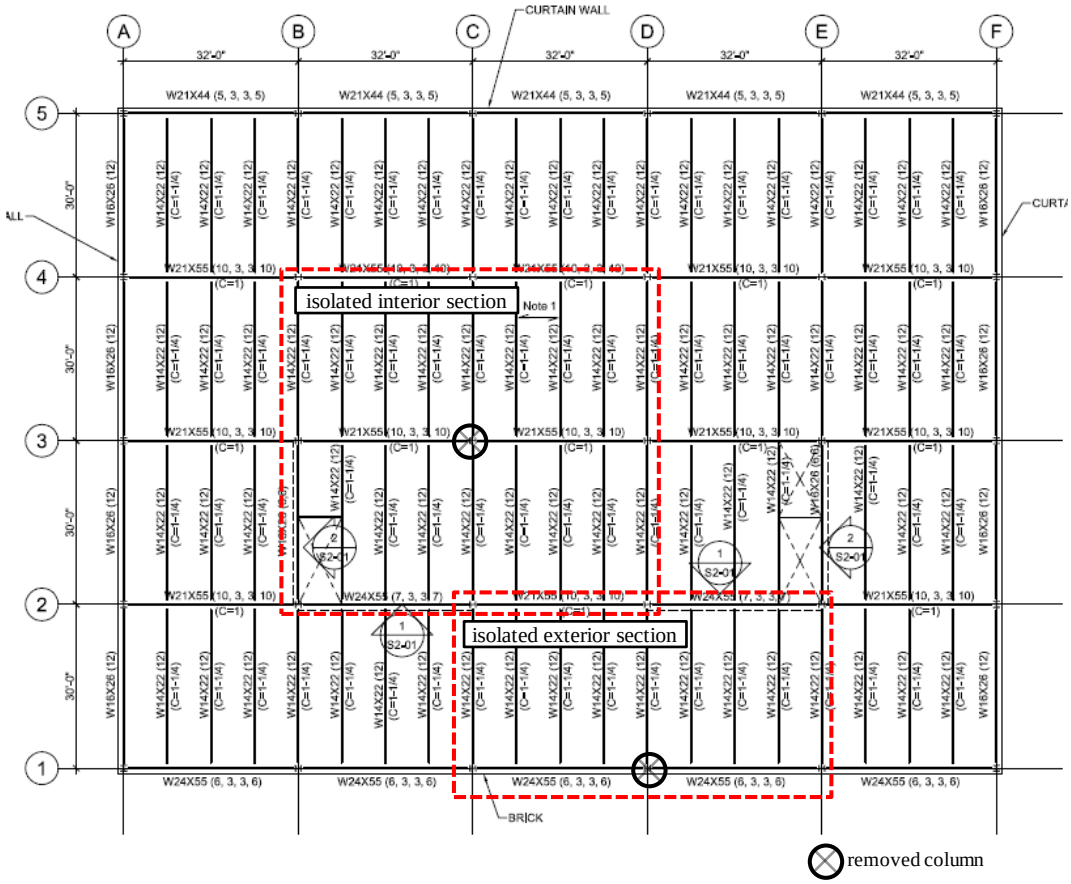

Figure 3.1: Typical floor plan of the prototype building representing locations for the isolated sections of the test specimens

3.3 ISOLATION OF FLOOR SECTIONS

Under a single column loss scenario in an actual building, it is anticipated that the bays of the floor slab adjacent to the lost column will experience large deformations. Hoffman and Fahenstock (2011) demonstrated that the number of stories does not appreciably affect the response of a building following a column loss. Rather, each floor acts independently to redistribute loads from damaged regions to undamaged regions. The remaining structure at each floor level will provide restraint at the perimeter edges of

the affected bays. For the ICL specimen, there are four edges associated with the four bays surrounding the collapsed column, while the ECL specimen has three edges surrounding the two damaged bays. Due to the lack of experimental data on the restraint provided from the remaining structure, a systematic approach was followed to implement reasonable boundary conditions around the perimeter of the two specimens. Both specimens were constructed in the test frame shown in Figure 3.2. A major component of the test frame was a relatively stiff perimeter beam. Details of the geometry and dimensional characteristics of this perimeter beam are shown in Figure 3.3. This stiff perimeter beam was used to provide restraints similar to those imposed from the nearby bays in an actual structure. These restraints can be decomposed into three components: (a) Vertical, (b) Rotational, and (c) Horizontal.

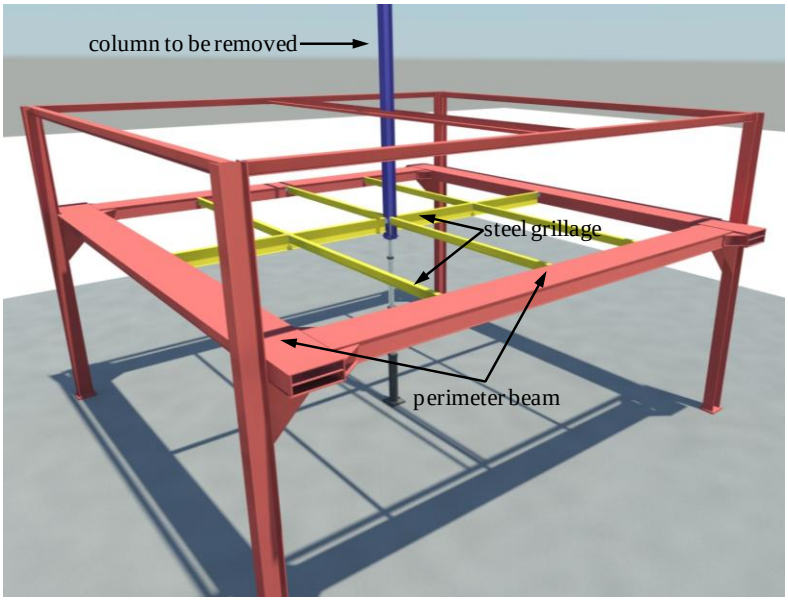

Figure 3.2: Test frame including the perimeter beam and the steel grillage (concrete slab is omitted for clarity)

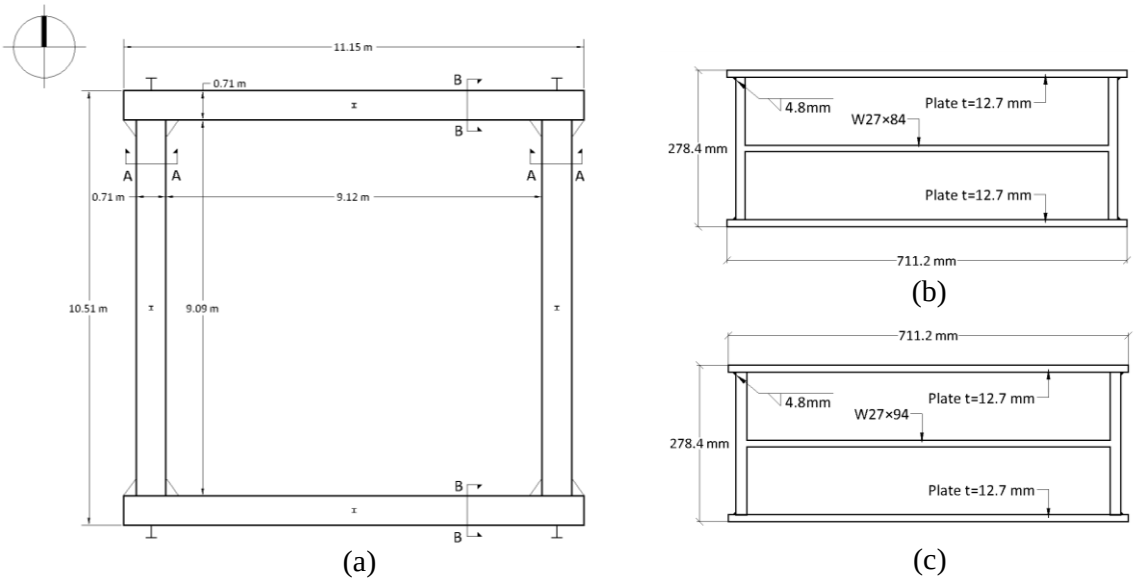

Figure 3.3: Perimeter beam: (a) Plan view, (b) Section A-A, (c) Section B-B

3.3.1 Vertical Restraint

Assuming the floor slab has enough capacity to redistribute the loads carried from the collapsed column, these loads will be shifted to the beams surrounding the affected bays. DoD guidelines (DoD 2013) indicate that the removal of a column is performed under service loads: 1.2 × Dead + 0.5 × Live = 5.10 kN/m^2 (107 psf). Based on the geometry of the floor bays, when the central column is no longer present, the gravity loads in the perimeter beams will increase by 50%, corresponding to a load of 5.10 kN/m^2 × 1.5 = 7.65 kN/m^2 (160 psf). This calculation does not address any dynamic amplification of the load that is expected to occur in an actual column loss scenario. Issues associated with dynamic load amplification are addressed in Section 3.6. The computed load is lower than the ultimate design load (UDL), which is equal to 1.2 × Dead + 1.6 × Live = 7.74 kN/m^2 (162 psf) and described in more detail in the next

section. The demand/capacity ratio during the design of structural components is typically less than 1.0, often 0.8-0.9. Accounting for material overstrength factors (ASCE 2010), it is anticipated that the beams surrounding the affected region (shown in Figure 3.1) have sufficient capacity to carry these extra loads. Under these loads, the maximum vertical deflection of the beams in the prototype building is 5 mm. Under similar loading conditions, the perimeter beam in the reaction structure used in the current experimental program has the capacity to sustain these loads under a vertical deflection of 0.5 mm. In both the prototype building and experimental test setup, deflections are small compared to the span of the bays, and the small difference in magnitude between the two cases is not expected to have a significant influence on the behavior of the test specimens following a column loss. Further, due to uncertainties associated with loads in an actual event, actual material properties, specific location of the failed column, dynamic response characteristics, and other factors, this difference in response between the prototype building and experimental setup is considered to be acceptable.

3.3.2 Rotational Restraint

At the perimeter of the affected region, the top fibers of the slab will start developing tensile stresses after the removal of the column. Because the concrete in such floor systems has minimal reinforcement, mainly for temperature and shrinkage resistance, these tensile stresses will cause early cracking of the concrete along the perimeter of the affected region. The cracking moment per unit width of the concrete slab is approximately 12 kNm/m (8.85 kip-ft/ft), which corresponds to a uniform load of 1.9 kN/m^2 (40 psf), a load that is considerably lower than the UDL. For loads lower than

1.9kN/m^2 (40 psf), moments along the perimeter of the affected region will develop as shown in Figure 3.4(a). Beyond this load, cracks form, causing the moments to remain approximately stable due to the presence of minimum steel reinforcement in the concrete slab. The presence of the reinforcement in the slab is to control cracking and does not typically increase the flexure capacity of the concrete slab. As a result, the affected bays rotate about these cracks in isolation from the adjacent bays with a constant moment equal to the cracking moment of the slab, i.e. 1.9kN/m^2 (40 psf). This moment vanishes at higher rotations as the slab reinforcement fractures, shown in Figure 3.4(b). Thus, rotational restraint is not expected to affect the response of the specimens because the early cracking at the perimeter isolates the affected bays from the remaining structure in terms of rotation.

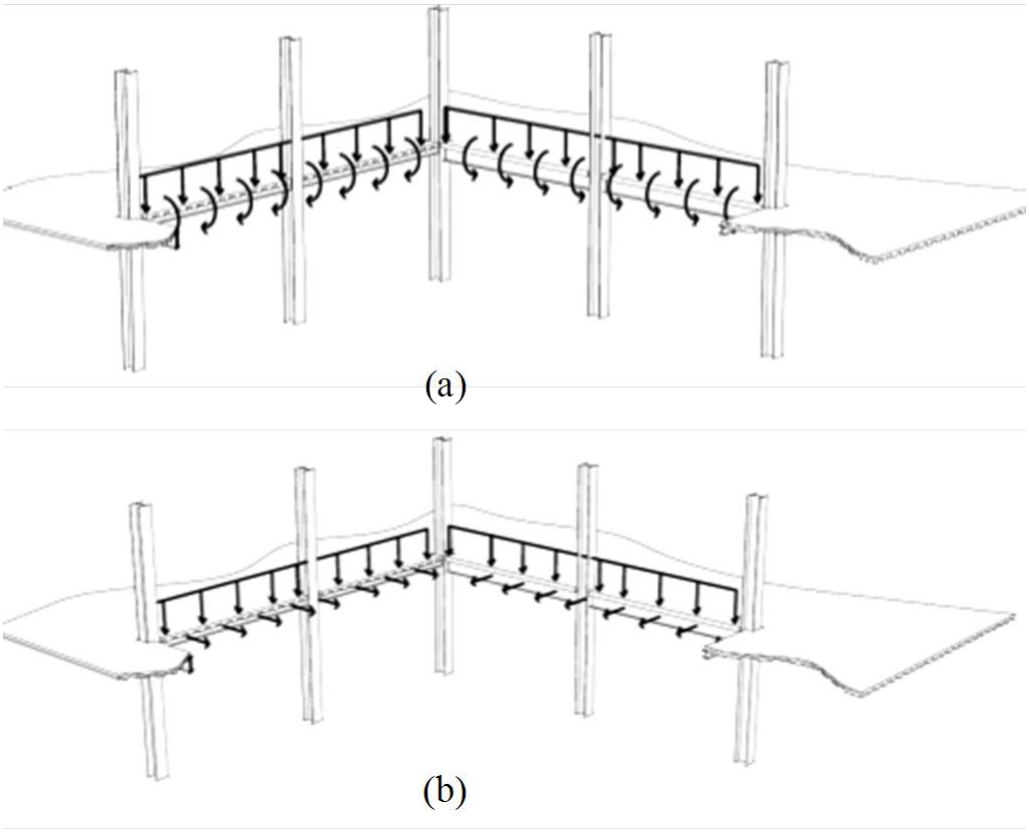

Figure 3.4: Loads exerted at the bays surrounding the ICL specimen (a) before cracking at the perimeter, (b) under larger deformations that reinforcement fractures (ICL specimen is omitted for clarity)

3.3.3 Horizontal Restraint

Under large deformations, the cracking along the perimeter of the affected bays spreads, and the flexural moments acting around the surrounding bays vanish as previously described. At this point, the only continuity between the affected section and the adjacent bays is mainly the corrugated steel deck. The deck under large deformations is expected to develop tensile membrane forces (Alashker and El-Tawil 2011), and the supporting steel beams develop catenary forces (Daneshvar and Driver 2011). The

decking will pull the nearby bays inwards at the locations where it is anchored to the top flange of the surrounding beams through the shear studs, as shown in Figure 3.4(b). The amount of lateral restraint provided by the surrounding bays varies depending on the location of the collapsed column. The lateral stiffness provided by the bays to the left of the ICL case (Figure 3.1) is lower than those to the right of that region. To obtain a good estimate of the in-plane displacement under the expected loads the decking and the beams impose on the adjacent bays, finite element analyses were conducted. Varying the location of the collapsed column for both the interior and exterior column cases, the in-plane displacement was found to vary between 0.5mm and 5mm. These values are based on a simplified model and did not account for local deformations that may occur at the locations where the decking is attached to the shear studs (Figure 3.5) and potential cracking of the concrete in the adjacent bays. The perimeter beam in the experimental test setup was loaded in a similar manner, and the deformations were found to be approximately two to three times larger than the results obtained from the prototypical steel-framed structure. However, the lower stiffness of the perimeter beam in the test structure compensates for the nonlinearities that are expected to occur in an actual building including cracking of concrete and localized deformations of the deck around the shear studs depicted in Figure 3.5. Furthermore, previous research studies suggest that slabs show some degree of self-equilibrating membrane effect, which will reduce the importance of the in-plane restraint provided by the surrounding elements (Bailey 2001).

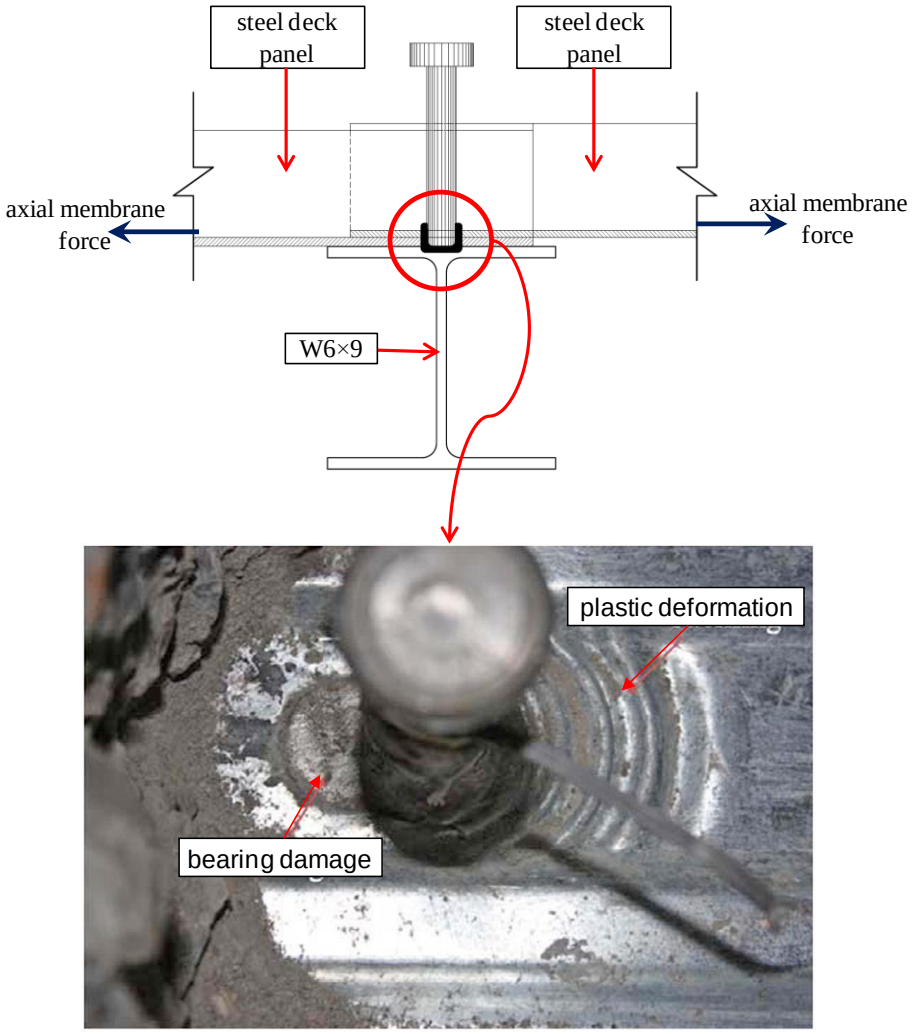

Figure 3.5: Localized deformation for the end anchorage of steel deck (Chen and Shi 2011)

3.3.4 Remarks

Because the location of the damaged column in an actual building and other design details vary, it is impossible to represent all cases with the use of the perimeter restraining beam in the test setup. Accordingly, the boundary conditions provided by the

test configuration may not be suitable for all potential cases. Nonetheless, the use of the perimeter beam allows a controlled experimental setup that can be used to identify and study the primary mechanisms contributing to collapse. Such controlled experimental data allows for the development of validated analysis models, which can then be used to study a wide array of building configurations if desired. Overall, the perimeter restraining beam reasonably represents the types of boundary conditions a typical building is expected to provide, while still providing a repeatable experimental setup that lends itself to controlled testing.

3.4 TEST SPECIMENS

The ICL specimen and the ECL specimen were designed and detailed without any provisions for progressive collapse. They were representative sections of a typical steel-framed building with simple connections. The ICL specimen was constructed and tested in the test frame shown in Figure 3.2. Upon completion of this test, the debris of the collapsed specimen was removed, and then the ECL specimen was constructed and tested.

3.4.1 Test Set-Up

Figure 3.6 represents the experimental set-up used to test the specimens. The supporting frame and the perimeter beam (Figure 3.3) are shown in red. The perimeter beam was placed 4 m above the ground level to ensure there would be sufficient clearance for the slab to deform before collapse. The supporting grillage, which includes the main girder and the floor beams, is shown in yellow. The steel deck and the concrete slab are shown in grey. The mid-span column to be removed is shown in blue.

The column to be removed terminated a few inches below the beams framing into that column and was supported by a collapsible actuator. During construction, the actuator was extended to support the floor slab. It was released during testing to simulate the removal of that column. It is noted that the actuator was configured to bear against a base plate attached to the bottom of the column being removed. It was able to fully disengage from the column without applying any axial load. Figure 3.7 shows a detailed view of the actuator supporting the center column.

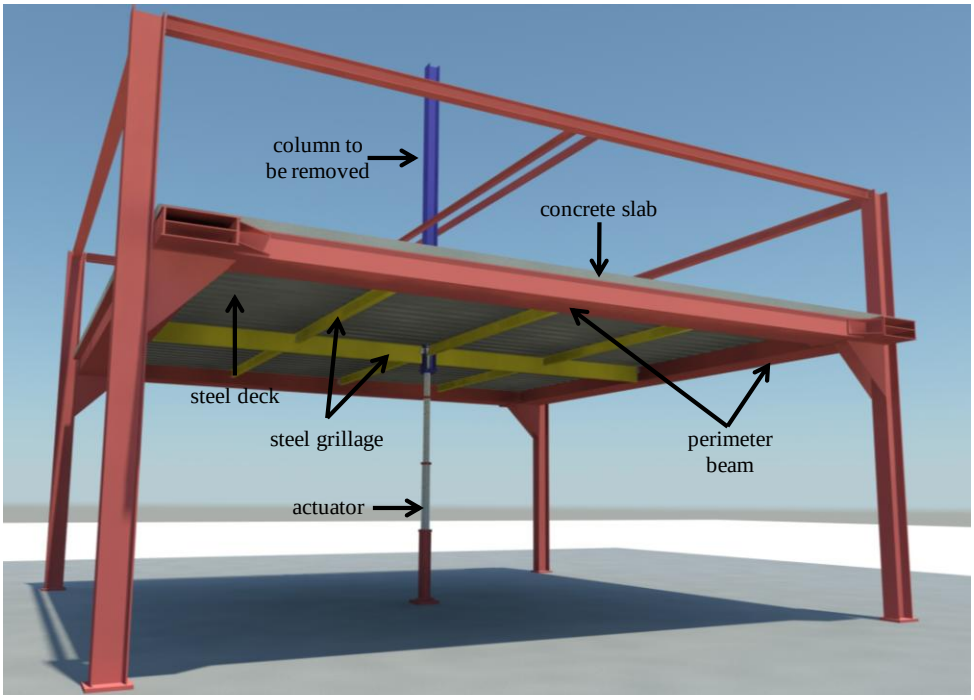

Figure 3.6: Test set-up

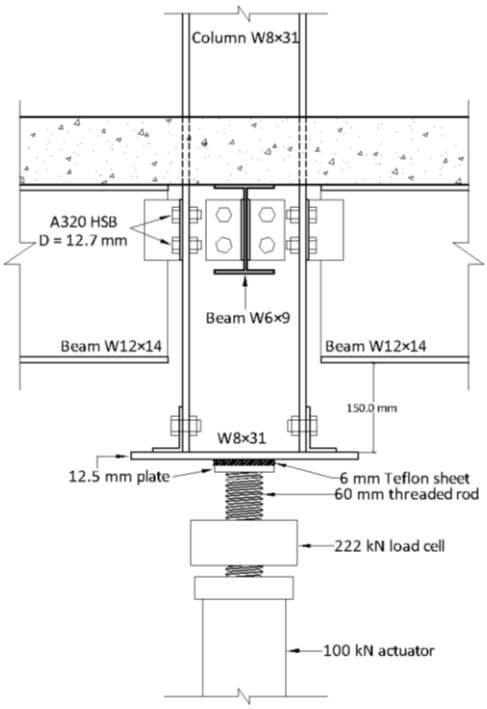

Figure 3.7: Detail of the actuator supporting the removed column

3.4.2 Design of the Specimens

Both test specimens were designed by researchers at The University of Texas at Austin in close cooperation with engineers from WPM. The intent was to design and detail the specimens to meet common practices followed in the US. The design loads for the specimens were based on ASCE 7-10 (2010) for a typical office building. The dead load due to the self-weight of the slab and steel members was 2.30 kN/m2 (48 psf), and an additional dead load of 1 kN/m2 (20 psf) was assumed to account for permanent floor loads. The design live load was 2.4 kN/m^2 (50 psf), leading to a UDL (1.2 × Dead + 1.6 × Live) of 7.74 kN/m^2 (162 psf). The perimeter beams for the ECL specimen were designed to sustain an additional façade load of 5 kN/m (345 plf). Figure 3.8 shows a plan view of

both specimens and the member sizes that were used. The plan dimensions for each bay were 4.55 m × 4.55 m, with one intermediate beam that divides the bays into panels of 2.28 m × 4.55 m. A 51-mm depth, composite, ribbed, 0.75-mm thick Vulcraft Structural Steel Decking Type 2VLI22 was chosen; it was continuous within each bay, bridging over the two 2.28-m spans. A slab depth of 114 mm with normal-weight concrete (24 kN/m^3) topping is specified in the Vulcraft catalogue (2008) to support the design loads. Figure 3.9 illustrates the cross-section of a decking sheet panel with the concrete topping and the minimum steel reinforcement consisting of 3-mm diameter WWM spaced at 150-mm in both directions. The supporting steel grillage acted compositely with the concrete slab through 12.7-mm diameter, 89-mm long shear studs. Shear studs were also welded along the perimeter beam under the assumption that in an actual building the beams adjacent to the affected bays also have shear studs (Figure 3.8). To meet the requirements of AISC 360-05 (2005), the main girders consisted of W12×14 steel sections, and the transverse beams were W6×9 sections. The two most commonly used connection types in such floor systems were employed. The intermediate transverse beams within each bay were connected with shear tab connections (Figure 3.10(a)), and all remaining members were connected with double-angle shear connections (Figure 3.10(b)). The angles and the plates were welded to the beams and girders using 4.8-mm fillet welds with E70 electrodes, and 12.7-mm diameter bolts were used for all the bolted connections.

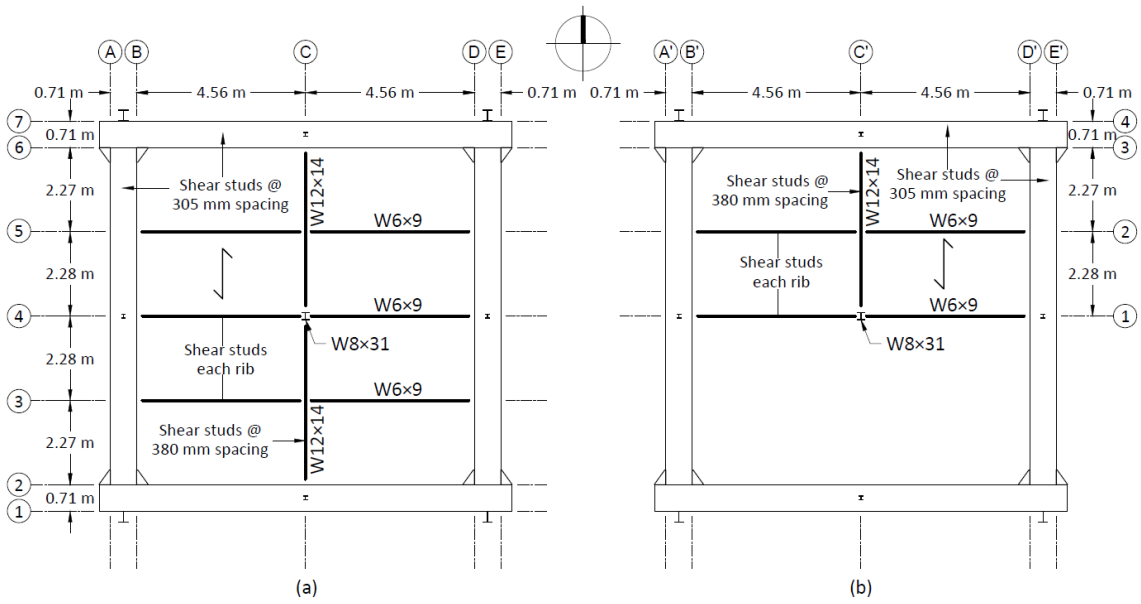

Figure 3.8: Plan view of the test specimens: (a) ICL specimen, (b) ECL specimen

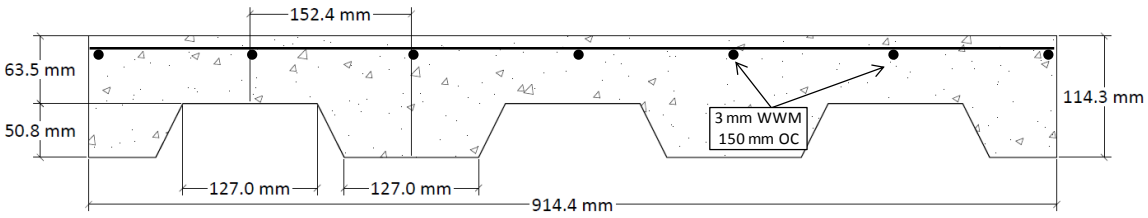

Figure 3.9: Steel-concrete composite deck geometry

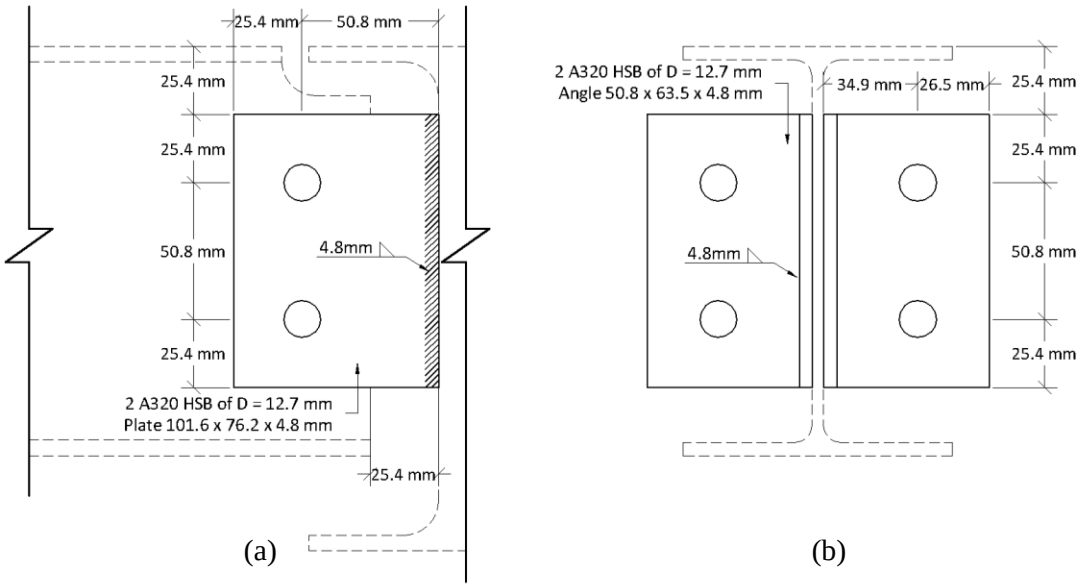

Figure 3.10: Connections used in the test specimens: (a) Single-plate shear connection, (b) Double-angle shear connection

3.4.3 Material Properties

All floor beams and girders were constructed using ASTM A992 steel. The shear tab and double-angle connections were made from A36 steel, while the steel deck utilized A653-91 material. All bolts were A325. There tensile tests were carried out for each components to evaluate the material properties of the steel components used in the tests, and Table 3.1 provides an average of the measured values. The concrete used for the floor slab was a small-aggregate mix with a specified compressive strength of 24 MPa. Eight cylinder tests using 100-mm diameter by 200-mm long specimens were carried out on the day of testing, and the average unconfined compressive strength values are summarized in Table 3.2.

Specimen	Upper yield point (MPa)	Static yield stress (MPa)	Dynamic yield stress (MPa)[a]	Dynamic tensile strength (MPa)[a]	Tensile strength-to-yield stress ratio	Strain at onset of strain hardening (%)	Strain at onset of necking (%)	Elongation (%)
W12×14 - Web	421	392	404	500	1.24	4.0%	19.6	33.8
W12×14 - Flange	396	368	383	483	1.26	2.6%	19.3	33.5
W6×9 - Web	394	369	389	489	1.26	3.4%	19.2	32.7
W6×9 - Flange	384	363	370	481.5	1.30	2.6%	17.7	32.3
Angle 50.8 × 63.5 × 4.8 mm	N.A.	N.A.	400	539	1.35	N.A.	15.8	30.4
Shear tab plate at ring beam	302	292	303.6	378	1.25	1.5%	20.2	40.0
Shear tab plate at girder	360	355	358	575	1.61	0.9%	14.8	30.0
2VLI11 Corrugated deck	338	317	332	396	1.19	3.0%	17.7	27.7

[a] Strain rate of 0.51 mm/min

Table 3.1: Summary of Material Properties Measured from Coupon Tests

Specimen	Age of concrete (days)[a]	Average compressive strength (MPa)
ICL	29	40
ECL	57	46

[a] Corresponds to the age at the day of the test

Table 3.2: Summary of Concrete Strengths Obtained from Cylinder Tests

3.4.4 Design/Construction Details

The corrugated decking was provided in sheets having a width of 914 mm (Figure 3.9). Six sheets of 5.20-m length were used to cover each bay. Self-tapping #10 screws, commonly known as tek screws, were used to fasten the decking to the steel grillage. The sheets were placed with an overlap of 60 mm on both sides, and #10 tek screws were

placed every 750 mm, creating side laps parallel to the north-south direction and a longitudinal lap parallel to the east-west direction. Additionally, one tek screw was placed adjacent to the location where each shear stud (Figure 3.8) was welded at a later stage. The concrete topping was lightly reinforced with Welded Wire Mesh (WWM) to provide temperature and shrinkage resistance. The mesh had grid dimensions of 150 mm × 150 mm × 3.125 mm. The WWM was provided in rolls 1.50-m wide, and the lap length was 150 mm between adjacent strips. Steel chairs were used to maintain a clear cover of 25 mm. On the recommendation of structural engineers from WPM, additional reinforcing bars of 1.20-m length were placed in the north-south direction on top of the W12×14 girder and along the east and west edges at a spacing of 300 mm as shown in Figure 3.11. In the ICL specimen, 9.5-mm bars were used, and 11.7-mm bars were used in the ECL specimen. These bars were tied on top of the WWM having a clear cover of 15.6 mm. This additional reinforcement is used to control cracking in the slab under service loads.

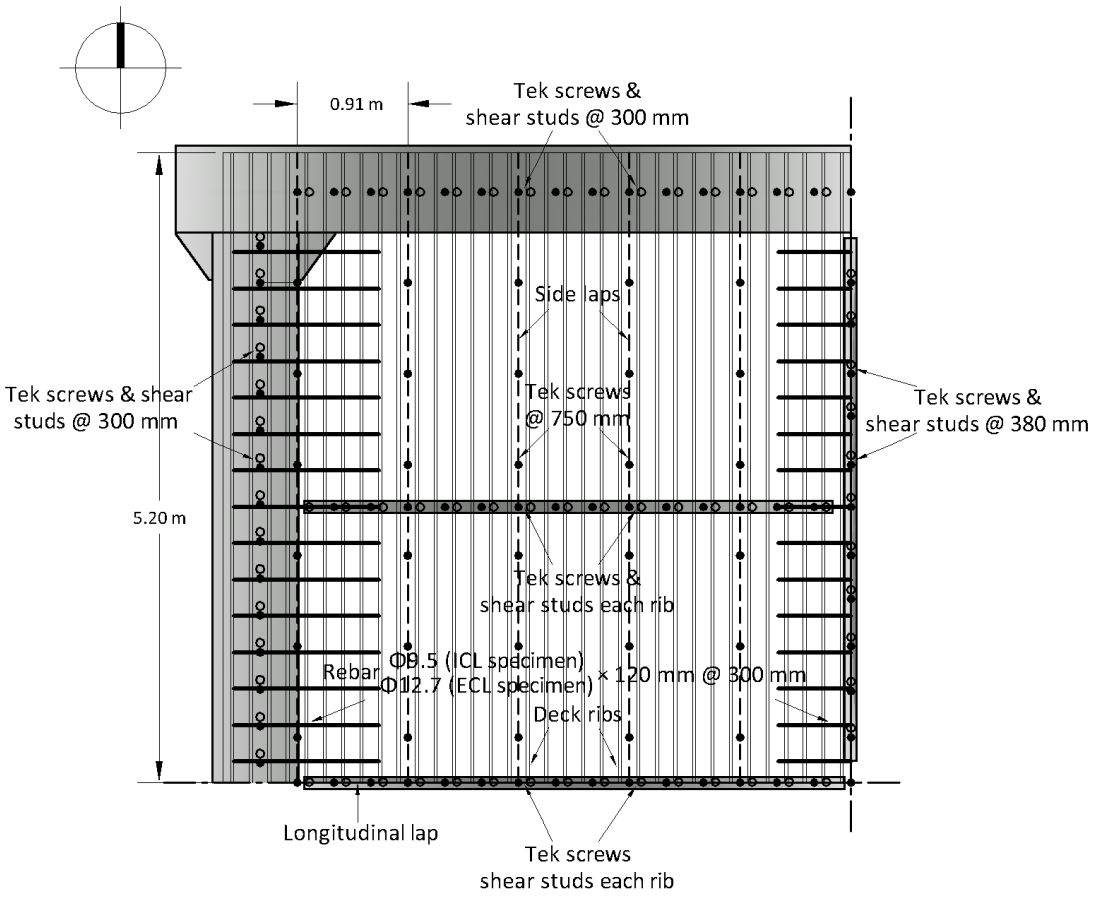

Figure 3.11: Design/construction details in a typical bay

3.4.5 Instrumentation

To measure the displacements, vertical string potentiometers were installed at the removed column location and at the mid-span of each beam. The displacements measured from the string potentiometers were intended to capture the profile of the deformed shape of the slab after the removal of the column. A total of twelve vertical potentiometers were used in the ICL test, and nine were used in the ECL test. In addition, a set of horizontal string potentiometers were attached on both sides of the top and bottom flange of each

beam framing into the removed column, which aimed to capture the connection behavior. The locations of these potentiometers are shown in Figure 3.12.

The strains at various locations of the steel grillage were measured with an array of strain gauges that were installed at multiple locations along the perimeter beam, the supporting grillage, and the exposed face of the corrugated steel decking, shown in Figure 3.12. The data gathered from the instrumentation were used to inform the validation procedure of the computational models described in the next chapter. Throughout this chapter, vertical displacement refers to the vertical displacement at the location of the center (removed) column relative to the original position before the column was removed.

A load-cell was used to measure the reaction at the middle column prior and during its static removal (Figure 3.7). Water containers were placed over the entire area of the specimens to approximate uniform loading conditions. A plan view of the locations of the water containers in the two specimens are shown in Figure 3.13. The exact volume of water placed into these vessels was measured remotely with flow meters.

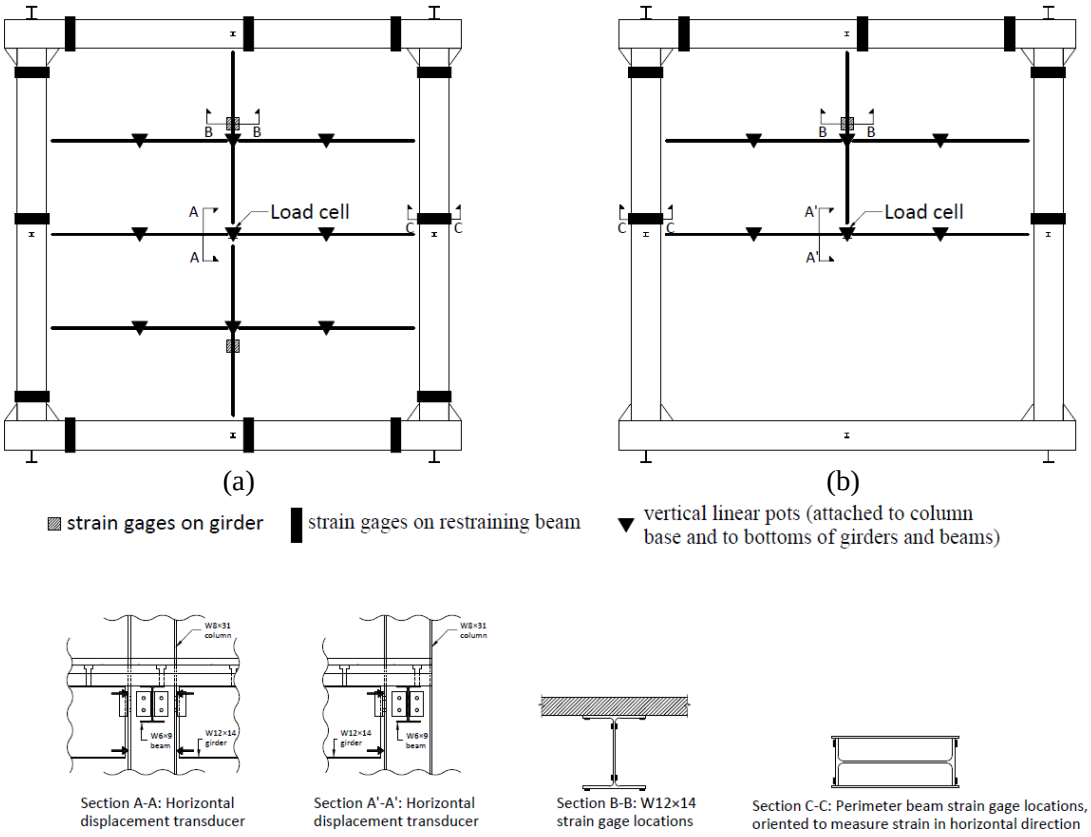

Figure 3.12: Instrumentation plan: (a) ICL specimen, (b) ECL specimen

3.4.6 Test Procedure

To simulate column removal in both specimens, the center column was discontinued 150 mm below the bottom flange of the W12×14 section (Figure 3.7), leaving 4 m clearance from the ground. The center column was supported laterally and was free to displace vertically (Figure 3.6), representing the restraints provided by the upper floors of a multi-story building. Initially, the slab was loaded with the DoD-recommended (2013) design load for progressive collapse (1.2×Dead + 0.5×Live), resulting in a total weight of 5.10 kN/m^2 (107 psf). The self-weight of the floor slab was

2.30 kN/m^2 (48 psf), and the remaining 2.80 kN/m^2 (59 psf) was added on the entire area of the slab before the removal of the column. For the ICL specimen, the additional load was approximated with sixty-four 1 m × 1 m × 0.60 m wooden buckets (Figure 3.13(a)); each one cast with a 1 m × 1 m × 0.15 m concrete slab (Figure 3.15). During the next stage of testing, the actuator was gradually released until the reaction measured at the load cell reached zero, requiring the slab to achieve a new equilibrium position without a centrally positioned column available to carry load. Next, with the central column no longer present, a specially designed irrigation system filled the remaining height of the buckets with water, bringing the total load on the slab to 8.00 kN/m^2 (167 psf). The irrigation system ensured a steady flow rate in all the water containers, and flow meters placed on the ground were monitored to determine the load acting on the slab. A similar procedure was followed for the ECL test specimen; however, the wooden buckets were replaced with two circular PVC-lined vessels, shown in Figure 3.13(b). To approximate the façade load for the ECL specimen, a row of ten concrete blocks was placed along the edge beam, imposing a 4.67 kN/m (320 plf) line load. Loading by means of adding water on top of the slab was continued until each specimen totally collapsed.

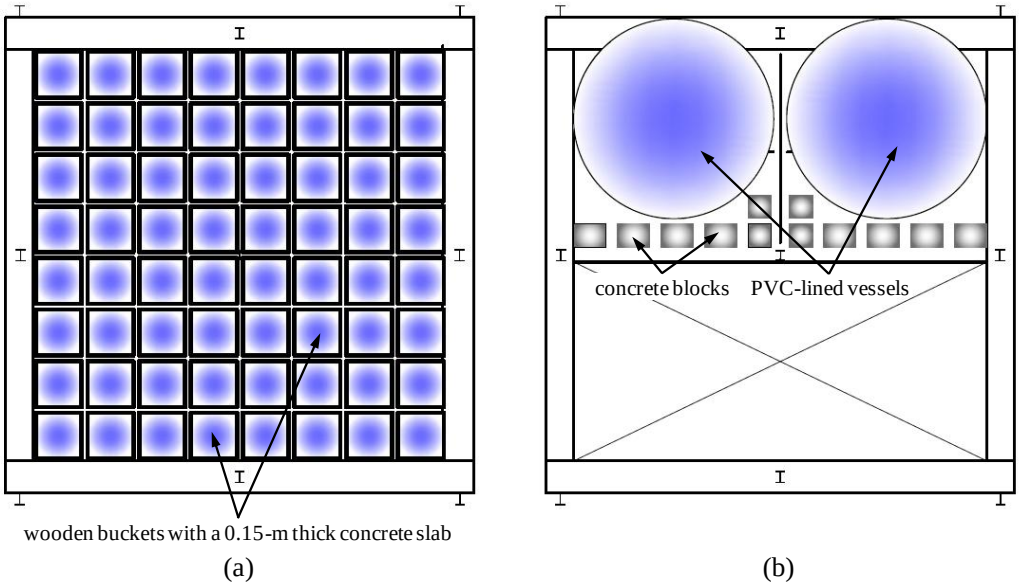

Figure 3.13: Plan view of the loading system: (a) ICL specimen, (b) ECL specimen

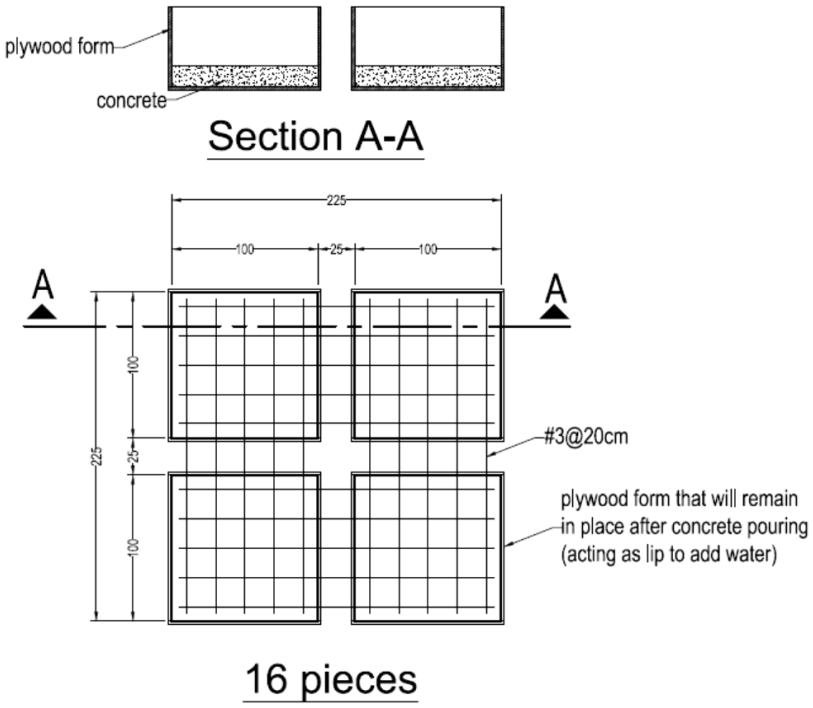

Figure 3.14: Detail of the loading system for the ICL specimen (dimensions in mm)

3.5 RESPONSE

3.5.1 Interior Column Loss Specimen

At the start of testing, the total weight on the floor slab was 5.75 kN/m^2 (120 psf), which is 0.65 kN/m^2 (13 psf) higher than the UFC load combination for progressive collapse (2013). Due to sagging of the corrugated steel deck during the concrete casting, the thickness of the slab in some regions was marginally higher when compared to its nominal thickness of 114-mm (Figure 3.9).

Under these loads, the recorded reaction was 120 kN. The actuator was gradually released until the recorded reaction dropped to zero. The actuator completely detached from the base plate of the center column (Figure 3.7) when the vertical displacement at that location reached 52 mm.

Figure 3.15 shows the recorded load-displacement curve while the actuator was gradually disengaged from the center column. After the central column was completely released, the floor slab had to bridge the double span of 9.10 m as shown in Figure 3.16. No failures were observed in the specimen apart from concrete cracking along the interior edge of the perimeter beam. With no additional load acting on the slab, the specimen remained with the center column unsupported until the deflections stabilized after approximately three hours. During that period, creep effects caused the vertical displacement to increase to 62 mm. The cause of the creep is speculated to be primarily attributed to the relative slip between the steel deck and the concrete due to the increased shear stresses that are developed after the column removal.

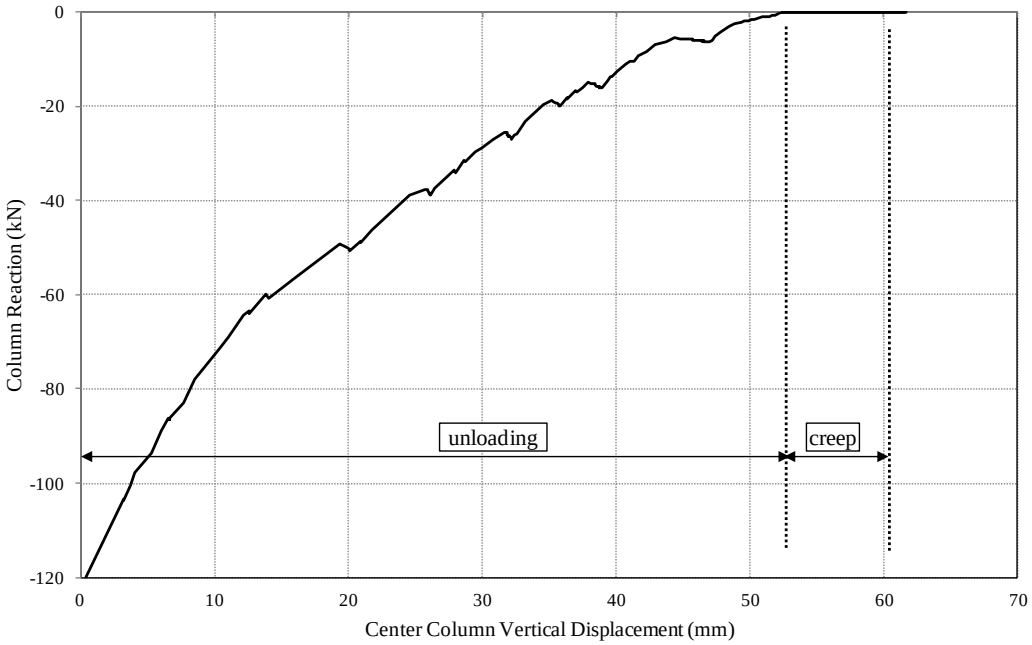

Figure 3.15: ICL specimen: Column reaction versus vertical displacement

Figure 3.16: ICL specimen after the removal of the mid-span support

Following this stabilization period, water was pumped into the wooden buckets (Figure 3.13 (a)). Due to water leaking in some of the buckets, water pumping was terminated when the load was increased by approximately 1.5 kN/m^2 (31 psf). The water was then drained from the buckets to repair the leaks. It is noted that even with the buckets empty, the vertical displacement increased to 82 mm under the total weight of 5.75 kN/m^2 (120 psf), 20 mm higher than that prior to the water loading. This residual deflection of 20 mm is mainly attributed to the spread of concrete cracking along the perimeter of the slab and plastic deformations in the steel member connections. After repairing the loading system, the second stage of testing was repeated. Once the buckets reached their maximum capacity, the superimposed load on the floor slab increased by 2.90 kN/m^2 (60 psf), and the vertical displacement increased by 28 mm. Ultimately, under a total weight of 8.65 kN/m^2 (180 psf) and a corresponding displacement of 110 mm, the floor slab remained in good condition. Apart from the increased width of the concrete cracks along the perimeter of the specimen, no failures were observed, and the steel connections were in good condition. Creep effects marginally increased the deflection by nearly 3 mm.

The capacity of the specimen exceeded the anticipated failure load, which was estimated using current progressive collapse guidelines (e.g., DoD 2009; GSA 2013) and accounting for dynamic loading effects. A detailed discussion concerning dynamic loading effects relative to the quasi-static data collected under this test program is described in a subsequent section of this chapter. Although the capacity of the loading system was limited and could not apply enough force to cause total collapse, the research team decided not to modify the loading system due to safety concerns. Rather, the

research team decided to re-test the specimen in a weakened condition. The water was drained from the buckets, and all twelve nuts connecting the steel beams framing into the center column were removed. By removing the nuts, the positive moments developed at those connections due to composite flexure action would vanish, reducing the capacity of the slab. Hoffman and Fahenstock (2011) demonstrated under a column removal scenario that such locations develop a force couple from bolts in tension and concrete in compression. Also, catenary action in the beams could no longer develop because they were now axially unrestrained at one end. This modification also fits into the context that in an actual column loss due to a blast or other extreme load, the connection might also experience some localized failure. Thus, initial damage may not be confined only to a single column.

After the nuts from the beams framing into the central column connection were removed, the load was increased again to 8.65 kN/m^2 (180 psf), and the vertical displacement was measured to be 160 mm. The specimen demonstrated significant softening at a deflection of approximately 140 mm. After terminating the water pumping, creep effects caused the deformations to increase until the vertical displacement stabilized at 185 mm after approximately three hours. The increased deformations were quite noticeable, though no signs of major failures were apparent. After the termination of loading, the water was drained from the buckets, decreasing the vertical displacement to 155 mm. Closer observations of the specimen showed the initiation of a new sign of failure. Approximately 1.20 m away from the center column, relative slip of the corrugated steel deck sheets in the east-west direction initiated along the longitudinal lap. Closer to the center column, the slip was nearly 18 mm, though it was nearly zero at a

distance of 1.20 m away from the center column. Figure 3.17 shows a close-up view of the slip at the longitudinal lap.

Because of the limited capacity of the loading system, the specimen was modified once more in a final attempt to quantify a lower bound for the ultimate capacity of the floor slab under the absence of the center column. For this test, all bolts from all steel connections were removed. All eight steel beams of the ICL specimen therefore hung from the concrete slab through the shear studs, and no shear forces or tensile forces could be transferred though the simple connections at either end. Water pumping initiated at a vertical displacement of 155 mm. Once the superimposed load increased by approximately 1 kN/m^2 (20 psf) and the displacement reached a vertical displacement of 165 mm, the deflections started increasing rapidly. The floor slab collapsed a few minutes later when the total load acting on the floor system was 7.90 kN/m^2 (165 psf). The vertical displacement just prior to collapse was 200 mm. A detailed investigation of video captured during the test revealed that the collapse was triggered from the failure of the longitudinal lap of the corrugated deck sheets. The signs of distress were quite clear from the previous tests because of the slip at the location as shown in Figure 3.17. Prior to the collapse and due to the large deformations, it is evident that membrane forces were developed in the concrete slab and the steel decking. The membrane in-plane forces were large enough that the longitudinal lap did not have adequate capacity to carry these tensile loads, causing total collapse of the slab.

Figure 3.18 shows a series of snapshots from the video footage of the specimen while collapsing, and Figure 3.19 shows the post-collapse condition of the specimen.

Starossek (2007) describes this type of collapse as zipper-type or section-type collapse. The complete load versus displacement curves for the three tests are shown in

Figure 3.20. It is noted that after at the end of each test, the water containers were drained before initiating the next test. Additional details for the ICL specimen are provided by Hull (2013).

Figure 3.17: Relative slip of the corrugated steel deck panels parallel to the longitudinal lap

(1) (2)

(3) (4)

Figure 3.18: ICL specimen: snapshots from video footage during collapse, east view

Figure 3.19: ICL specimen after collapse

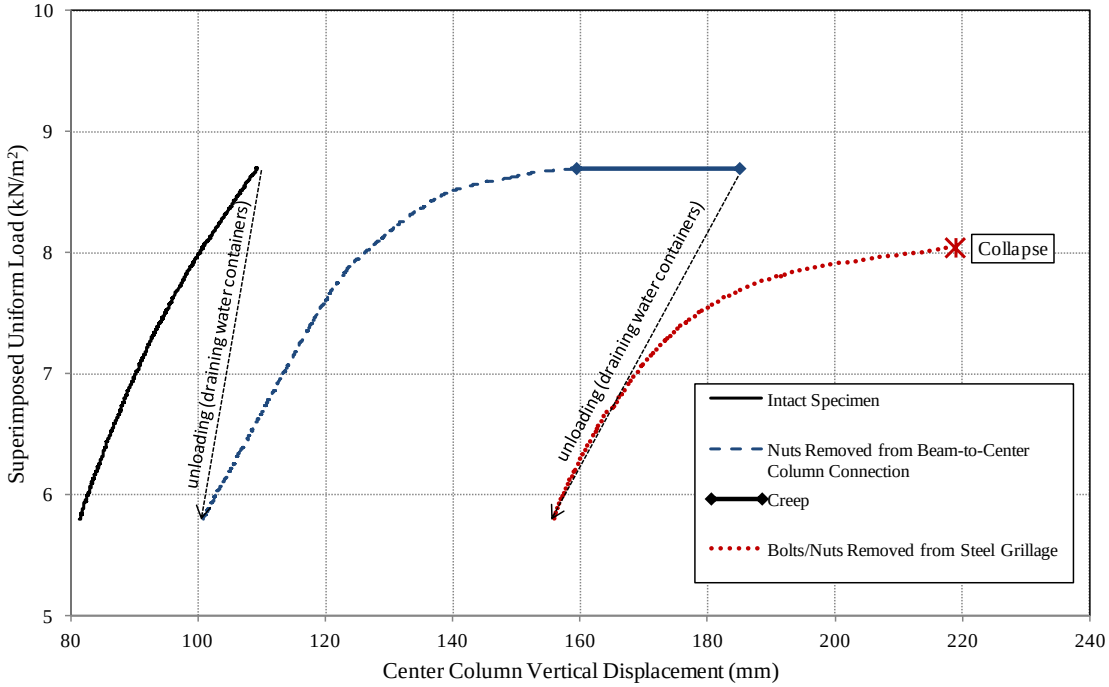

Figure 3.20: ICL specimen: Superimposed load versus vertical displacement after the removal of the support at the center column

3.5.2 Exterior Column Loss Specimen

Based on the ICL tests, the research team felt it necessary to increase the capacity of the loading system. As such, rather than using wooden buckets, two large circular PVC-lined vessels were used for the ECL specimen. The façade load at the exterior edge of the specimen was approximated with a row of twelve concrete blocks, resulting in a load of 4.67 kN/m (320 plf) (Figure 3.13 (b)). During casting of this specimen, shoring measures were taken to reduce sagging of the steel deck to ensure the thickness of the concrete slab would be close to its nominal thickness of 114-mm. Before the removal of the exterior column, adequate water was pumped into the swimming pools to reach the

UFC load combination for progressive collapse (2013). At this point, the total weight of the floor slab and water was 5.50 kN/m^2 (115 psf), which is 0.38 kN/m^2 (8 psf) higher than the UFC load for progressive collapse.

Under these loads, the recorded reaction of the load cell at the center column was 65 kN. The actuator was gradually lowered. Once the recorded reaction dropped to zero, the vertical displacement of the center column was 120 mm. The slab was now in a new equilibrium position without the vertical support at the center column location. Figure 3.21 shows the recorded load-displacement curve while the actuator was gradually disengaged from the specimen. It is noted that the spikes in this curve occurred because the actuator was lowered in increments of 12 mm. At the end of every increment, the lowering process was halted until the reactions and deflections stabilized to a constant value. Once the actuator fully disengaged from the center column, the vertical displacement stabilized to a value of 128 mm. Figure 3.22 shows the condition of the specimen after the full disengagement of the actuator.

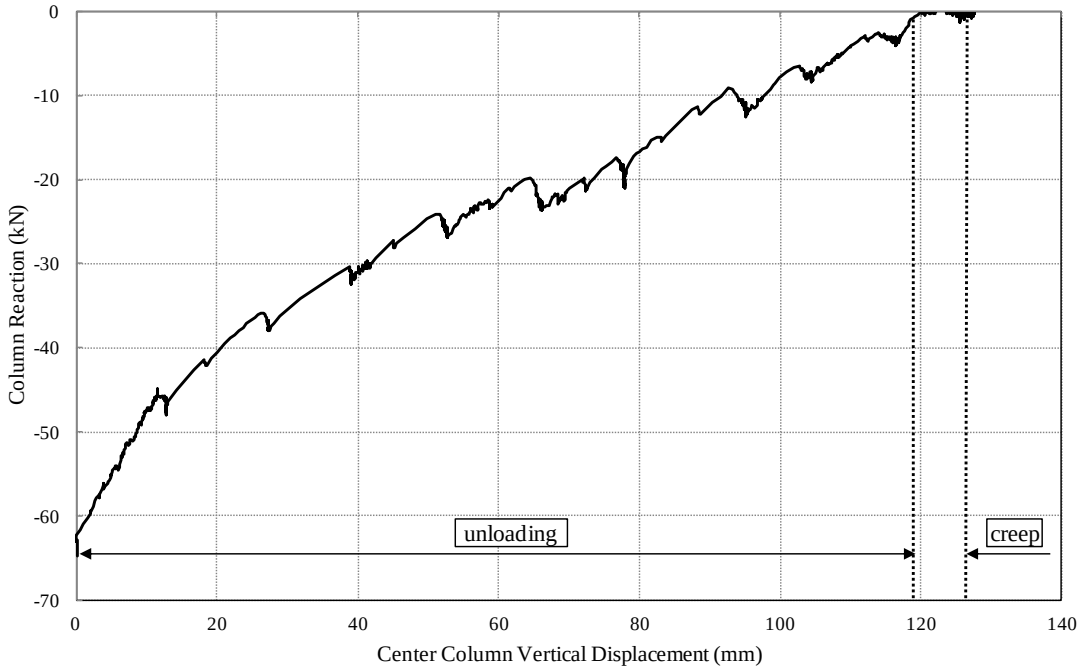

Figure 3.21: ECL specimen: Column reaction versus vertical displacement

Figure 3.22: ECL specimen after the removal of the mid-span support

During the next stage of testing, water was pumped into the swimming pools, thereby increasing the load acting on the slab. The superimposed load was increased in increments of 1 kN/m^2 (20 psf). Once the deflections stabilized, another load increment was added to the slab. The specimen demonstrated significant softening once the vertical displacement at the location of the center column reached a value of 320 mm. The floor slab collapsed moments later when the total weight was 9.10 kN/m^2 (190 psf). The vertical displacement just prior to collapse was 340 mm. No major failures were observed before collapse, though close observations of the specimen during testing were prohibited due to safety concerns. The load versus displacement curve for the superimposed loading is shown in Figure 3.23. It is noted that the flat parts of this curve correspond to the incremental increase of the loading and the corresponding creep because deflections increased under constant load. Figure 3.24, Figure 3.25, and Figure 3.26 show the collapse event in a series of snapshots taken from the video footage. Additional details for the ICL specimen are provided by Moutsanidis (2014).

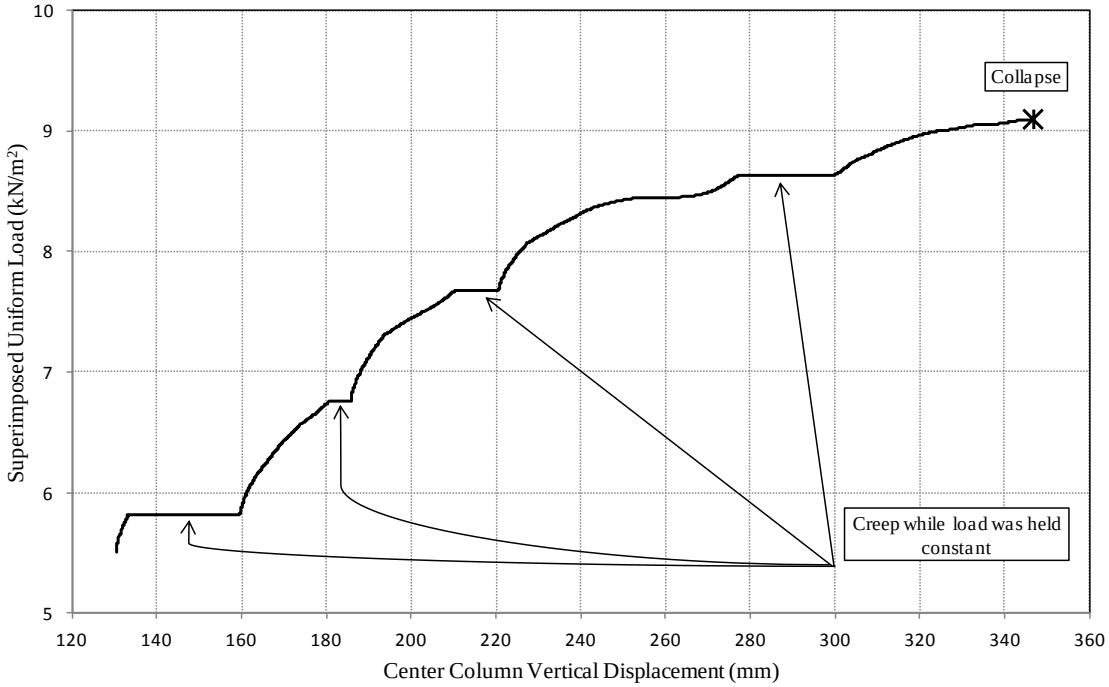

Figure 3.23: ECL specimen: Superimposed load versus vertical displacement after the removal of the support at the center column

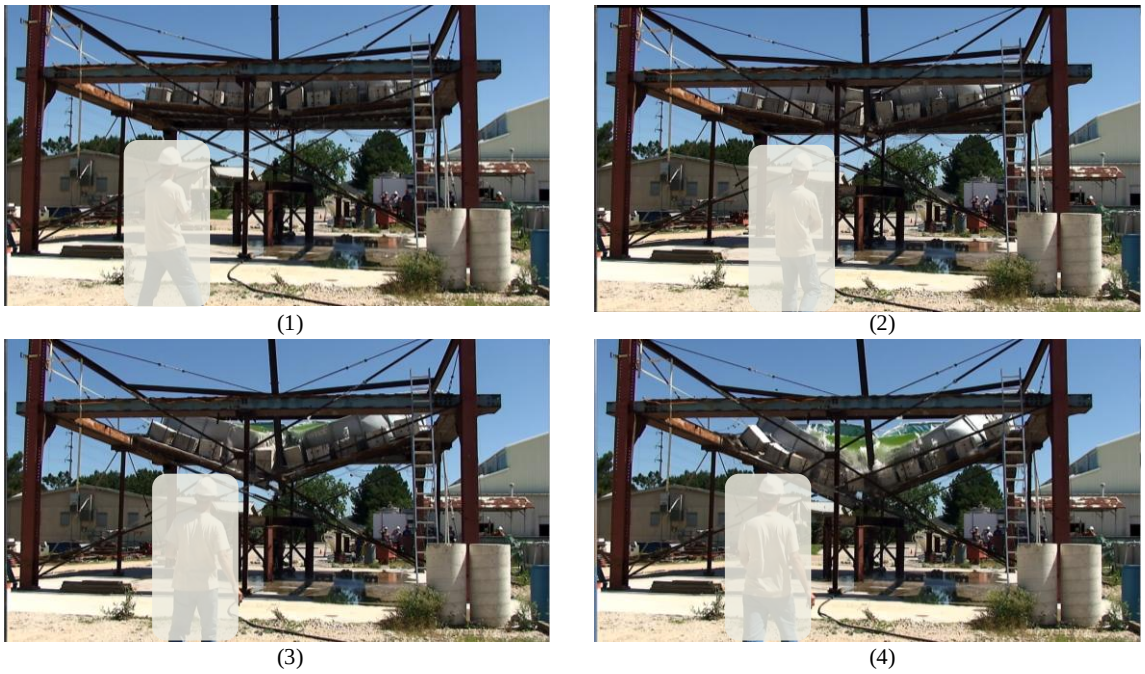

(1) (2)

(3) (4)

Figure 3.24: ECL specimen: snapshots from video footage during collapse, north view

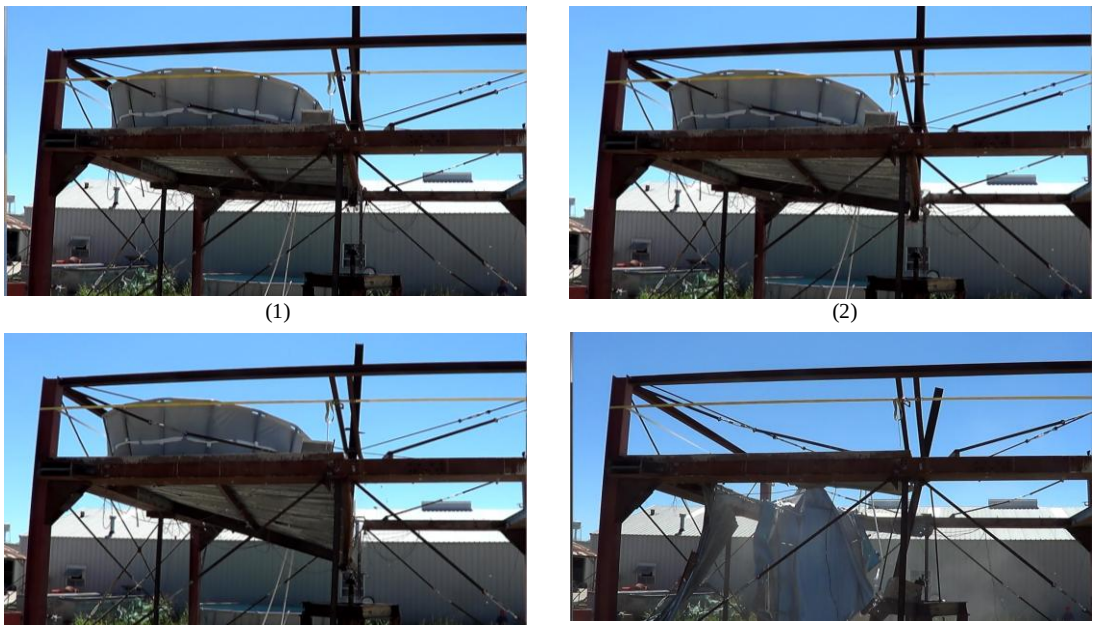

(1) (2)

(3) (4)

Figure 3.25: ECL specimen: snapshots from video footage during collapse, east view

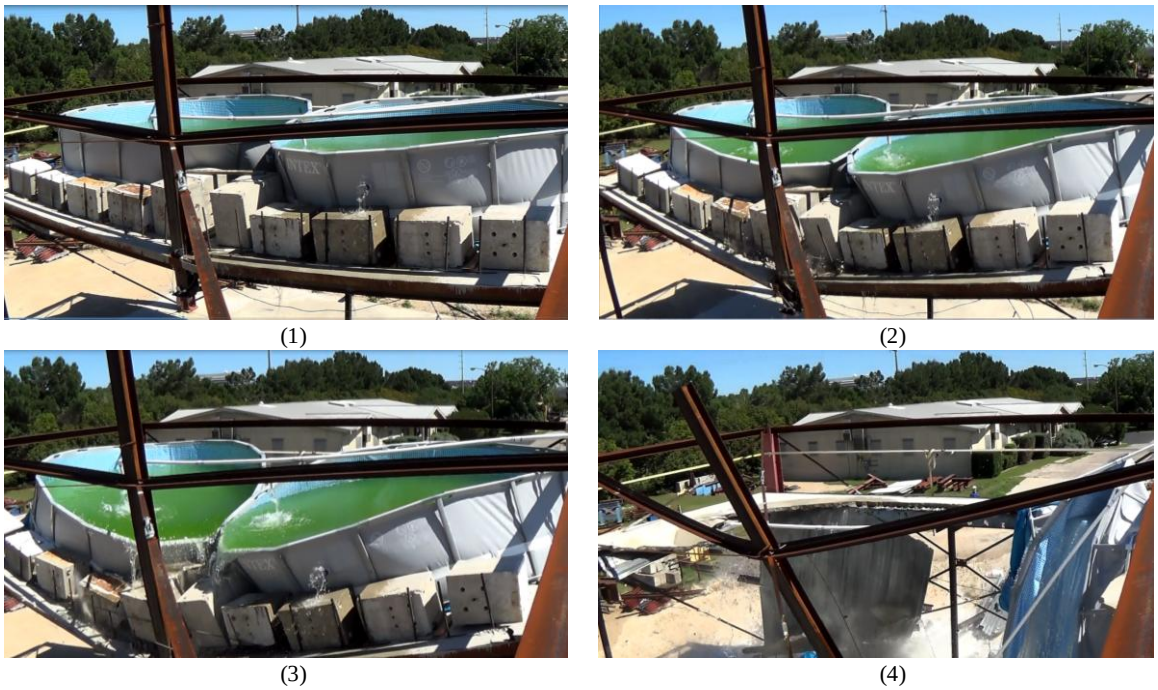

(1) (2)

(3) (4)

Figure 3.26: ECL specimen: snapshots from video footage during collapse, northwest view

3.6 DYNAMIC EFFECTS

Both tests were performed under quasi-static loading conditions. Damage events resulting in the sudden loss of a column (e.g., blast loads or vehicle impact) have dynamic effects associated with them. The methodology suggested by the DoD guidelines (2013) was followed to account for the associated dynamic effects following a column loss. The gravity loads acting on the floor slab were multiplied by an appropriate dynamic increase factor (DIF). The DIF was estimated based on the steel framing connection types and the chosen structural response level — "Collapse Prevention or Life Safety" as described in the DoD guidelines (2013). For the floor systems tested, the required DIF was computed to be 1.2 for both response levels. Therefore the amplified

load that the ICL specimen would be required to carry is 5.75 kN/m^2 × 1.2 = 6.9 kN/m^2 (144 psf), and the ECL specimen would need to carry 5.5 kN/m^2 × 1.2 = 6.6 kN/m^2 (138 psf) to account for dynamic load effects. Both specimens carried a higher load prior to collapse, which suggests both specimens had sufficient capacity to sustain the DoD design load (2013) for progressive collapse including the associated dynamic effects.

3.7 CHAPTER OVERVIEW

This chapter presented the experimental procedure and the main observations regarding the response of the two specimens tested. The specimens performed well and demonstrated appreciable amounts of reserve capacity prior to collapse. Both specimens successfully absorbed the removal of the center column under the DoD recommended design load of 5.10 kN/m^2 (107 psf). At a second stage, they sustained additional load that exceeded their UDL of 7.74 kN/m^2 (162 psf), even under the absence of one column. The dynamic effects associated with the instantaneous removal of a column were accounted for using the DoD guidelines (2013). The amplified load was 6.9 kN/m^2, and both specimens sustained even higher loads prior to their collapse; 7.90 kN/m^2 (165 psf) for the ICL specimen and 9.10 kN/m^2 (190 psf) for the ECL specimen. It is noted that the ICL specimen initially supported a load of 8.65 kN/m^2 (180 psf) and did not collapse. Ddue to the limited capacity of the loading system, the specimen was weakened by removing all the bolts of the supporting grillage. It finally collapsed at a load of 7.90 kN/m^2 (165 psf).

CHAPTER 4

NUMERICAL MODELING

4.1 INTRODUCTION

A series of high fidelity finite element (FE) analyses were performed to simulate the response of the experimental tests presented in the previous chapter. Detailed three-dimensional models were developed for this purpose. These numerical models were able to explicitly capture the global response of the experimental tests (e.g., deformations and overall collapse) and the local damage that occurred to individual components (e.g., steel fracturing and concrete cracking). Solid elements were used to represent the concrete floor slab, steel beams, connection parts and bolts, shell elements were used to represent the corrugated metal decking, and beam elements were used to represent the reinforcing steel and shear connectors. The models were analyzed using the multi-physics code LS-DYNA (Hallquist 2013) by employing the explicit solution scheme. Because composite floor slabs consist of a number of different components, a thorough validation study was performed for each one of these individual components to ensure that the modeling parameters employed could reasonably capture their response. In the last section of this chapter, a sensitivity study is presented, which identifies the contribution of the various components in the response of the composite floor system. Throughout this chapter, certain LS-DYNA keywords used in the analyses are reported with an asterisk '*' followed by the keyword in block capitals. The complete input cards for the FE models presented in this chapter can be found in Appendix A.

4.2 INDIVIDUAL COMPONENT STUDIES

A series of preliminary analyses were performed on the individual components that make up a typical composite floor system. These analyses were intended to ensure the modeling parameters and procedures followed could predict floor system response with reasonable accuracy. Previously available experimental data on these components were used as a basis for the validation studies, which focused on double angle connections, single plate shear-tab connections, and concrete slabs.

4.2.1 Double Angle Connection

A typical double angle beam-to-column connection is shown in Figure 4.1. The beam (shown in yellow) is connected to the double angles (shown in red) by first welding the three edges of the angle to the web of the beam (shown in black). Then, the angles are attached to the column (shown in green) with bolts (shown in magenta). In some cases, the legs of the angle are bolted to the beam web instead of being welded.

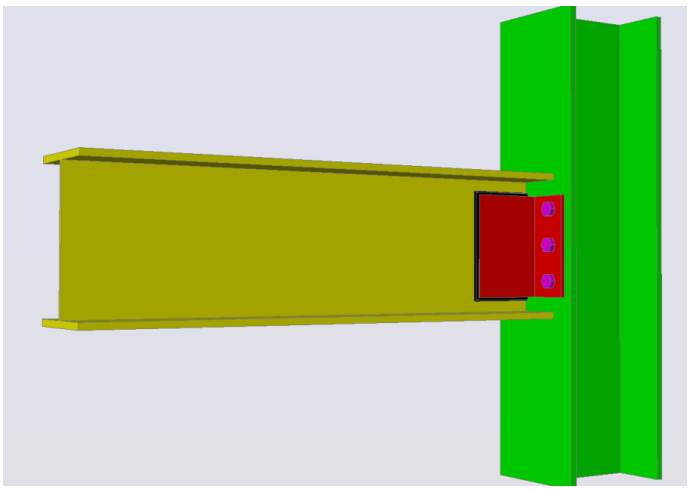

Figure 4.1: Typical beam-to-column double angle connection

Lewitt, *et al.* (1966) performed a series of experimental tests on double angle beam-to-column connections. These data were used to ensure the modeling procedure followed was able to predict the experimental response with acceptable accuracy. The connection assembly considered for validation purposes is shown in Figure 4.2(a) and is denoted as "specimen FK-3" (Lewitt*, et al.* 1966). The assembly was tested by applying a vertical load to the column, with the two beams constrained by rollers. From this test, the moment/rotation behavior of the connection was obtained.

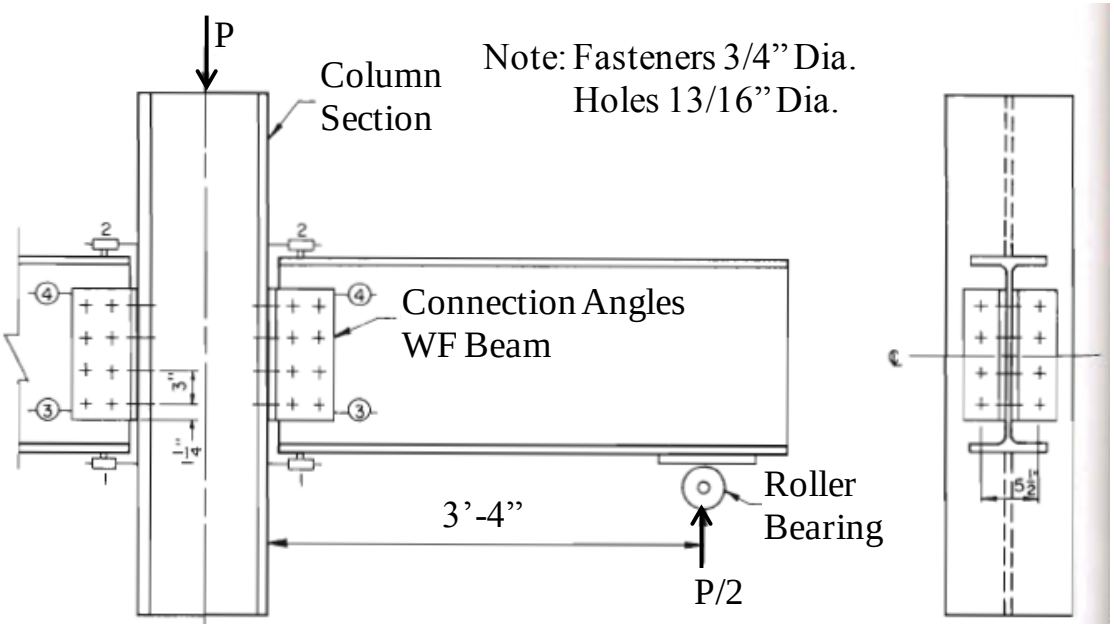

(a)

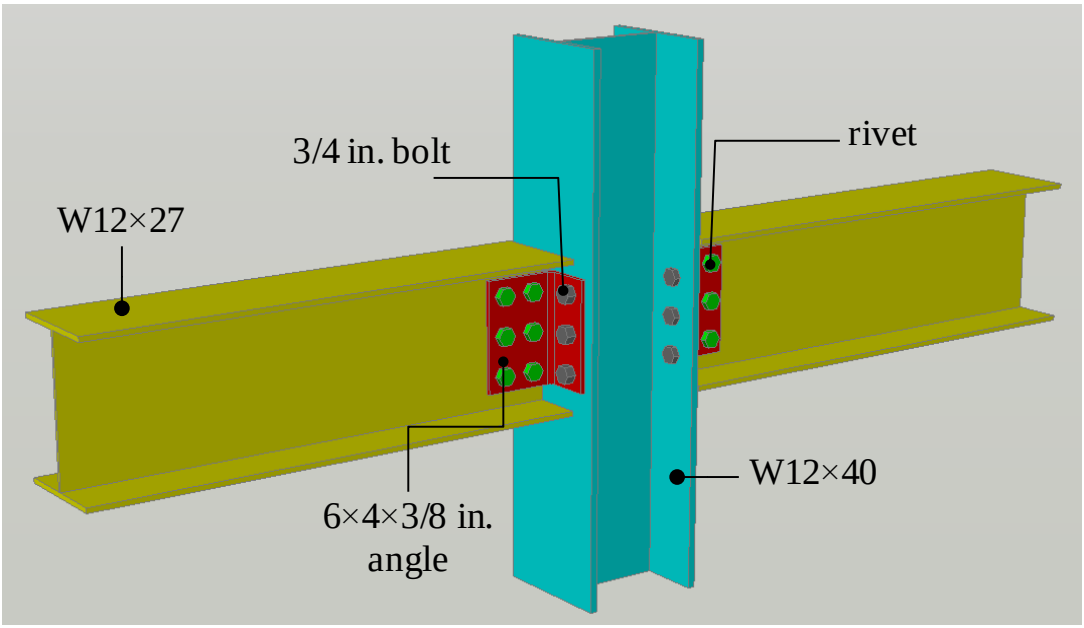

(b)

Figure 4.2: Specimen FK-3: (a) Test setup (Lewitt, *et al.* 1966), (b) Isometric view

Figure 4.2(b) shows the member sizes of the specimen. The beams were 40-in. (1-m) long W12×27 sections, the column was a W12×40 section, and the angles were 6×4×3/8-in. (152×102×9.53-mm), 8.5-in. (216-mm) long. The bolts were 3/4-in. (19.1-mm) in diameter and consisted of A325 steel. The remaining connection parts consisted of A36 steel. The web was attached to the double angles using six rivets, and six bolts were used to attach the double angles to the beams.

Four-node tetrahedral elements with one integration point, shown in Figure 4.3, were used to model the entire specimen, (*SECTION_SOLID, elform = 10). Based on symmetry, only the left half of the specimen was considered. Figure 4.4 shows the FE model of the specimen. For computational efficiency, the mesh was refined in locations expected to experience significant deformations. The angles, bolts, beam flange, and column web were finely meshed with 3-mm long tetrahedral elements (Figure 4.4). After a convergence study was conducted, this element size was found to be adequate to capture the response of the connection with good accuracy. The mesh size was gradually increased in regions of the specimen where deformations were limited. The beams responded primarily as rigid bodies because of the considerably larger moment of inertia of the beam sections compared to that of the two angles, which was approximately five times larger. The interaction between the different connection components was explicitly captured by defining a penalty-based contact procedure (*CONTACT_AUTOMATIC_SINGLE_SURFACE) with a static friction coefficient of 0.50 as suggested by AISC (2014). The dynamic coefficient of friction was reduced to 0.35, although relative slip between connection parts was not expected to occur.

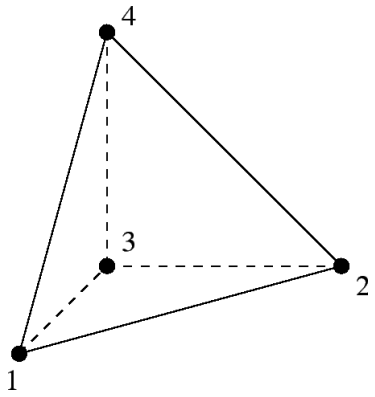

Figure 4.3: Four-node tetrahedral element

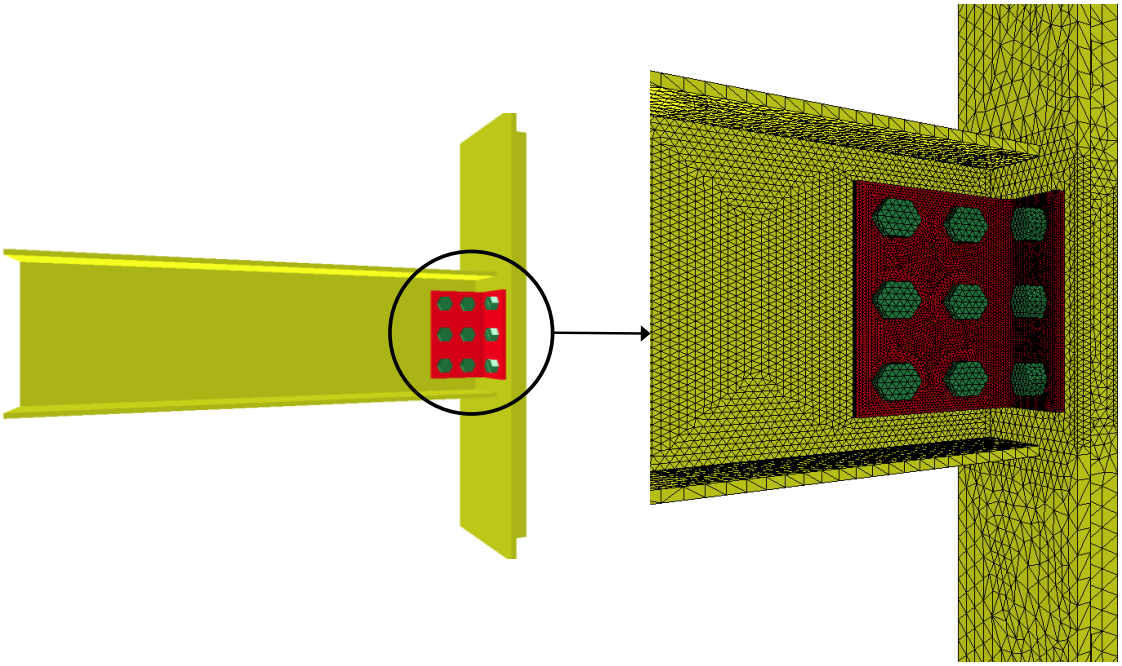

Figure 4.4: FE model of specimen FK-3

The Piecewise Linear Plasticity Model (*MAT_PIECEWISE_LINEAR_PLASTICITY) was used for all steel components. The

steel properties used for these materials were based on ASTM standards and information given in the report by (Lewitt, *et al.* 1966). The authors gave tension test results for the angle sections shown in Table 4.1. In lieu of complete stress-strain curves for the angle, wide flange section, and bolt material, control points as suggested by ASTM standards were used to develop stress-strain curves that were used as input to the material model.

Specimen Number	Angle Size	Fillet Radius, in.	Leg, in.	Angle Thickness, in.	Elongation in 8 in., per cent	Reduction in Area, per cent	Lower Yield Point. ksi	Ultimate Strenght, ksi
FK-3, FK-4AB, FK-4P, WK-4	6×4×3/8	1/2	4	0.352	28	54	39.3	62.5
			6	0.357	31	51	41.3	65.4
FK-4AB-M	6×4×3/8	1/2	4	0.375	-	-	43.1	62.5
			6	0.375	-	-	40.1	60.6
FB-4, FB-4A	4×3-1/2×3/8	3/8	4	0.373	33	55	38.9	60.2
			3-1/2	0.370	33	52	38.8	59.6
FK-5	6×4×7/16	1/2	4	0.451	29	52	37.2	63.6
			6	0.436	28	52	36.4	63.8
WB-10AB	4×4×7/16	3/8	4	0.440	27	57	40.1	68.8
			4	0.440	27	57	40.1	68.8

Table 4.1: Connection angle properties, (Lewitt, *et al.* 1966)

In the FE model, concentrated loads were applied (*LOAD_NODE_SET) to all nodes on the front face of the beam, as depicted in Figure 4.5. The column was restrained against displacement in all directions, simulating similar restraint conditions as in the experimental tests. The analysis was conducted using the explicit solution scheme. The selective mass scale option was enabled for computational efficiency (*CONTROL_TIMESTEP, dt2ms = -3E-6). To ensure quasi-static loading conditions were appropriately represented, a series of analyses were performed using different loading rates to ensure dynamic effects were negligible. For each load rate, the maximum vertical displacement at the tip of the beam was used as an index to find the maximum

possible load rate capable of simulating quasi-static loading conditions. Table 4.2 summarizes the peak displacements at different load rates. It is evident that at higher load rates the dynamic effects are noticeable. A load rate of 15 kN/s was found to simulate static loading conditions with reasonable accuracy and was adopted for the subsequent analyses. It is noted that analyses were also performed using the implicit static solver. However, because the analyses for the experimental tests were planned to be performed using the explicit solution scheme due to the highly non-linear response of the specimens, especially during collapse, it was desirable to ensure that parameters associated with this solution method were calibrated accordingly.

Load Rate (kN/s)	Peak Vertical Displacement (mm)	Difference from Previous Disp. (%)
240	83.70	
120	71.24	17.48
60	64.70	10.12
30	62.10	4.19
15	62.75	1.05
7.5	62.15	0.97

Table 4.2: Peak vertical displacement at different load rates

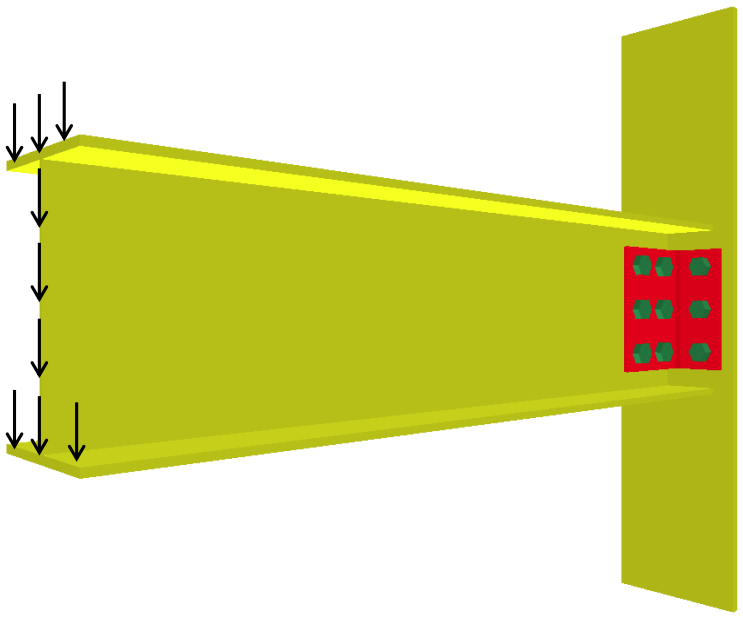

Figure 4.5: Application of load at the nodes of the front-face of the beam

Figure 4.6 shows the moment/rotation curves for this specimen obtained from the experimental tests and along with those from the analyses performed using LS-DYNA. In general, good comparison can be observed between the experimental data and the response of the FE model. The discrepancy of the initial stiffness of the connection in the FE model is attributed to the gap closure between the bolts and the bolt holes. As presented in the report (Lewitt*, et al.* 1966), the 3/4-in. (19.1-mm) diameter bolts were positioned within 13/16-in. (20.6-mm) diameter bolt-holes. In the computational model, the bolts and the bolt-holes were centered. Until contact was established between all the bolts and the corresponding bolt-holes, the computed initial stiffness was somewhat less than the experimentally measured one. The reduction of the connection stiffness after a rotation of approximately 0.10 radians is the point at which the angle starts to unfold as shown in Figure 4.7. At rotations less than 0.10 radians, show limited deformation,

whereas for rotations greater than 0.10 radians, the angles start to unfold by detaching from the column flange.

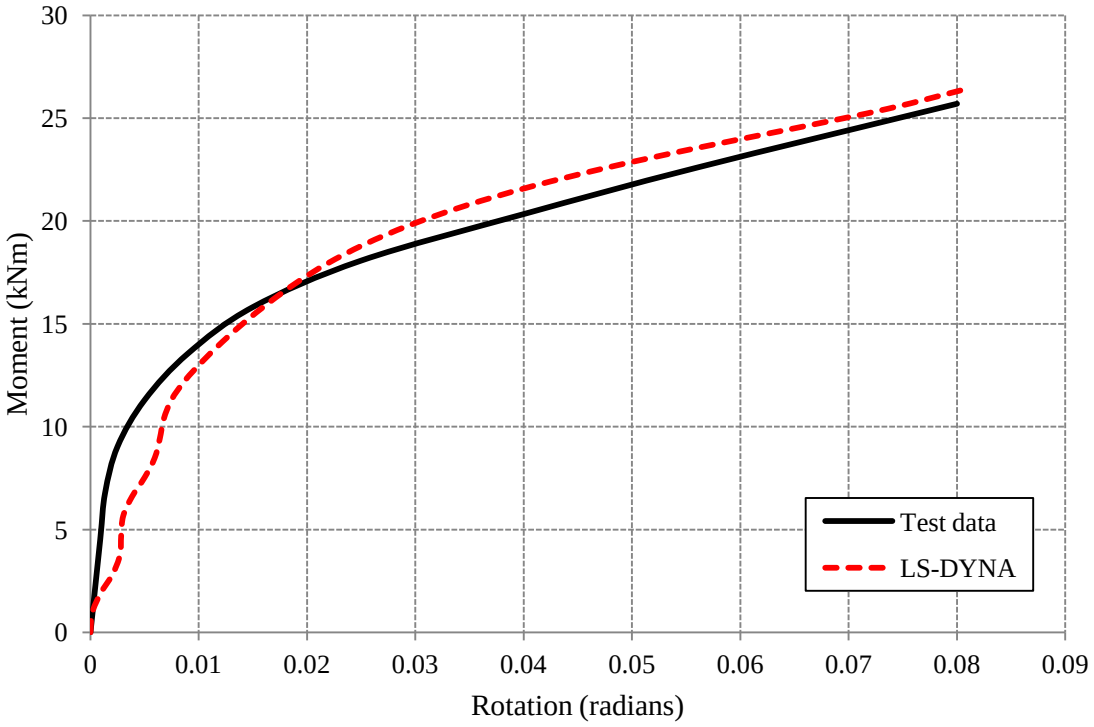

Figure 4.6: Moment/rotation curves for "specimen FK-3", (Lewitt, *et al.* 1966)

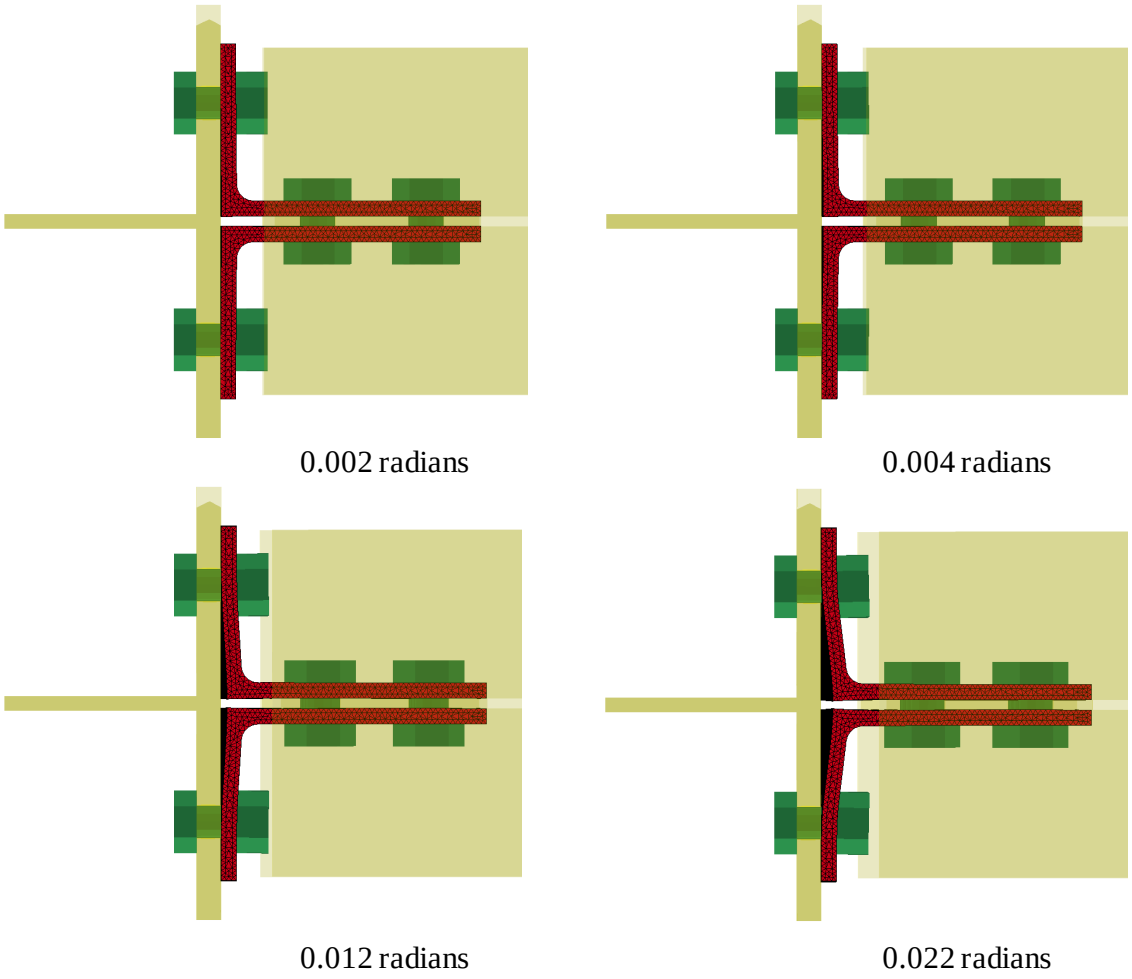

Figure 4.7: Angles unfolding under increasing connection rotation (some parts are transparent for clarity)

Further analyses on this specimen identified the importance of the fillet radius between the two legs of the angle sections. The angles in this specimen had a 1/2-in. (12.7-mm) fillet radius. A series of analyses were performed using different fillet radii—no fillet, 1/2-in. (12.7-mm), and 5/8-in. (15.9-mm). Figure 4.8 shows the computed moment/rotation curves for the different fillet sizes. Although the initial stiffness remains

largely unaffected by the size of the fillet radius, the fillet radius significantly affects the response of the connection after the angle starts to unfold (Figure 4.7). This result is particularly important within the context of analyses for progressive collapse scenarios because such connections are expected to experience relatively large rotations. Therefore, particular attention must be given to accurately modeling the fillet radius of angles. In the subsequent analyses of the experimental tests, shown in Section 4.3, the nominal fillet radius of the angles utilized for the steel connections was included in the models. The fillet radius for these angles was 1/4 in. (6.35 mm).

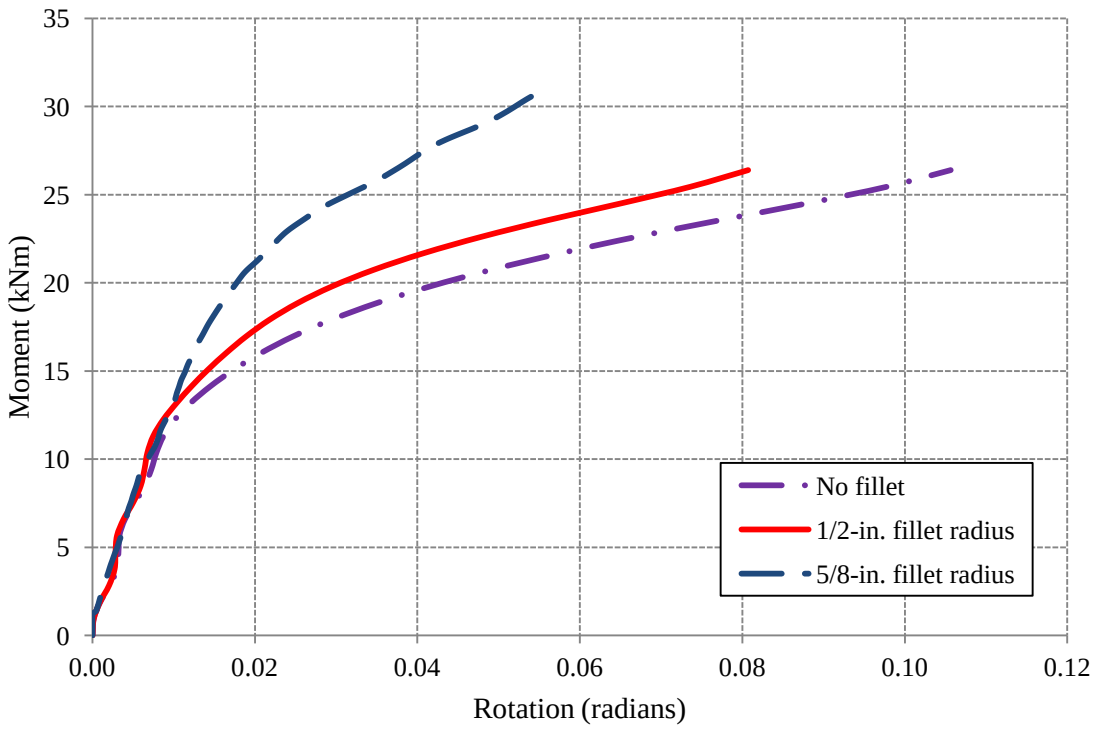

Figure 4.8: Moment/rotation response curves for different fillet radii of the angle section

4.2.2 Shear Tab Connection

Figure 4.9 shows a typical single-plate connection, commonly known as shear tab connection. Simple shear tab connections typically consist of a single steel plate (shown in red) that is welded (shown in black) to a column (shown in green) on one end and bolted to a beam (shown in yellow) on the other end. Shear tabs are also used to join beams to other beams or girders.

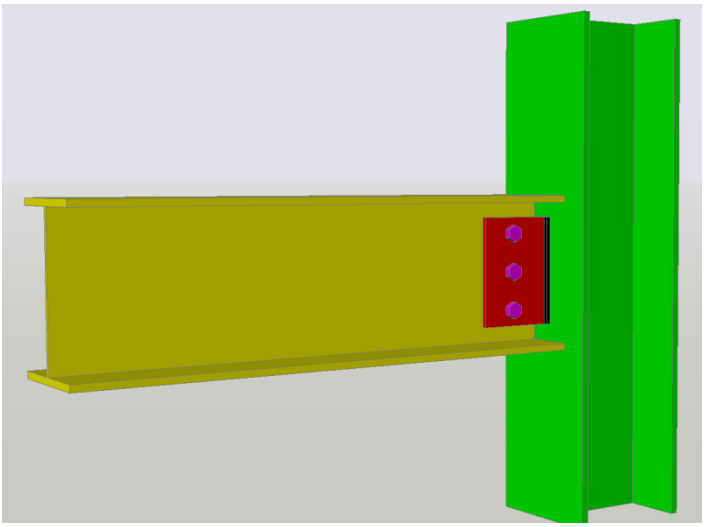

Figure 4.9: Typical beam-to-column shear tab connection

A series of experimental tests were performed at The University of Texas at Austin on shear tab connections (Guanyu 2011). Figure 4.10 shows dimensional and geometric properties of the connection tested in pure tension. Another specimen was tested in inclined tension, shown in Figure 4.11. The inclined tension specimen was intended to evaluate the response of the connection under a combination of tensile and shear forces, because the inclined tension can be decomposed into components that are

acting parallel and perpendicular to the longitudinal axis of the specimen, as depicted in Figure 4.11. The specimens consisted of W12×26 sections made from A992 steel and a 3/8-in. (9.53-mm) thick steel plate made from A36 steel. A325 3/4-in. (19.1-mm) diameter bolts were used in both specimens. The wide flange sections and steel plates were welded to two thick plates with 1/4-in. (6.4-mm) fillet welds.

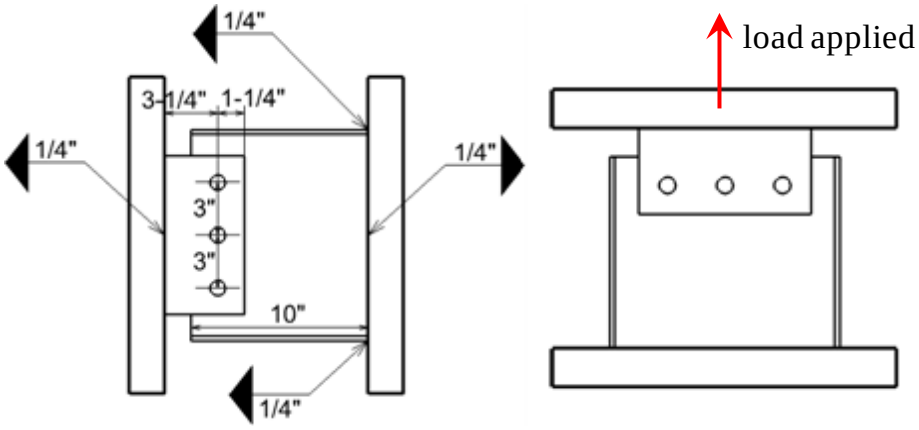

Figure 4.10: Axial tension test specimen dimensions, (Guanyu 2011)

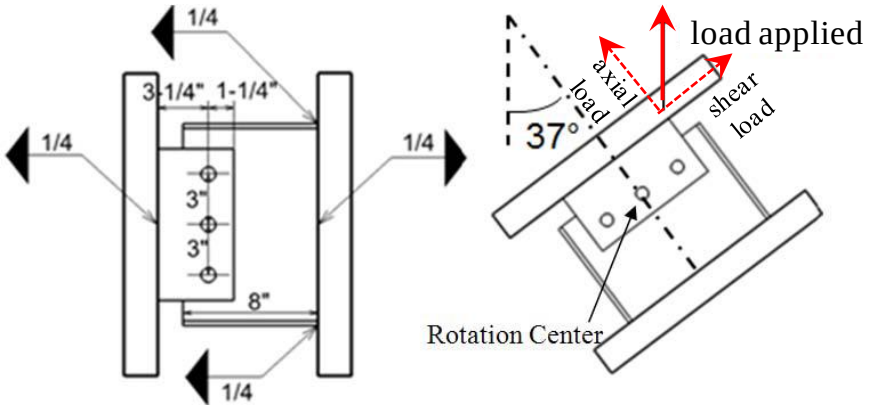

Figure 4.11: Inclined tension test specimen dimensions, (Guanyu 2011)

Tension tests were performed to determine the material properties of the steel parts used in the specimens. Data from these tests were used to define the input parameters of the material properties used in the computational models. Attention was given to the steel material properties at high strain values through the initiation of fracture because the connections were tested until failure. Coupons in the testing program (Guanyu 2011) were fabricated and tested in accordance with ASTM Standard A370 (ASTM 2012) to obtain the actual material properties of the wide flange section and the steel plate used in the specimens (Figure 4.10, Figure 4.11.). Figure 4.12 shows the dimensions of the tension coupon. A coupon with geometry identical to the one tested in tension was modeled in LS-DYNA, shown in Figure 4.13. The FE model was discretized with four-node tetrahedral elements (*SECTION_SOLID, elform = 10) with a 3-mm edge length. The size of the elements was equal to the size of the FE mesh used to model the test specimens of (Guanyu 2011). The coupon was loaded in tension in a nearly identical manner as the actual tension tests (i.e., displacement controlled, quasi-static load in tension). The Piecewise Linear Plasticity Model (*MAT_PIECEWISE_LINEAR_PLASTICITY) was used to model the steel behavior.

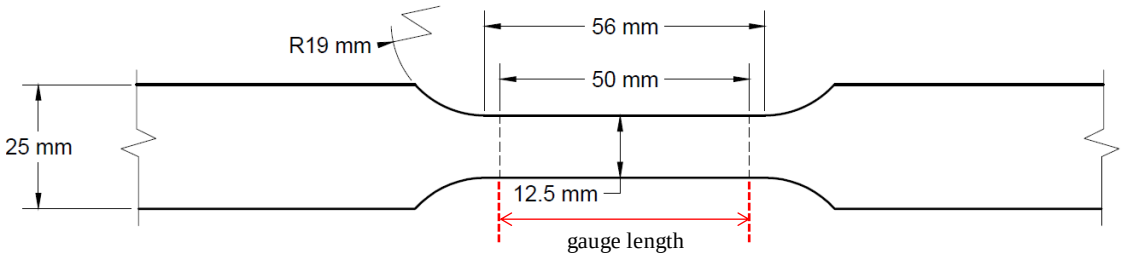

Figure 4.12: Standard size coupon specimen (ASTM 2012)

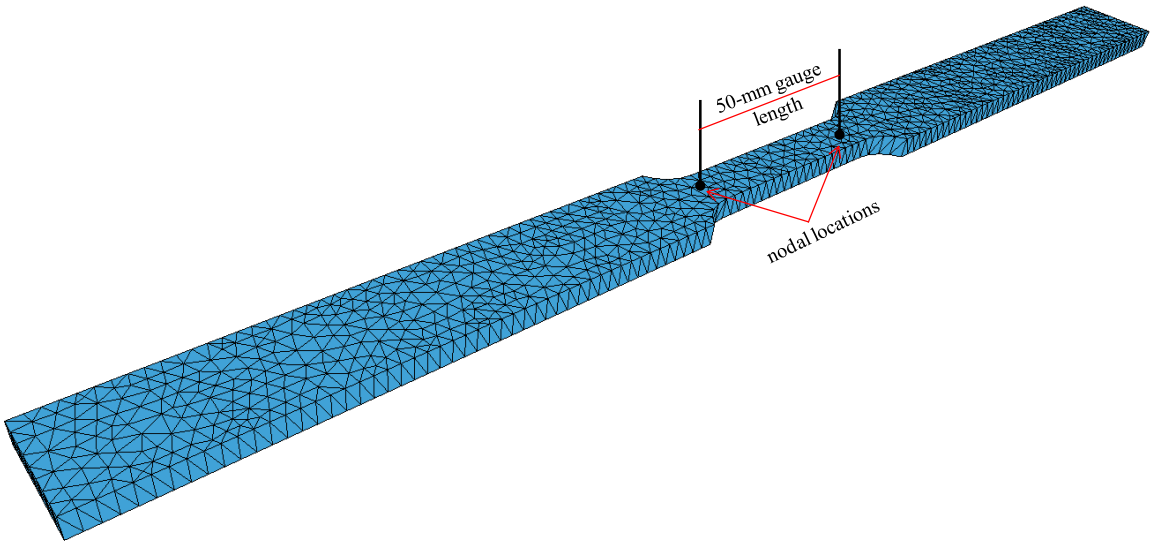

Figure 4.13: FE model of standard size coupon

The actual engineering stress-strain curves, obtained from the uniaxial tension tests, were used as a basis to extract a set of engineering stress-strain values that precisely followed these curves. These values were then converted to true stress-strain values (Beer*, et al.* 2011) and were used as input parameters for the material model used in LS-DYNA. The conversion was required because the input stress-strain values for the Piecewise Linear Plasticity model are entered as sets of true stresses and effective plastic strains. The effective plastic strain is the residual true strain after unloading elastically. After performing the analysis, the engineering stress-strain curve of the computational model was obtained by measuring the load and the corresponding relative displacement between two nodes that had a distance equal to the 50-mm gauge length of the actual tension tests, as depicted in Figure 4.13. A "trial and error" procedure was followed so that the input parameters were such that the obtained engineering stress-strain curve after running the analysis of the uniaxial tension test was nearly identical to the actual one.

These analyses were performed to obtain accurate input values for the shear tab and the W12×26 wide flange section that were used in the specimens.

Figure 4.14 shows the plastic strain values at different stages of the analysis for the W12×26 section material properties. Fracture of steel was simulated by enabling the embedded element erosion criterion (fail) on the material model used to simulate the steel behavior. Elements that exceeded the specified effective plastic strain of 0.53 were deleted from the FE model. Figure 4.14 (b) shows the fractured coupon after some of the elements at the fractured location were eroded (deleted) from the model. The value of plastic strain criterion was such that the computational coupons fractured at the same deformation level as the actual coupon tests. The complete stress-strain curves of the materials are shown in Figure 4.15 and Figure 4.16, respectively, for the W12×26 section and the 3/8-in. (9.53-mm) thick shear tab. In the same figure, three stress-strain curves are shown: (a) the one obtained from the actual coupon tests, (b) the input set of true stress-strain values used in the FE analysis, and (c) the obtained engineering stress-strain curve from the analyses in LS-DYNA. It can be seen that both the experimental and computational engineering stress-strain curves are in good agreement. Because tension tests are not reported for the 3/4-in. (19.1-mm) diameter bolts, the input parameters for the bolts were based on the control points as suggested by the ASTM standards for A325 bolts.

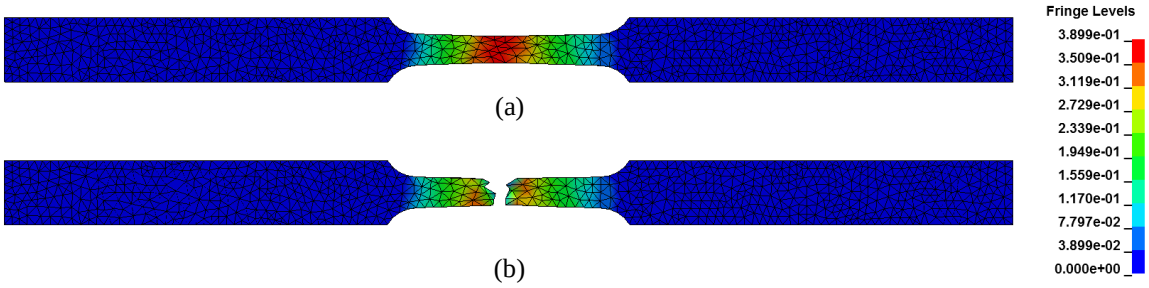

Figure 4.14: Plastic strains under uniaxial tension, (a) Maximum elongation, (b) After fracture

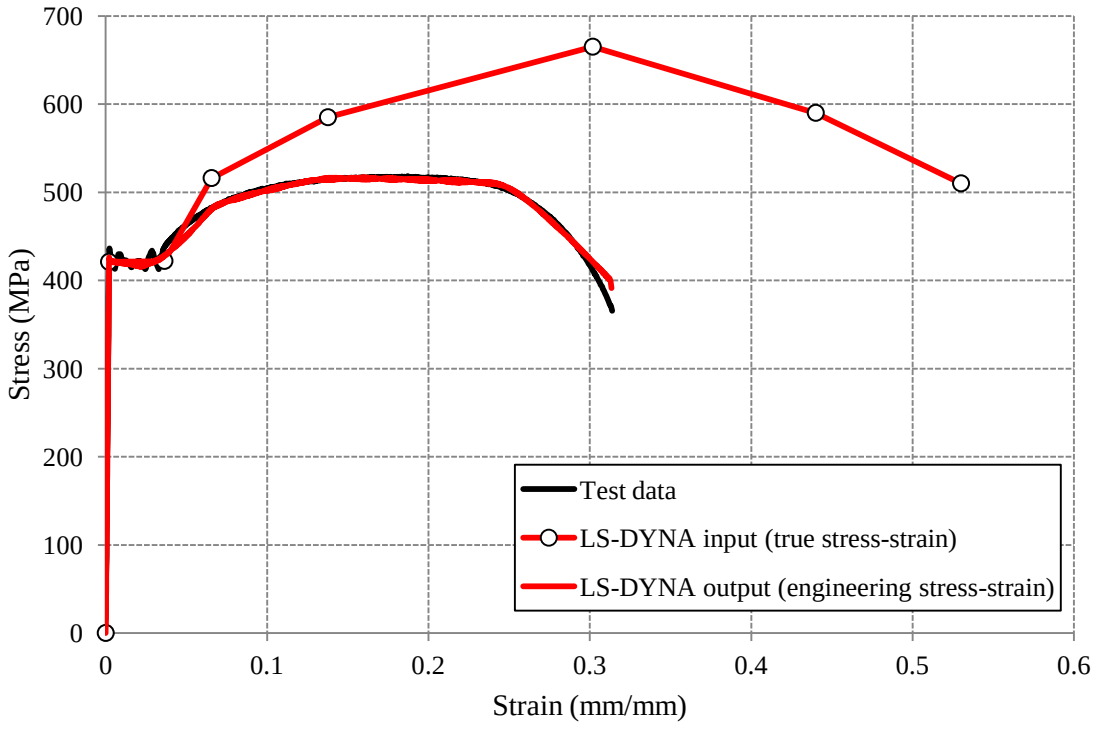

Figure 4.15: Stress-strain curve for the W12×26 section

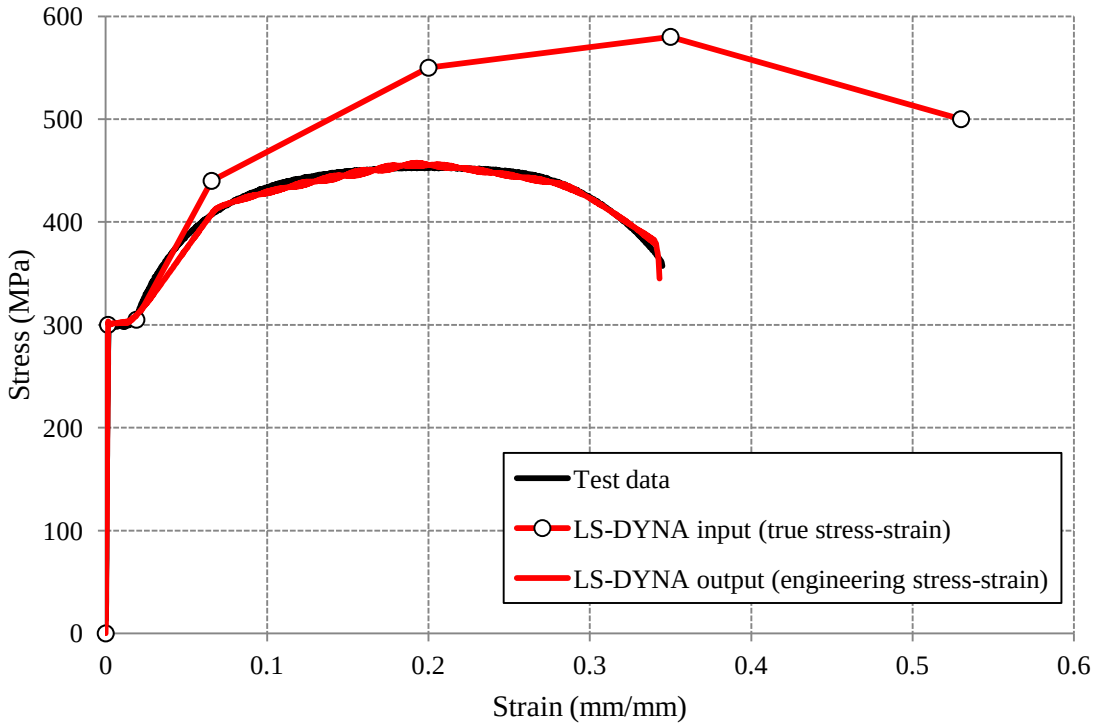

Figure 4.16: Stress-strain curve for the 3/8-in. (9.53-mm) thick shear tab

Figure 4.17 shows a view of the FE model of the specimen tested under axial tension. Four-node tetrahedral elements with 3-mm long edges were used in the vicinity of the bolts because significant plastic deformations were expected in this region. The mesh size was gradually increased moving away from this region. Load was applied by means of a prescribed translation (*BOUNDARY_PRESCRIBED_MOTION_SET) at the middle row of nodes on the top plate as shown in Figure 4.17. The same row of nodes on the bottom plate was restrained against all translational degrees of freedom. This approach allowed the specimen to rotate freely about its transverse axis, simulating similar loading and boundary conditions as the experimental tests (Guanyu 2011). Figure

4.18 shows a picture of the test setup and depicts the points that the specimen was allowed to rotate freely about.

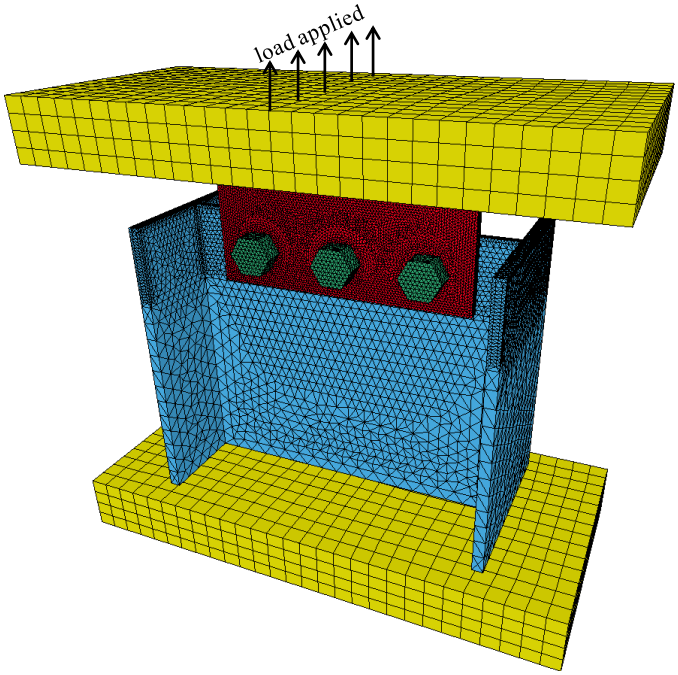

Figure 4.17: FE model of the specimen tested under axial tension

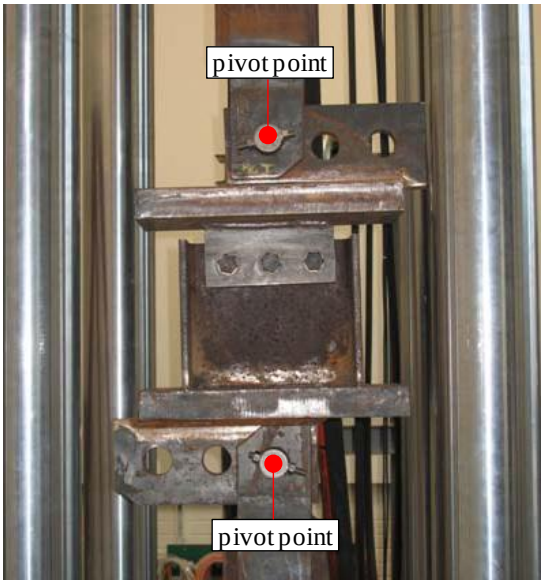

Figure 4.18: Test setup of the specimen tested in axial tension, (Guanyu 2011)

Because the specimens were expected to fail by bearing in the beam web, as observed during the experimental tests, special attention was given to the contact definition employed in the analyses. Because the computational model was capable of simulating fracture of steel by deleting elements that exceeded a specified plastic strain value, elements in the beam web were expected to erode. Default contact algorithms account for contact only at the exterior boundary of the elements. Because some elements at the exterior boundary of the beam, shown in Figure 4.19, were expected to erode, a new exterior boundary would then be defined by a different set of elements that were exposed after the erosion of existing elements. Therefore, a special contact algorithm was employed (*CONTACT_ERODING_SINGLE_SURFACE, erosop = 1, iadj = 1) that was capable of reestablishing contact after erosion of elements at the exterior boundary of the model. Figure 4.19 shows the progression of failure at the bolt-hole of the beam web. As

the bolt shaft bears against the bolt-hole, elements erode and contact is maintained because the contact definition at the exterior boundary of the bolt-hole is redefined. The inclined tension test specimen (Figure 4.11) was modeled with a similar procedure.

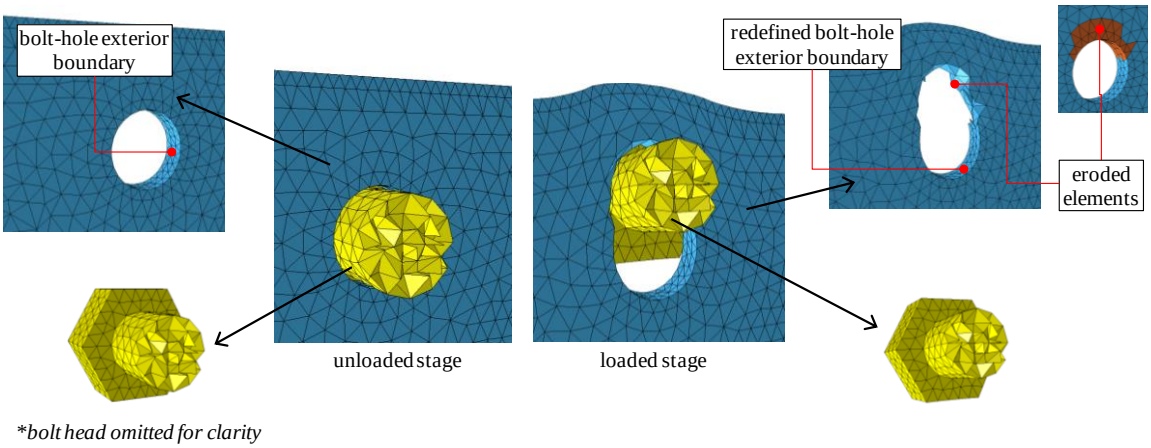

Figure 4.19: Bolt shaft bearing against the bolt hole at the beam web

Figure 4.20 and Figure 4.21 show a comparison of the load-displacement curves obtained from the LS-DYNA analyses for the connections under axial tension and inclined tension, respectively. In both cases, the initial stiffness is predicted with reasonable accuracy. The overall response, however, shows a significant deviation between the measured and computed values shortly after the initial elastic response. These differences might be attributed to variations in how the tear-out failure propagates in the analysis model as compared to the actual tests. In the FE model, the elements in front of the bolt face that bear against the hole start eroding as their failure strain is reached. The eroding of these elements leads to rapid changes along the load-displacement curve. As elements begin to erode, the contact forces acting against the bolt

decrease. As the overall displacement increases by a few millimeters (i.e., the length of an element), the bolt begins to bear against the element behind the one eroded previously. In the tests, however, the failure propagation is different. Nonetheless, similar load paths are presented by Main and Sadek (2011) for simulations of bearing failure. Therefore, the modeling approach adopted may not allow an accurate representation of the actual failure propagation. Comparing the area under the experimental and computational curves, which is an index of the strain energy absorbed as deformations increase, there is reasonably good agreement. For the connection under axial tension, the ratio of the computational to the experimental energy is approximately 1.1. For the connection under inclined tension, the ratio is 1.3. In both cases, the computational analyses over-predict the absorbed energy by 10%-30%. Nonetheless, for progressive collapse analyses, this issue might not be crucial because the contribution of the steel grillage and the stiffness of the connections are practically negligible compared to the contribution of the concrete slab and the corrugated decking, as previously demonstrated by Sadek, *et al.* (2008). Moreover, the ultimate displacement that the connection can sustain before total failure occurs is predicted with reasonable accuracy, which is expected to be of significant importance in predicting the overall response of the composite floor system under a column removal scenario. Thus, despite the differences between the measured and predicted results, the approach adopted for the current study is consistent with previous research and is expected to be sufficiently accurate for the objectives of this study. Future research, however, should consider alternative ways to efficiently model bearing failures and fracture of steel connections within the context of large computational models used to predict floor system collapse.

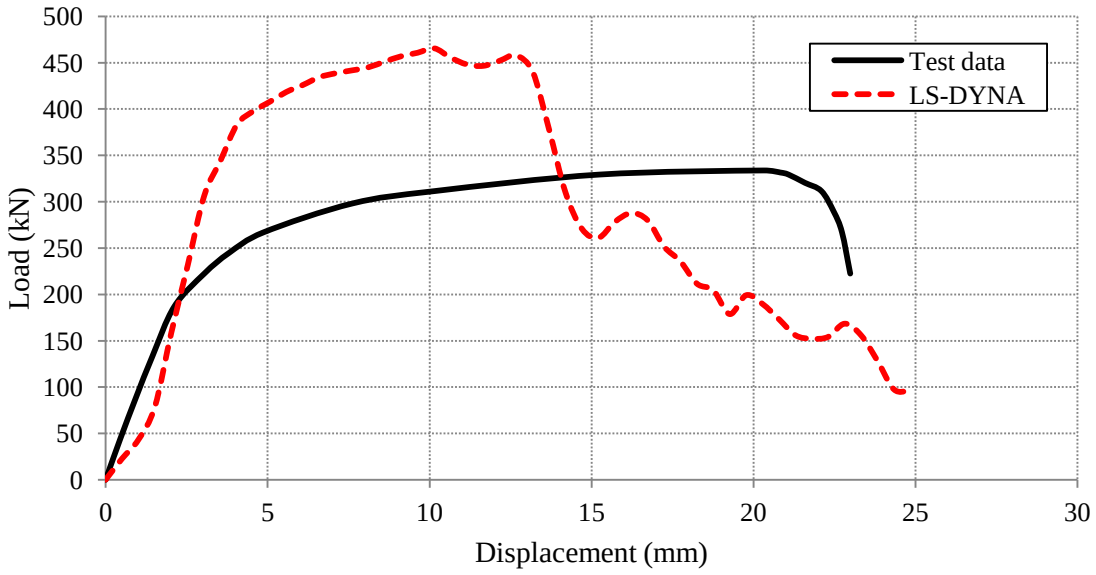

Figure 4.20: Load-displacement comparison between LS-DYNA and test for connection under axial tension

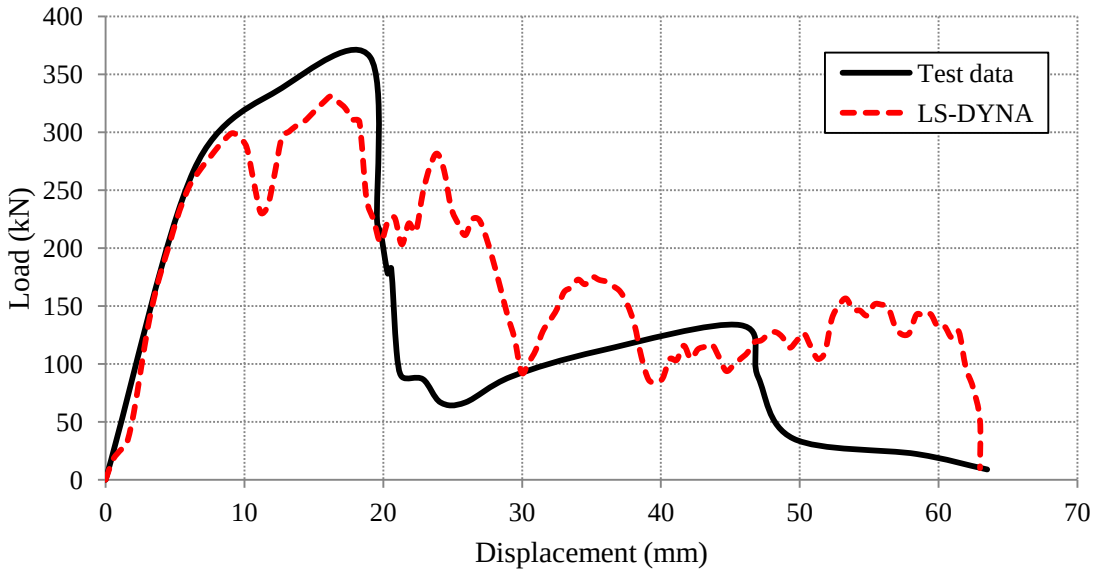

Figure 4.21: Load-displacement comparison between LS-DYNA and test for connection under inclined tension

Figure 4.22 and Figure 4.23 show a comparison between the failure modes observed in the tests and those predicted from the computational analyses. The failure modes are quite similar, and the bearing failure in the beam web is captured in both cases. Further, no significant plastic deformations are developed in the bolts or the shear tab plate. These observations provide confidence that this modeling approach is suitable for progressive collapse analyses, because such failure modes are likely to be observed under the extreme loading conditions associated with column removal scenarios.

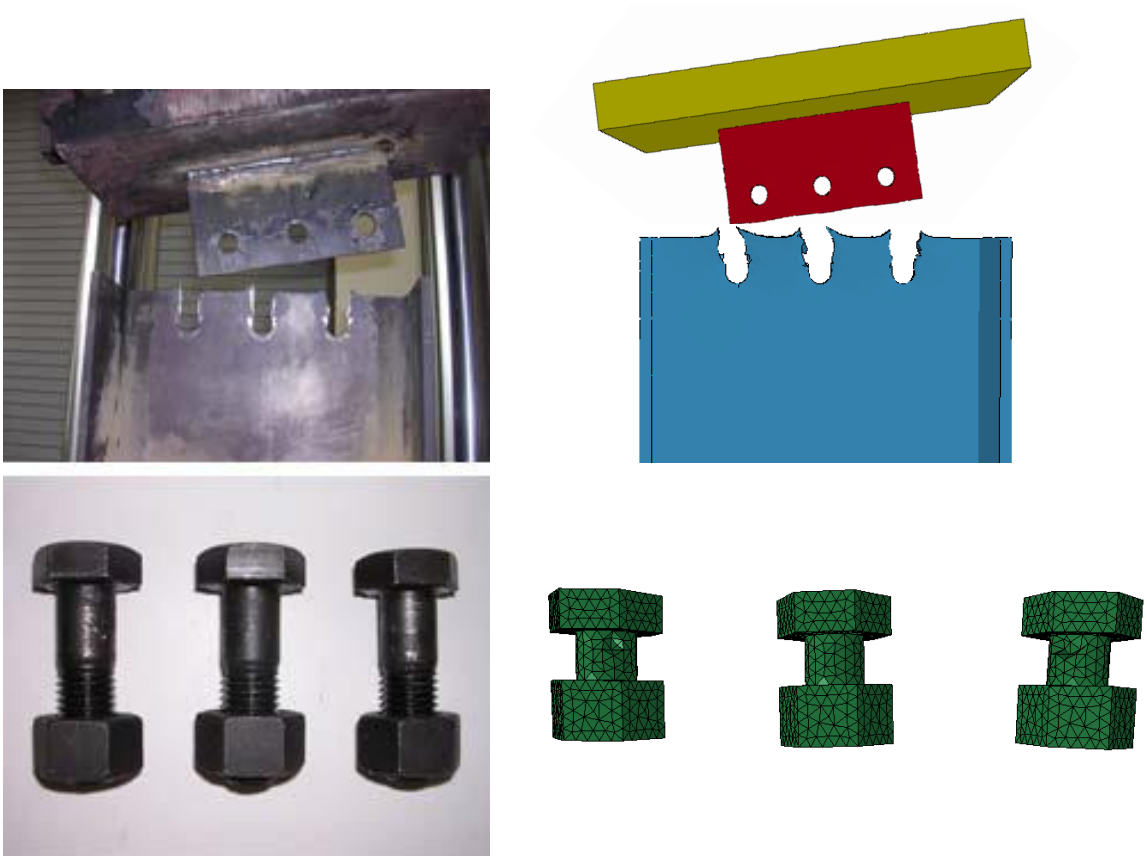

(a) (b)

Figure 4.22: Comparison of connection failures for axial tension: (a) Test, (b) LS-DYNA

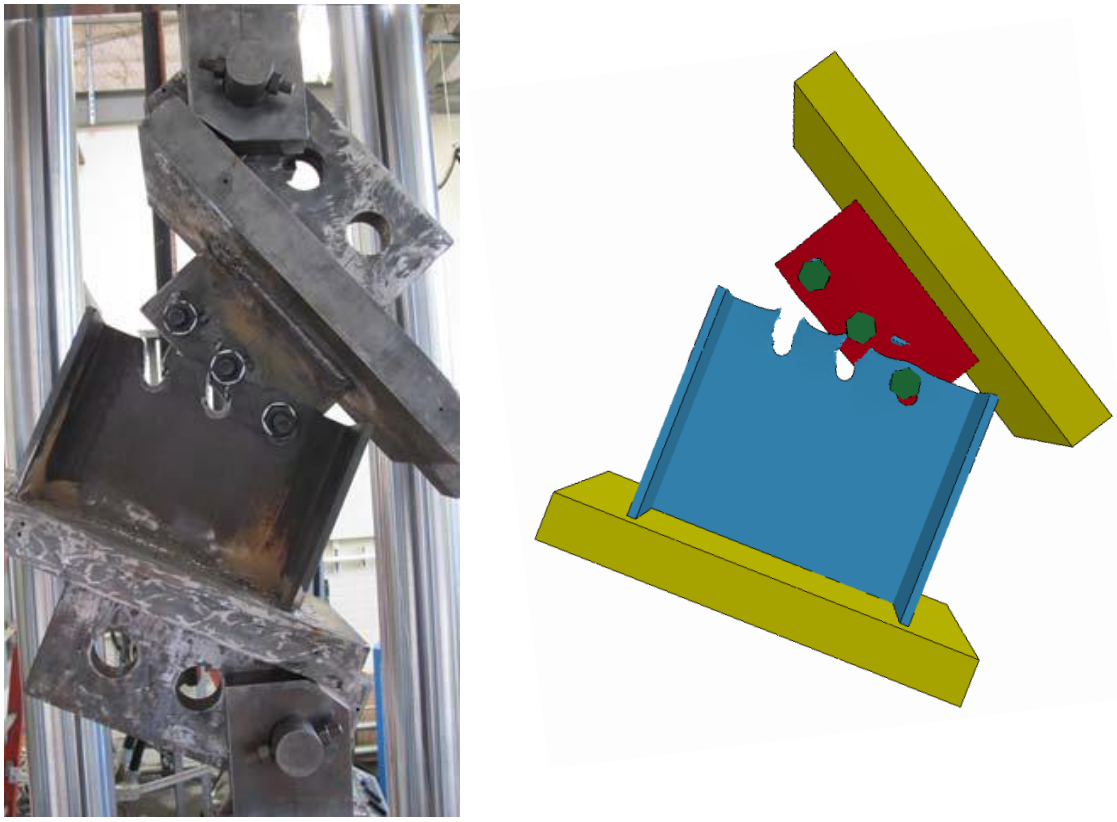

(a) (b)

Figure 4.23: Comparison of connection failures for inclined tension: (a) Test, (b) LS-DYNA

4.2.3 Concrete Slab

Aside from the steel member connections described in the preceding sections, another major component of a composite floor system is the concrete slab. Modeling of concrete is numerically challenging because of its different tensile and compressive strength values, the abrupt changes in stiffness when reaching these limit states, and the effects of triaxiality. Previous experimental studies on slab panels uniformly loaded until failure were used to ensure the modeling approach and material properties used to

represent concrete in the computational analyses were capable of predicting its response with reasonable accuracy. Of particular interest was verifying that the FE analyses were able to capture failure modes associated with the limit states of tensile cracking and compressive crushing. Such failure modes were observed during past experimental tests, as presented in the previous chapter, and it was desirable to explicitly capture these modes of response using computational simulations.

Park (1964b) performed tests on concrete slab panels with fully restrained edges. A series of reinforced and unreinforced slabs with plan dimensions 84 in. × 64 in. (2.10 m × 1.60 m) and different thicknesses were fastened to a relatively rigid test frame, shown in Figure 4.24, to provide full restraint against rotation and translation. After the slab panels were installed in the test frame, they had a clear span of 60 in. × 40 in. (1.50 m × 1.00 m). A uniformly distributed load was applied to the entire area of the slab using a rubber bladder filled with water. The specimen considered for validation purposes was a 2-in. (25.4-mm) thick unreinforced concrete slab denoted as "specimen D5" (Park 1964b). The compressive strength of concrete for this specimen was 4440 psi (30.6 MPa), and the slab sustained a maximum pressure of 3.84 psi (26.5 kN/m^2).

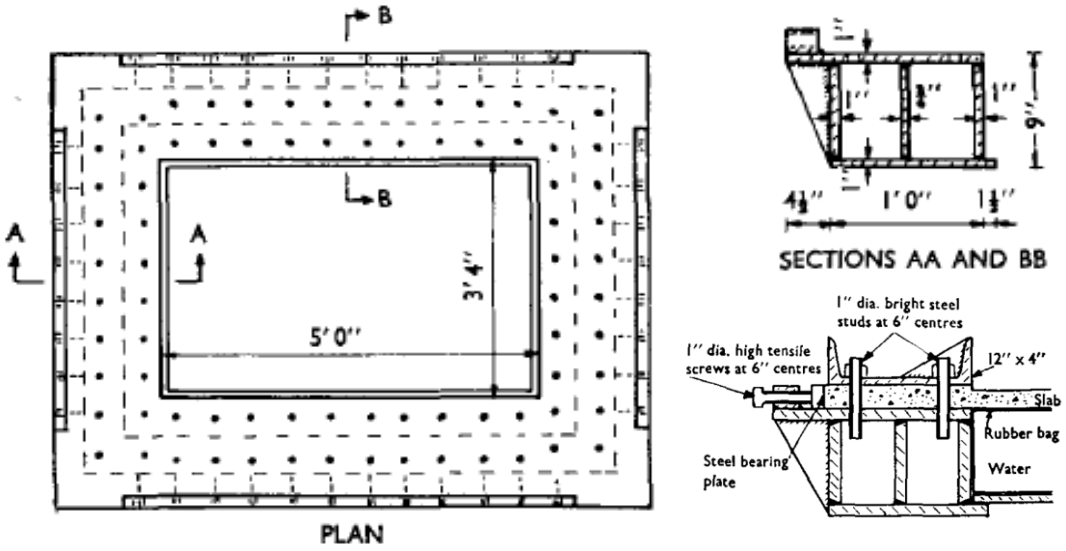

Figure 4.24: Test frame used by Park (1964b)

Specimen "D5" was modeled in LS-DYNA with eight-node hexahedral elements having one centrally located integration point (*SECTION_SOLID, elform = 1), as shown in Figure 4.25. Four elements were used through the thickness of the slab as shown in Figure 4.26, giving an element edge length of 6.35 mm. The length of the elements in the other two directions was 12.7-mm long. The concrete was modeled using the Continuous Surface Cap Model (*MAT_CSCM_CONCRETE) (Murray 2007). The automatic parameter generation option was employed so that the default input parameters were generated based on its unconfined compressive strength. To explicitly capture the effects of concrete cracking, the integrated erosion criterion of the material model was enabled (erosion = 1).

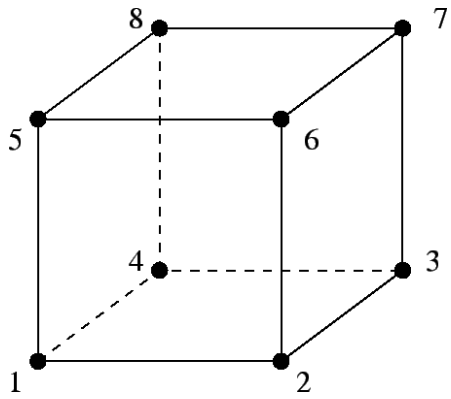

Figure 4.25: Eight-node hexahedral element

The effects of the boundary conditions provided by the test frame were explicitly modeled with a 300-mm wide zone of shell elements with five integration points through their thickness (*SECTION_SHELL, elform = 2, nip = 1) along the perimeter of the model, as shown in Figure 4.26. The thickness of the shell elements was such that they had the same in-plane moment of inertia as that provided by the experimental test frame. Specifically, the concrete slab rested on a relatively stiff steel perimeter frame (Figure 4.24), which was represented with 5.3-in. (132-mm) thick shell elements. At the top, the slab was clamped with a 12 in. × 4 in. (300 mm × 100 mm) U-channel section that was represented with 1.4-in. (36-mm) thick shell elements as shown in Figure 4.26. To simulate the uniformly distributed load that was applied in the actual tests, nodal loads were applied to the exterior face of the slab (*LOAD_NODE_SET).

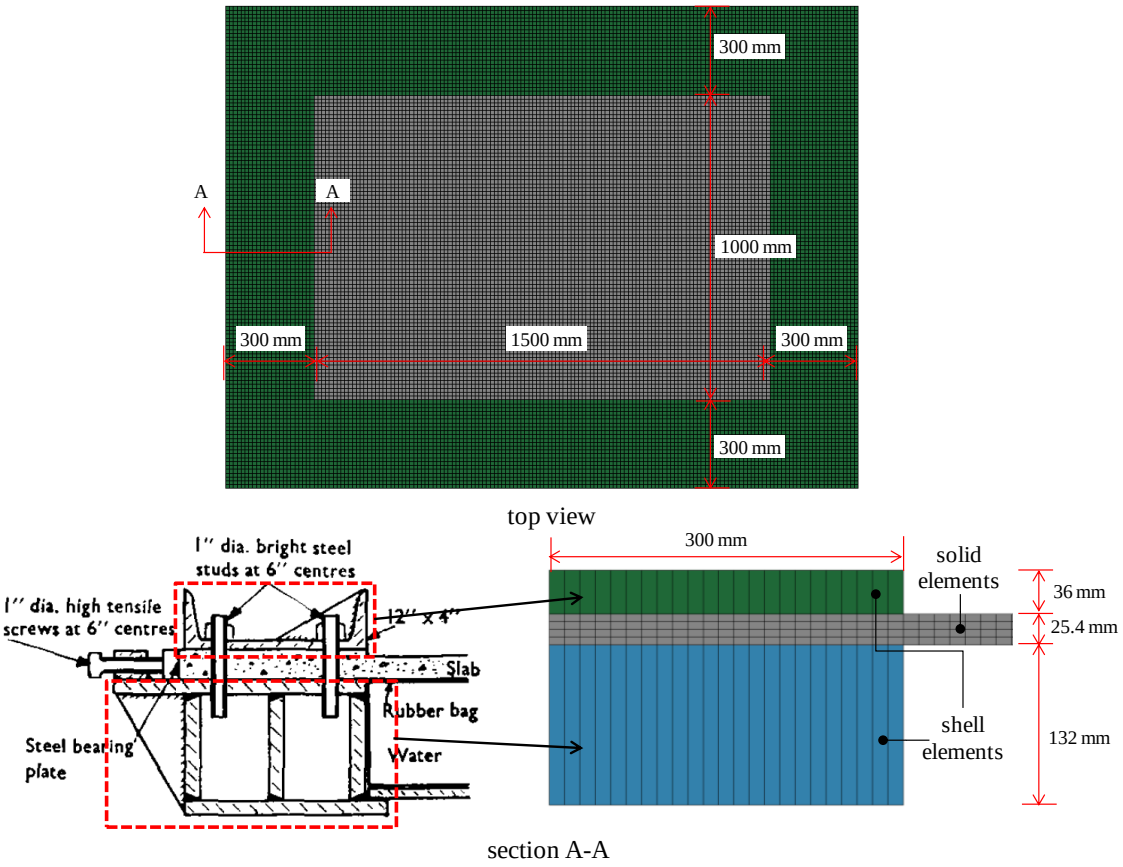

Figure 4.26: FE model of "specimen D5", (Park 1964b) (actual shell element thickness is shown)

The uniform load versus vertical displacement at the center of the slab curve is shown in Figure 4.27. The experimentally obtained response is in good agreement with the FE analysis. The initial stiffness of the slab is predicted with good accuracy, and, at higher loads when cracking first occurs at the top fibers of the slab, the stiffness gradually drops. The test specimen sustained an ultimate uniform load of 3.84 psi (26.5 kN/m^2), whereas the analysis in LS-DYNA predicted an ultimate load of 4.31 psi (29.7 kN/m^2). The predicted load is less than 15% higher, and the discrepancy can be attributed to

material variability and the slightly different loading conditions. Overall, there is good agreement between the measured and predicted behavior.

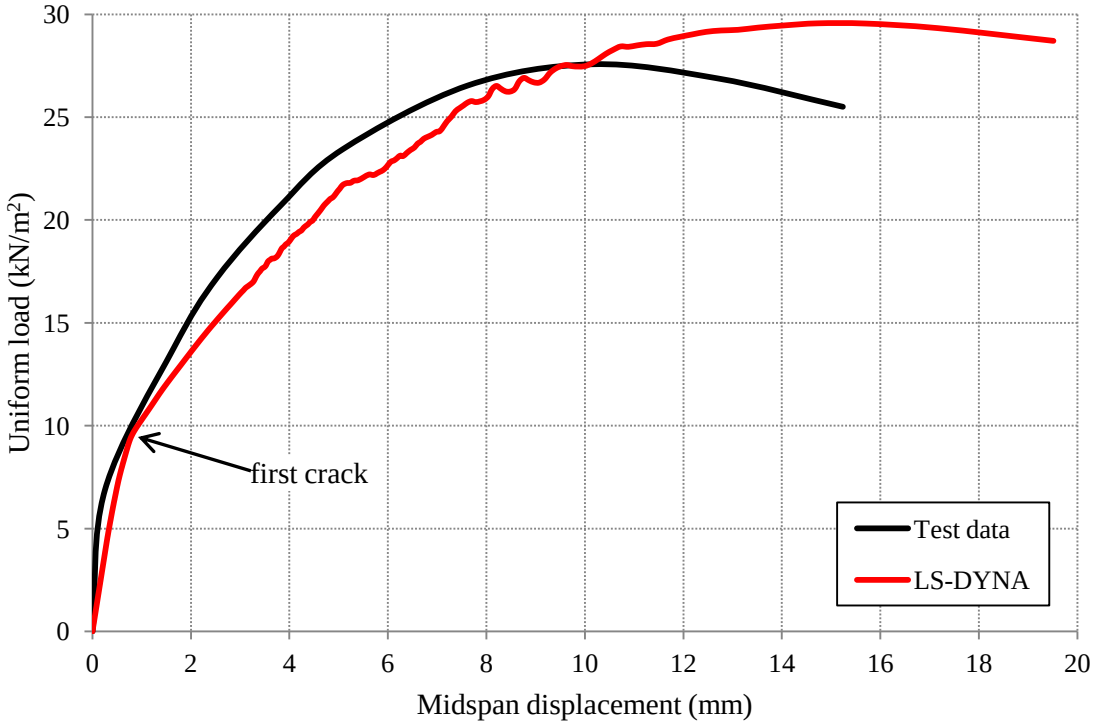

Figure 4.27: Load-displacement comparison between LS-DYNA and test for an unreinforced concrete slab with edges restrained, "specimen D5", (Park 1964b)

Additional analyses were performed with the same model by altering the boundary conditions. A first analysis was performed with shell elements having thicknesses reduced to 25% of those shown in Figure 4.26. Thus, the shell elements at the top had a 9-mm thickness, and those at the bottom had a 33-mm thickness. The slab sustained a maximum load of 3.92 psi (27 kN/m^2) compared to 4.31 psi (29.7 kN/m^2) when the shell thicknesses were representative of the actual boundary conditions

provided by the test frame (Figure 4.24). Two more analyses were performed by removing the shell elements from the model. In the first case, all the nodes along the perimeter 12-in. (300-mm) width zone were restrained against all translational and rotational degrees of freedom, and the slab failed at a load of 5.37 psi (37 kN/m^2). A second analysis was performed by allowing the slab to expand laterally (i.e., in-plane displacements were permitted), and the slab sustained a maximum load of 2.03 psi (14 kN/m^2). The results from these analyses are summarized in Figure 4.28. The considerable variation in the ultimate load the slab panels could sustain depended significantly on the amount of lateral restraint provided. These results highlight the importance of accurately modeling boundary conditions in such analyses. This observation was taken into consideration in the subsequent analyses of the specimens tested for the current research project. Because the floor systems tested in the current program were loaded in a similar restraining frame (Figure 3.3) as the one used by Park (1964b) (Figure 4.24), it was deemed necessary to explicitly model this test frame to account for its contributions to the response of the specimens.

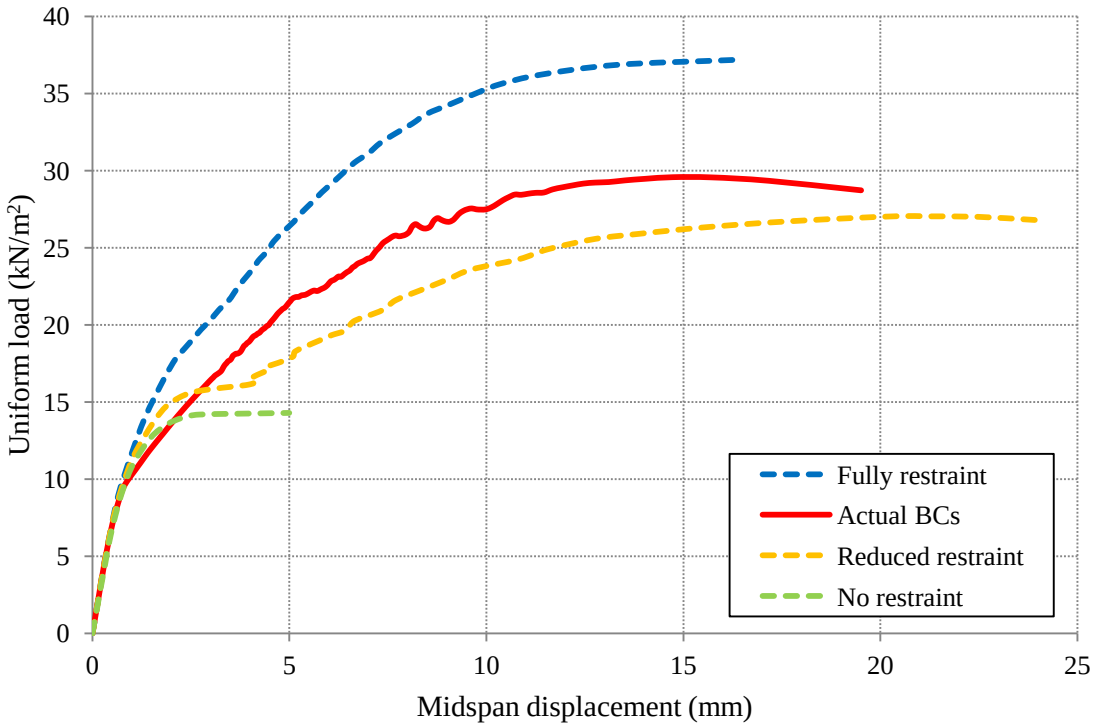

Figure 4.28: Comparison of the load-displacement response for concrete slab panels with different boundary conditions

4.2.4 Overview

Data from experiments on individual components was used to validate modeling techniques that were subsequently used to simulate the response of the specimens tested during the current study. The components selected were similar to the main components of the floor systems studied during the current project. Detailed numerical models were developed, and their response was compared with experimental data reported in the literature. Overall, good correlation between the computed and measured behavior was found, and the detailed numerical models were capable of explicitly capturing failure modes such as steel fracture and concrete cracking. Similar modeling procedures were

followed to simulate the response of the two specimens tested during the current project and are presented in detail in the following section.

4.3 TEST SPECIMEN MODELING

Detailed three-dimensional models of the specimens' geometry were created using CAD drawing software. These highly detailed models were then used to generate the FE mesh, accounting for all components of the floor system and reaction structure. With this approach, modeling assumptions were minimized, and the various failure modes observed during the tests were captured including bolt fracture, concrete cracking, and failure of the corrugated decking. Four-node tetrahedral elements (Figure 4.3) were used to represent all steel components, including the beams, bolts, shear tabs, and angles. The concrete slab was modeled with eight-node hexahedral elements (Figure 4.25). Shell elements with four nodes were used to represent the corrugated metal decking, and two-node beam elements were used to represent the reinforcing steel and shear connectors. Taking advantage of symmetry, one-quarter of the ICL specimen and one-half of the ECL specimen were modeled as shown in Figure 4.29.

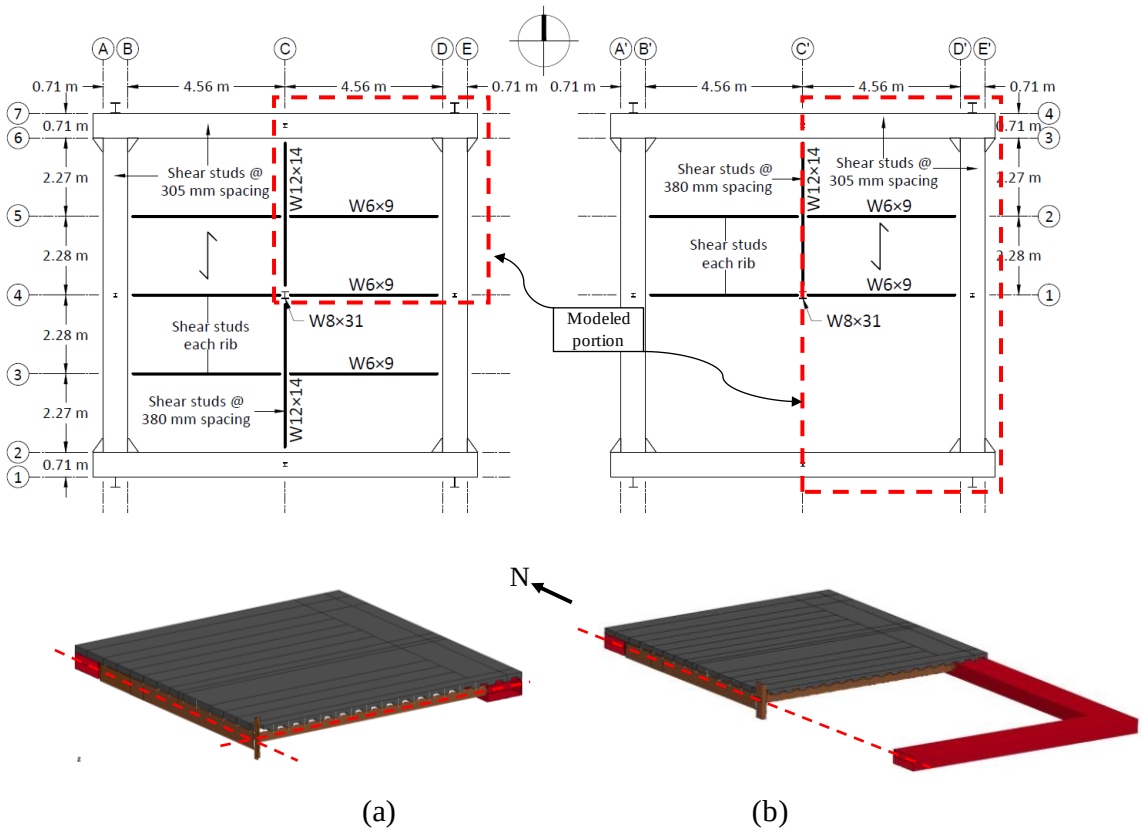

Figure 4.29: FE models of the test specimens: (a) ICL specimen (quarter model), (b) ECL specimen (half model)

4.3.1 Component Modeling Details

Specific details for the numerical modeling of each component comprising the entire model are presented in this section. In Figure 4.30, the components that were included in the computational model are shown. These components include the concrete slab, the steel deck, the steel beams, connection parts (i.e., bolts, angles, and shear tabs), and the shear studs. The interaction among these components was captured by defining a penalty-based contact as appropriate (with additional details provided below). The tek-

screws used to fasten the steel deck to the steel grillage and to attach adjacent deck panels together were included in the model as non-linear springs (not shown in Figure 4.30).

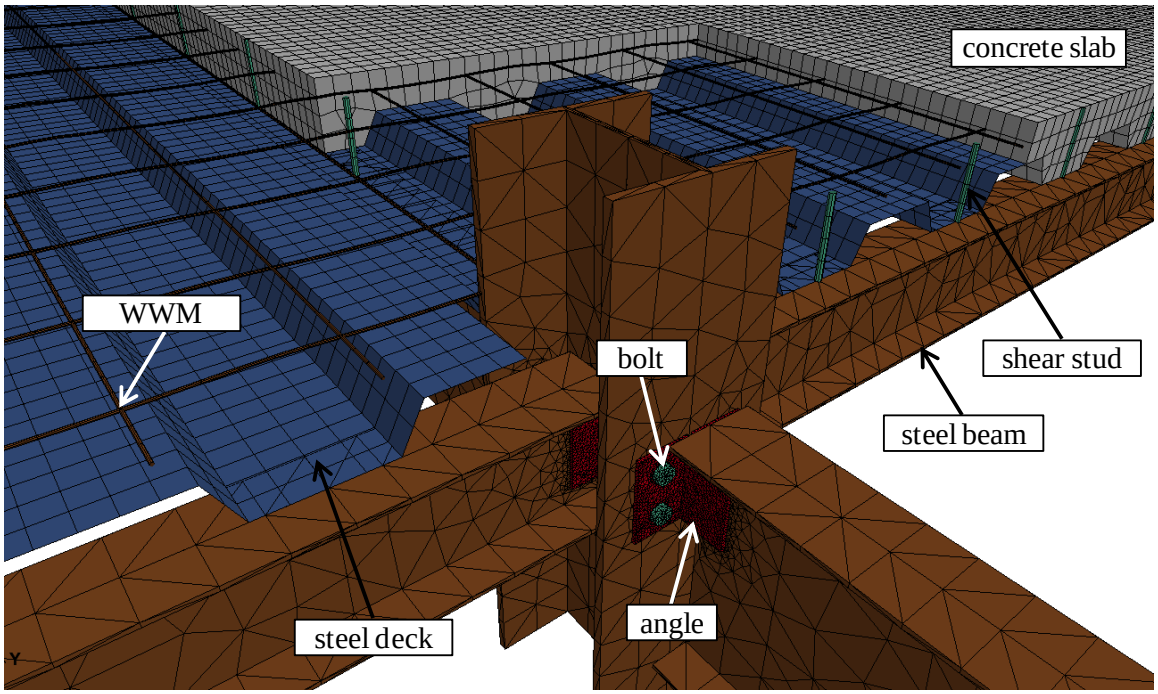

Figure 4.30: Details of the FE model (some parts are omitted for clarity)

4.3.1.1 Concrete Slab

The following list summarizes the modeling techniques used to represent the concrete slab:

- Concrete: Eight-node hexahedral elements (Figure 4.25) with one centrally located integration point (*SECTION_SOLID, elform = 1), were used to model the concrete. The average edge size was 28-mm long. Four elements were placed through the

thickness of the slab along the low-flutes of the corrugated deck, and two elements were used along the high-flutes as shown in Figure 4.30.

- Corrugated steel decking: Deck panels with dimensions of 0.91-mm wide and 5.20-m long were used to cover the steel grillage in the experimental tests (Figure 3.11). The decking was modeled with rectangular four-node shell elements with four integration points through the thickness (*SECTION_SHELL, elform = 2, nip = 4). Although the adjacent panels had an overlapping width of 60 mm on all four sides, this was not included in the computational simulations because the strength of the deck splices is mainly attributed to the strength of the tek-screws used to fasten the deck in place before casting the concrete slab. Figure 4.31 shows a perspective view of a bay of the FE model with the modeling details depicted. The decking was assumed to be fully bonded to the concrete slab. For that reason, the shell elements of the decking shared the same nodes as those of the solid elements along the bottom face of the concrete slab as shown in Figure 4.30.

- Deck splices and fastening: Between adjacent deck panels, #10 tek-screws were placed every 750 mm to connect them together (Figure 3.11). Tek-screws were also used to fasten the deck panels on top flanges of the steel grillage (Figure 3.11). These screws did not have any structural function, but they were placed to ease constructibility. Nonetheless, they were included in the simulations as discrete non-linear springs (*SECTION_BEAM, elform = 6) and are depicted in Figure 4.31.

- Slab Reinforcement: The entire slab was lightly reinforced with Welded Wire Mesh (WWM) with dimensions 150 mm × 150 mm × 3.125 mm (Figure 3.11). A clear

cover of 25 mm was maintained for the WWM. Additional reinforcing bars were placed at regions of the slab that develop negative moments under normal loading conditions (i.e., no column removal). These additional bars were used to control cracking under service loads. In both specimens, the bars were 1.20-m long, spaced every 0.30 m. 9.5-mm reinforcing bars were used in the ICL specimen and 12.7-mm were used in the ECL specimen (Figure 3.11). The reinforcing bars in the ICL specimen had a clear cover of 15.5 mm, and the bars in the ECL specimen had a clear cover of 12.3 mm. These components are depicted in Figure 4.31 and were modeled with two-node beam elements (*SECTION_BEAM, elform = 1, cst = 1). The interaction of the reinforcing steel and the concrete slab was included by merging the nodes of the beam elements with the nodes of the solid elements representing the concrete slab. Because the beam elements shared the same nodes as the solid elements, the exact clear cover the specimens had was not maintained due to the significant mesh refinement that the solid elements would require. Both types of reinforcement were placed at the same level of 28.6 mm from the top surface of the slab, corresponding to a clear cover of 27 mm for the WWM, 23.8 mm for the 9.5 mm bars, and 22.2 mm for the 12.7 mm bars. These values are only slightly different from those specified in the construction drawings. Due to variability in placing the bars and due to construction tolerances, the precision of the bar positioning in the FE models was considered to be reasonable.

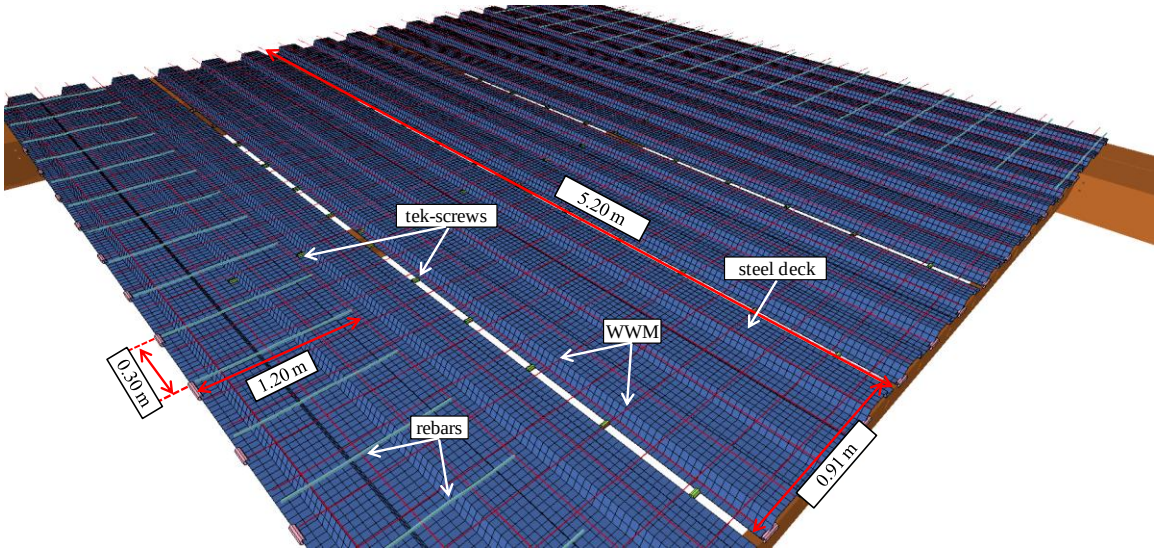

Figure 4.31: Perspective view of a typical bay of the FE model (some parts are omitted for clarity)

4.3.1.2 Steel Components

The following list summarizes the modeling techniques used to represent the steel components:

- Steel beams: The steel beams of the floor system and the perimeter beam (Figure 3.8) were modeled using four-node tetrahedral elements with one integration point (Figure 4.3) and an edge size of approximately 50 mm (*CONTROL_SOLID, elform = 10). Convergence studies demonstrated that this element size is able to capture the stiffness of these steel components with reasonable accuracy. Globally, the steel beams remained elastic, with none of them experiencing plastic deformations. Therefore, mesh refinement was not deemed necessary. Nonetheless, localized plastic deformations were observed around the bolt-holes. For that reason, the mesh size in the vicinity of the bolt holes was reduced to approximately 3 mm, which was found

from the computational validation described in Section 4.2.2 to be adequate for capturing localized plastic deformations with reasonable accuracy. A close view of the floor beam shear-tab connection is shown in Figure 4.32. With increasing deformations, as observed during the experimental tests, the web of the main girder (W12 × 14) started to bind against the perimeter beam, which resulted in localized buckling of the web and fracture between the bottom flange and the web. To capture this behavior, triangular shell elements with four integration points (*SECTION_SHELL, elform = 4, nip = 4) and a 10-mm long edge were used in that region of the girder. The use of solid elements in this region was not able to accurately capture this failure mode. Figure 4.33 shows a close-up view of the FE model depicting these details. Continuity of the main girder (W12×14) at the joint between the shell elements and solid elements was maintained by overlapping shell and solid elements and merging their coincident nodes over a 380-mm length. The overlapping was used to allow rotational compatibility between the two elements types due to the absence of rotational degrees of freedom at the solid elements. Therefore, the overlapping elements allowed for proper shear, flexural, and axial transfer of the forces over the entire length of the girder. Figure 4.34 represents the region of the main girder that includes the joint with the two element types.

The steel cantilever beam shown in Figure 4.35 demonstrates the validity of the method used to connect shell and solid elements for representing a continuous beam. The cantilever is 2-m long, 0.6-m wide, and 0.2-m deep, and a prescribed displacement of 0.3 m is applied at the beam edge. Under 0.3-m vertical displacement, the theoretically calculated reaction force is 9450 kN (Gere and

Goodno 2012). The first half of the beam was modeled with solid elements, and the second half used shell elements. In Figure 4.36(a), the solid and shell elements overlap over a 0.2-m length, and the coincident nodes are merged together. In Figure 4.36(b), however, there is no overlapping between the two elements types, and the coincident nodes at the edges of the two element types are merged together. The deformed shape of the two models is shown in the same figure. It is clear that the deflected shape in Figure 4.36(b) is incorrect, and no reaction was measured at the fixed end due to the absence of rotational degrees of freedom for the solid elements. This result occurs because it is not feasible to transition rotation through a single row of nodes, and the edge where the shells transition into solids acts like a hinge. Conversely, the deflected shape in Figure 4.36(a) is consistent with that expected for the theoretical solution, and the reaction at the fixed end is 9200 kN, which is approximately 2.6% lower than the theoretically calculated one (Gere and Goodno 2012). This modeling approach resolves the deficiency in the model previously described (Figure 4.36(b)) because it engages two rows of nodes at the interface of the two element types, which interact and allow the transition of rotation in a force-couple-like form. This same approach was used to model the transition from the shell to solid elements on the W12×14 section in the analyses presented.

- Connection components and bolts: To model the connections between the frame members, four-node tetrahedral elements were utilized for the angles, the shear tab plates, and the bolts. Figure 4.32 and Figure 4.37 show the FE model of these connections. The mesh size used had an edge length of approximately 3 mm, similar to the size used for the simulation of the shear tab test specimen of Guanyu (2011),

presented in Section 4.2.2, which was found to be adequate to capture both the stiffness and plastic deformation of these connection types (Figure 4.20, Figure 4.21). It is noted that the components comprising the connection were modeled as separate parts, and their response relied on the contact between their surfaces.

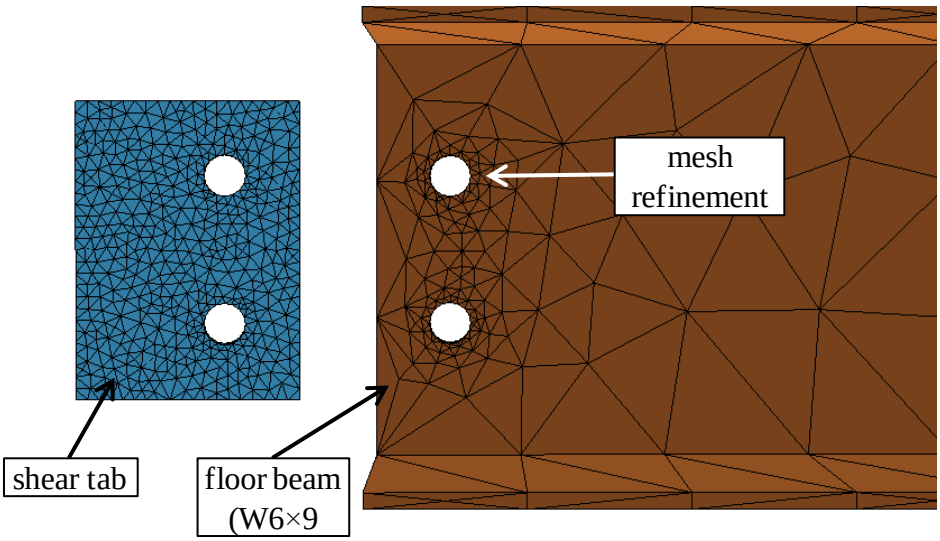

Figure 4.32: Detail of shear tab connection (bolts are omitted for clarity)

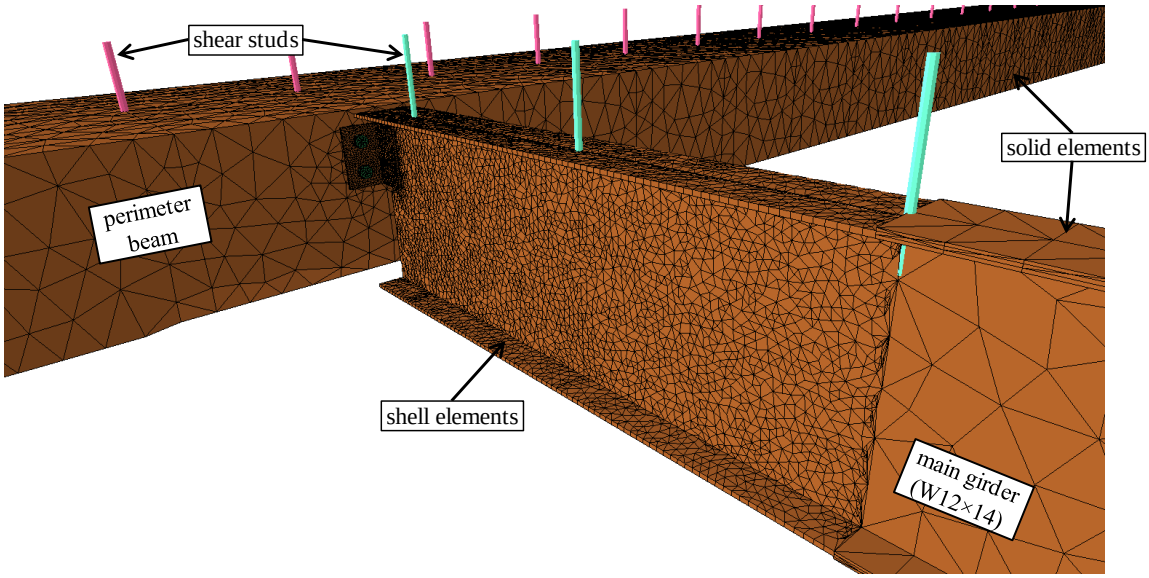

Figure 4.33: Detail of main girder mesh refinement with shell elements

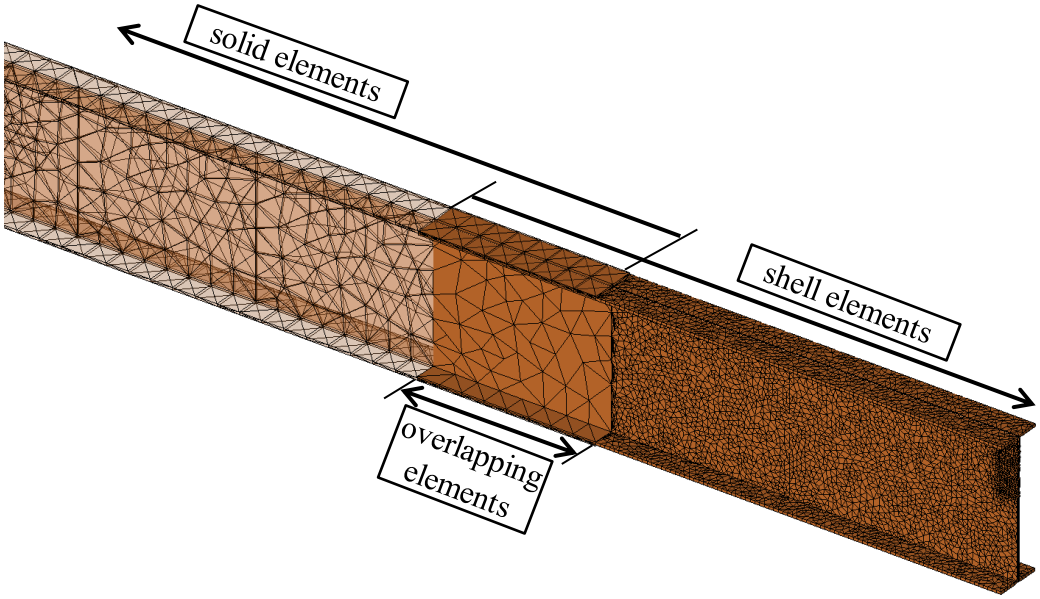

Figure 4.34: Joint of solid and shell elements close to the main girder (W12×14) end

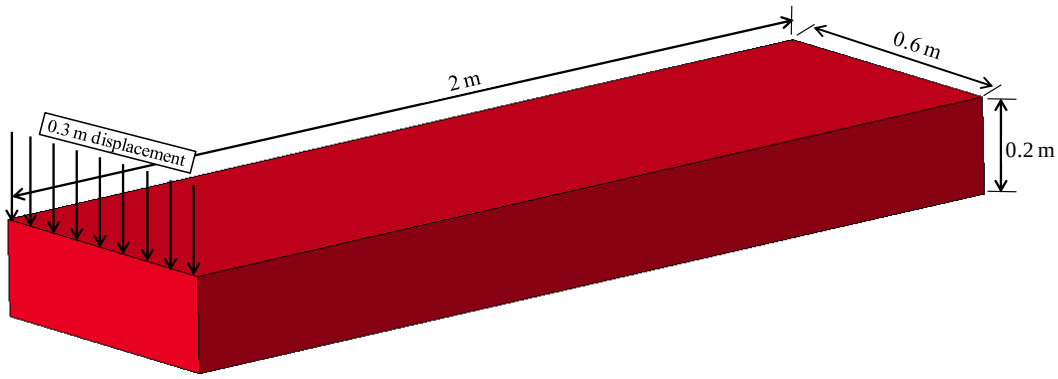

Figure 4.35: Cantilever beam geometry

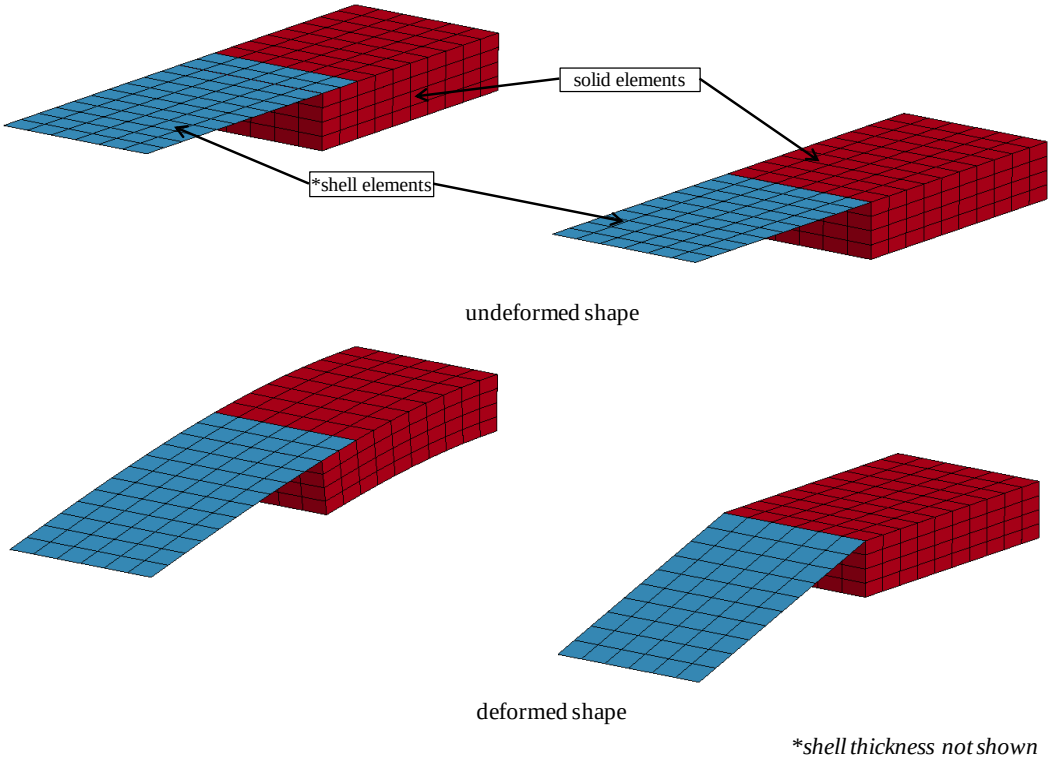

Figure 4.36: Cantilever beam modeled with solid and shell elements: (a) Overlapping elements, (b) No overlapping elements

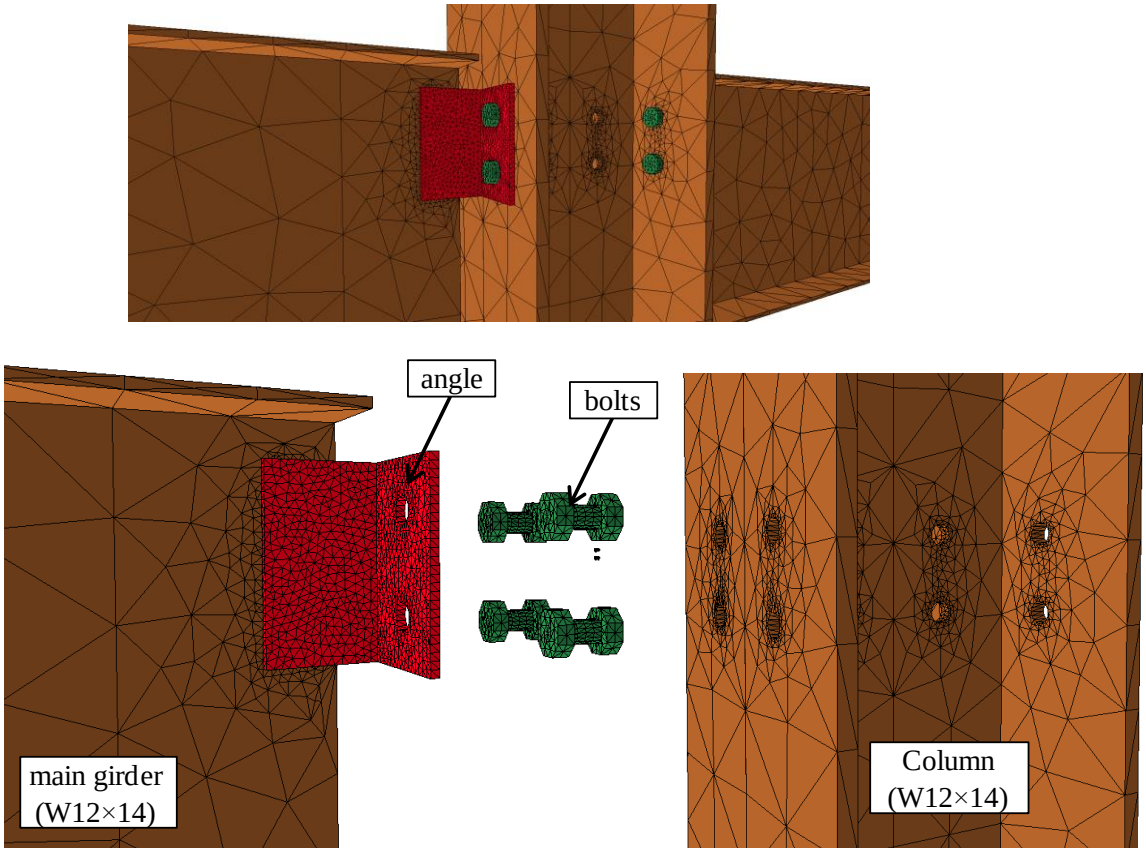

Figure 4.37: Detail of double angle connection

- Shear studs: The shear studs were modeled using two-node beam elements (*SECTION_BEAM, elform = 1, cst = 1). They were assumed to be fully bonded to the concrete and extended through the full slab thickness. Because the slab had four elements through its thickness, four beam elements were used for the studs as well. Thus, the shear stud nodes were coincident with those of the concrete slab. These nodes were merged to represent the mechanical interaction between each shear stud and the surrounding concrete. Because the shear studs were welded through the deck to the top flanges of the beams, inevitably, the decking was also attached to the beams

due to the fact that melted metal connected these parts together around the perimeter of each stud. For that reason, the node at the base of each stud was merged with a node of the deck and one from the top flange of the beam as shown in Figure 4.30. Because the solid elements used to represent the beams did not have rotational degrees of freedom, a fifth beam element was added at the base of each stud towards the beam web, and its node was merged together with the coincident node of the beam web as depicted in Figure 4.38. This additional element "fixed" the shear stud to the beam top flange, preventing it from rotating freely. More accurate modeling of the connection between the stud and beams was not deemed necessary because observations after the test revealed that the studs remained attached to the beams, even after the specimens totally collapsed.

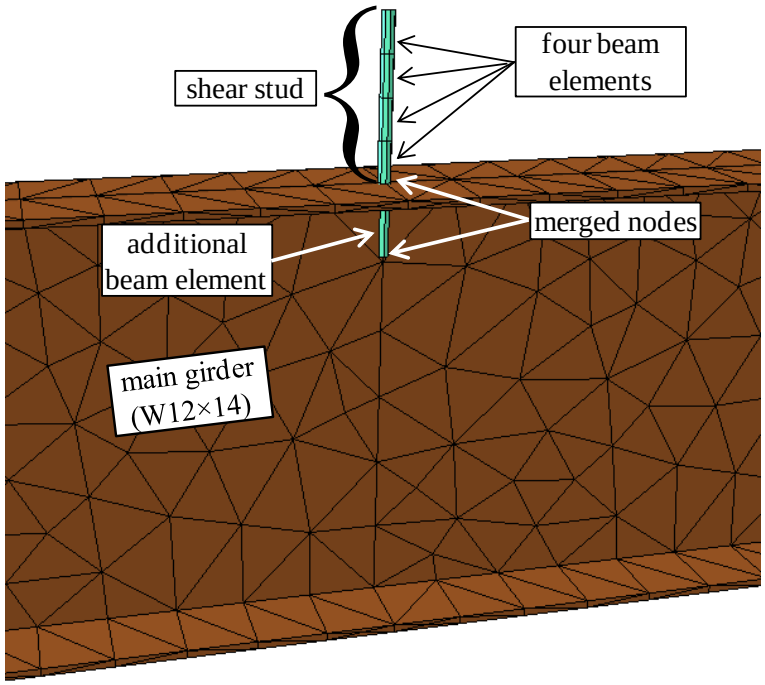

Figure 4.38: Detail of the shear stud attachment to the beam top flange

4.3.1.3 Contact Definitions

A penalty-based contact procedure was used to capture the interaction among the various parts of the FE models. The Automatic Single Surface Contact (*CONTACT_AUTOMATIC_SINGLE_SURFACE) algorithm was enabled in LS-DYNA. This is a penalty-based contact algorithm that places springs at the normals of all penetrating nodes and the contact surface. Penetrations are limited by applying penalty forces at penetrating nodes. Iterations are made until penetration is limited within a specified tolerance and the applied forces, commonly known as contact forces, are equal and opposite in direction between the contacting parts. This contact definition automatically searches for potential contact between different parts of the model without the need to define certain contact pairs. The "slave search" is used to locate the nearest point on the master surface of a slave node. Contact pairs between the slave nodes and the master surface are defined. More information about this method can be found in LS-DYNA theory manual (2015). For computational efficiency, parts that were known *a priori* to not require a contact definition were excluded from the contact algorithm. These parts included the shear studs, the tek-screws, the slab reinforcement, and the concrete. Relative movement for these parts was prevented by the modeling approach used in which the nodes for these components were directly merged and behaved as fully bonded. It is noted that because the concrete was on top of the corrugated steel decking, the interaction of the concrete slab with the steel grillage was still captured because the corrugated steel decking was included in the contact definition. The static coefficient of friction was assumed to be 0.5 (AISC 2014), and the dynamic coefficient of friction was set equal to 0.35 (though sliding friction was not expected to occur in the simulations).

4.3.2 Material Modeling

The concrete and steel components used in the specimens were tested according to ASTM standards to obtain their material properties. These measured properties were used to define the constitutive parameters in the computational simulations.

4.3.2.1 Concrete

The unconfined compressive strength of concrete was obtained from 100-mm diameter cylinders. These cylinders were tested according to ASTM standards (2014) on the same day the floor systems were tested. As reported in the previous chapter (Table 3.2, Chapter 3), the average compressive concrete strength for the ICL specimen was 40 MPa, and it was 46 MPa for the ECL specimen. Although the ICL specimen was tested over multiple days because of difficulties faced with the loading system, the compressive strength used for the computational analyses was kept constant with a value corresponding to the first test day. At that time, the concrete was 29-days old, and its compressive strength did not significantly increase over the two-month testing period of this specimen. The mass-density of the concrete used was found to be 24 kN/m^3.

The Continuous Surface Cap Model (*MAT_CSCM_CONCRETE) (Murray 2007) was used to model the concrete behavior. The automatic parameter generation option was employed so that default input parameters were generated based on the compressive strength obtained from the cylinder tests. The embedded element erosion criterion was enabled (erode = 1) to explicitly capture concrete cracking and to prevent computational difficulties associated with the highly distorted elements (Murray 2007) that were expected to exist in the simulations during collapsing of the models. This

material model was found to adequately represent the concrete behavior, as demonstrated in Section 4.2.3.

4.3.2.2 Steel Members

The Piecewise Linear Plasticity Model (*MAT_PIECEWISE_LINEAR_PLASTICITY) was used to model all the steel components. The element erosion criterion based on the maximum plastic strain at fracture was enabled to explicitly capture steel fracture.

Steel coupons were obtained from all the different parts of the specimens, including the wide flange steel members, shear tabs, angle sections, and steel decking. Tension test specimens were fabricated and tested according to ASTM standards, (ASTM 2012, ASTM 2008). More specifically, standard-size coupon specimens with a 50-mm gauge length (Figure 4.12) were fabricated from steel decking and from the web and flanges of the W12×14 and W6×9 wide flange sections. Sub-size specimens with a 25-mm gauge length, shown in Figure 4.39, were tested in tension for the shear tabs and the angle sections. The sub-size specimens were used for these components because the dimensions of the available steel pieces were not large enough to fabricate standard-size specimens. The engineering stress-strain curves from the tension tests were used to define the input material properties of the computational models. A procedure similar to the one presented in Section 4.2.2 was followed to obtain a set of true stress-stain values for each one of the steel components. Figure 4.40 and Figure 4.41 show the set of true stress-strain values for each one of the steel components used in the computational simulations. The values for the erosion criterion were based on the actual fracture strains. These values

correspond to the last data point in each one of the stress-strain curves shown in Figure 4.40 and Figure 4.41. The modulus of elasticity was set equal to 210 GPa, the mass-density was specified to be 78 kN/m^3, and Poison's ratio was set equal to 0.29. These parameters are similar to those widely used in structural engineering according to the AISC Steel Construction Manual (2014) and Eurocode 3 (ECS 2005).

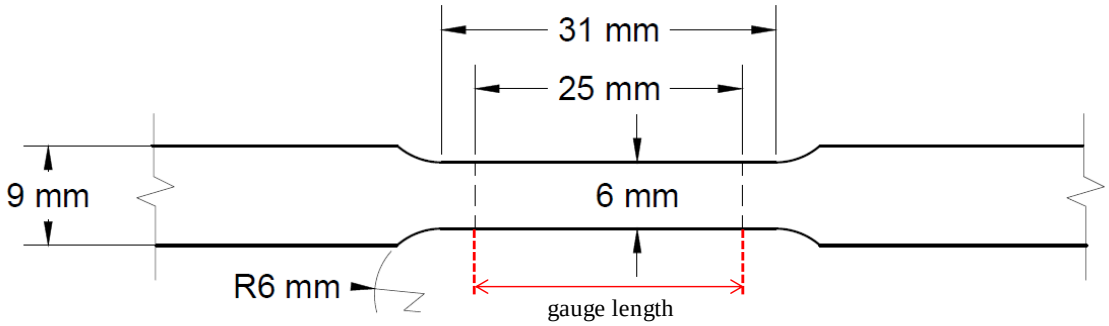

Figure 4.39: Sub-size coupon specimen (ASTM 2012)

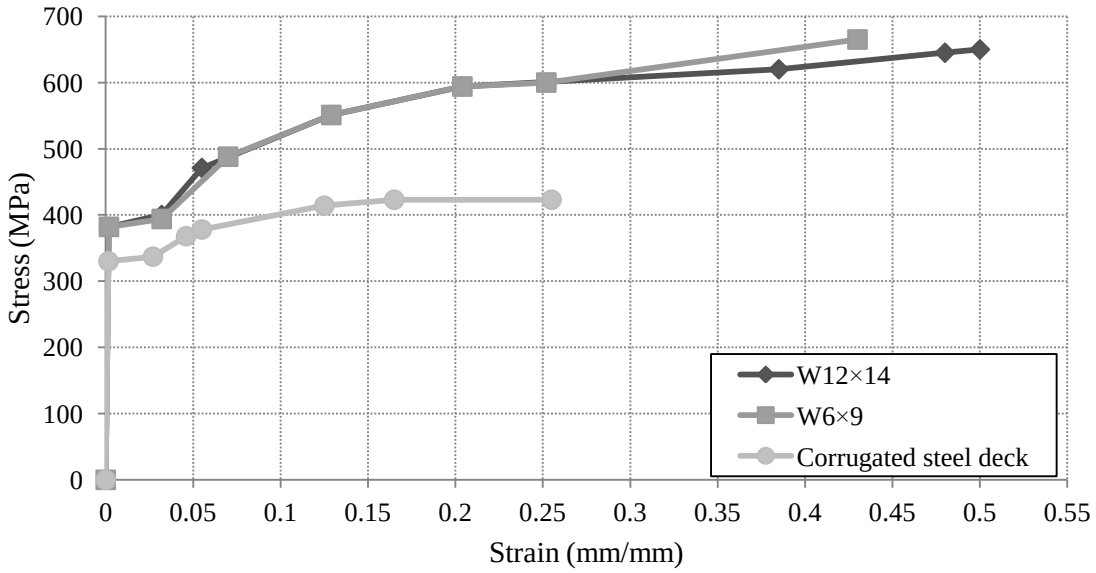

Figure 4.40: True stress-strain curves of steel components based on tensile tests with standard size coupons

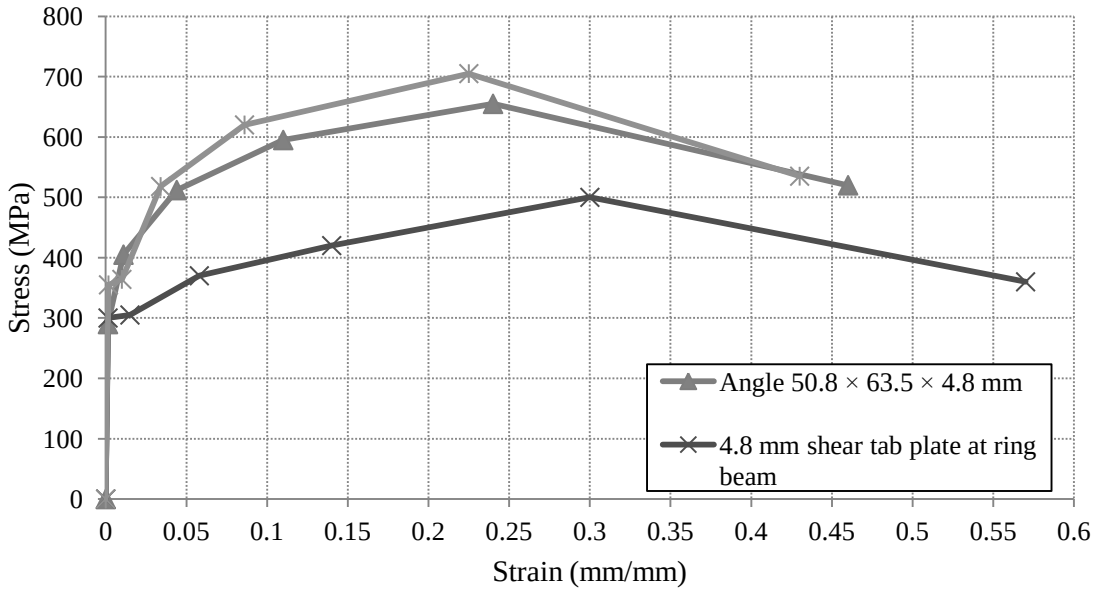

Figure 4.41: True stress-strain curves of steel components based on tensile tests with sub-size coupons

Tension tests were also performed on the 3.125-mm diameter WWM and the reinforcing bars used in the specimens. For the ICL specimen, 9.5-mm diameter reinforcing bars were used in certain regions, shown in Figure 3.11, and 12.7-mm diameter reinforcing bars were used for the ECL specimen. A total of nine tensions tests were performed, three for each reinforcement type. Figure 4.42 shows the set of stress-strain values for each of these components, which were obtained using a similar procedure to the one presented in Section 4.2.2. The only difference is that two-node beam elements were used for the material calibration because such elements were subsequently used to represent these components in the finite element models.

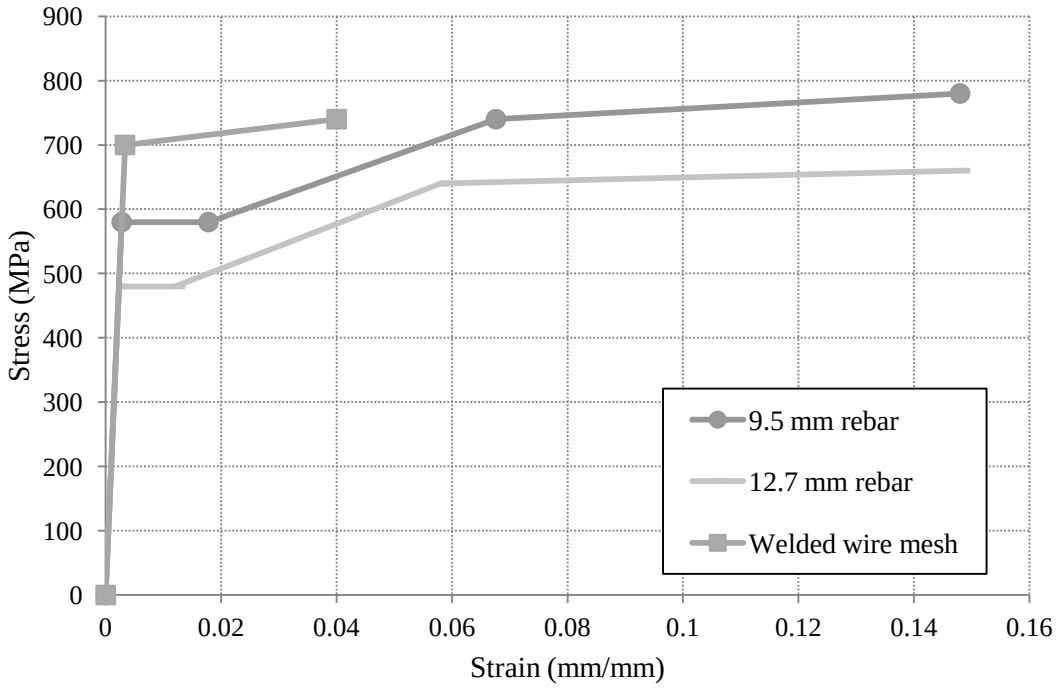

Figure 4.42: Stress-strain curves of the steel reinforcement

Nominal material properties were used for the shear studs as reported on the manufacture's catalogue (Nelson 2010). The nominal values for the studs used in the specimens were 340 MPa for the yield stress, 420 MPa for the ultimate stress, and 15% for the strain at fracture. As observed from the experimental tests, the shear studs were not severely loaded; therefore, a more accurate representation of their material properties based on test coupons was not deemed necessary.

4.3.2.3 Bolts

All bolts used for both specimens were 12.7-mm in diameter. During the tests, the bolts were primarily loaded in tension. Thus, tension tests on these bolts were performed using the setup shown in Figure 4.43. The obtained load versus displacement curve from the bolt tension tests was used to guide the selection of material parameters used in the constitutive model for the bolts. A bolt with nominal specified dimensions equal to the one used in the specimens was modeled and loaded in tension in LS-DYNA, as shown in Figure 4.44. The threads of the bolt were not included in the model, and the bolt-shaft was modeled as a cylinder. A number of other important details that influence the computed response were included. The diameter of the modeled bolt was based on the net area of a 12.7-mm diameter bolt that was found according to Kulak, *et al.* (2001). The diameter corresponding to its net area was 10.95-mm (Figure 4.44). The gauge length of the bolt (i.e., the length between the bolt head and the nut) was nearly identical to the one used in the tension tests of the bolts. It is noted that the bolt gauge lengths varied for different locations within the steel grillage because they were used to connect components of different thicknesses. A length of 21-mm (Figure 4.44) was representative

of the majority of the connections and was selected for the analyses. Figure 4.47(a) shows the experimentally obtained load-deformation curve for the bolt tested in tension.

Figure 4.43: Testing device for bolt tensile strength

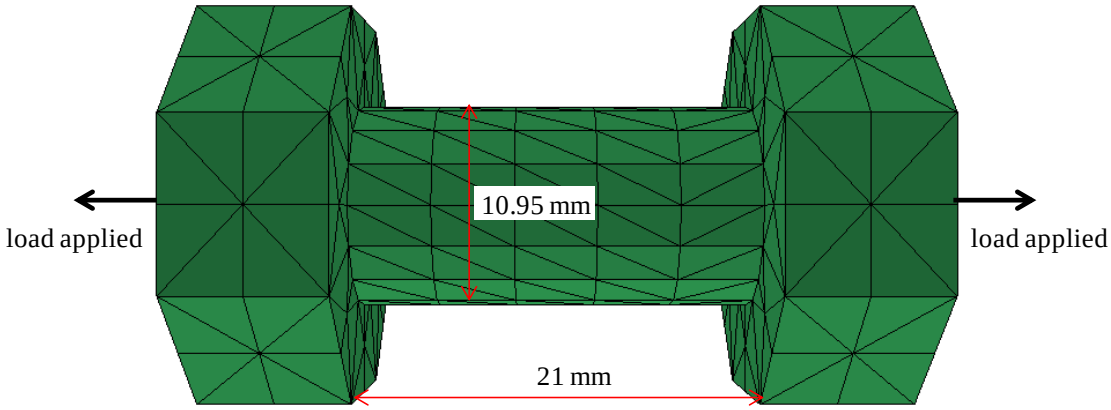

Figure 4.44: FE model of bolt

The Piecewise Linear Plasticity Model (*MAT_PIECEWISE_LINEAR_PLASTICITY) was used to model all the bolts. The curve shown in Figure 4.45(a) is representative of one of the tension tests that was performed on a number of bolts with nearly identical response. Based on the experimental response of a bolt in tension, shown in Figure 4.45(a), a set of stress-strain values used as input parameters in LS-DYNA are shown in Figure 4.45(b). These values were such that when loading the bolt in a similar way as schematically shown in Figure 4.44, the response of the bolt closely approximated the experimental one shown in Figure 4.45(a). It is noted that the experimental data from the bolt tension tests result in an unrealistically low modulus of elasticity as compared to the typical elastic modulus of steel. This was speculated to occur because of elastic bending of the bearing plates used in the testing device (Figure 4.43). However, the elastic modulus specified in the material model used to represent steel in LS-DYNA was set equal to 210 GPa, which is a typical value for steel. For that reason, the load-elongation curves shown in Figure 4.45(a) differ significantly in the elastic region of response. The test data suggest that steel yields at an elongation of approximately 1 mm, whereas using the actual elastic modulus of steel, yielding occurs at approximately 0.15-mm of elongation. After yielding, however, the plastic deformation until fracture is similar and equal to approximately 2 mm. Bolt fracture was explicitly modeled by enabling the erosion criterion and defining an effective plastic strain at fracture equal to 0.135. Figure 4.46 shows a comparison of the bolt behavior between the experimental tests and the computational simulations. The erosion criterion based on plastic strain was enabled to explicitly model bolt fracture.

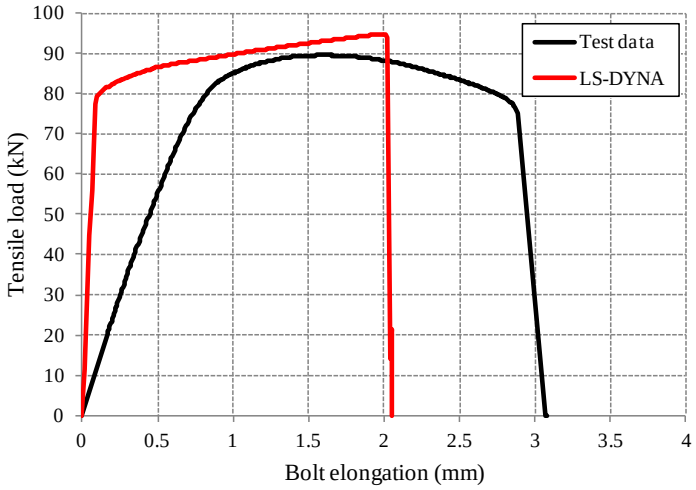

(a)

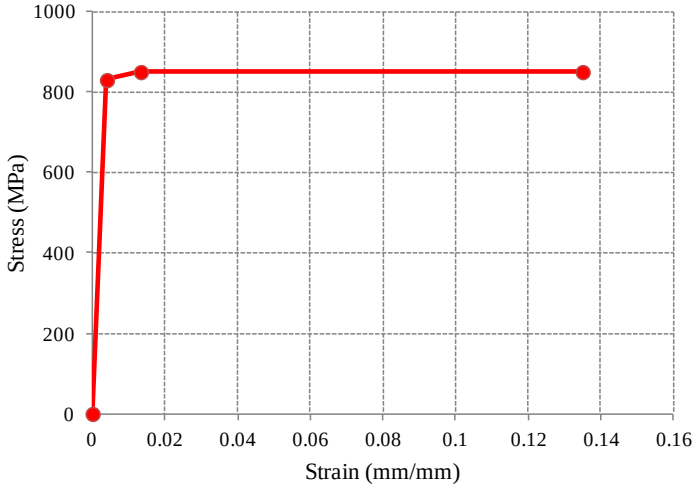

(b)

Figure 4.45: Bolt response in tension, (a) Experimentally and computationally obtained load-elongation curve, (b) Material input parameters

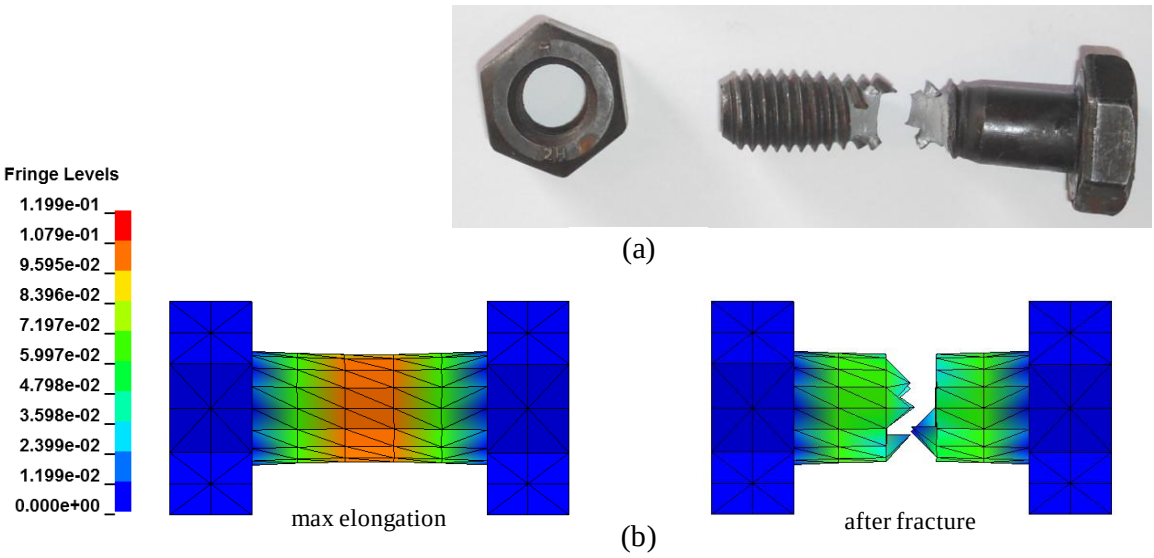

Figure 4.46: Bolt response, (a) Fractured bolt, (b) Plastic strains in the bolt before and after fracture

4.3.2.4 Tek-Screws

The tek-screws used to fasten the steel decking to the steel grillage and to connect adjacent deck panels together were also included in the computational models. Tension tests of such splices were performed in specimens shown in Figure 4.47. Because the response of the tension tests in these two different configurations was quite similar, a unified load-displacement response was used as a basis to generate input parameters for the non-linear springs used to represent their behavior. The General Nonlinear 6DOF Discrete Beam material model was used (*MAT_GENERAL_NONLINEAR_6DOF_DISCRETE_BEAM) to model the behavior of tek-screws. Figure 4.48 shows the experimentally obtained load versus elongation relationship from the tension tests and the set of input values for the non-linear spring.

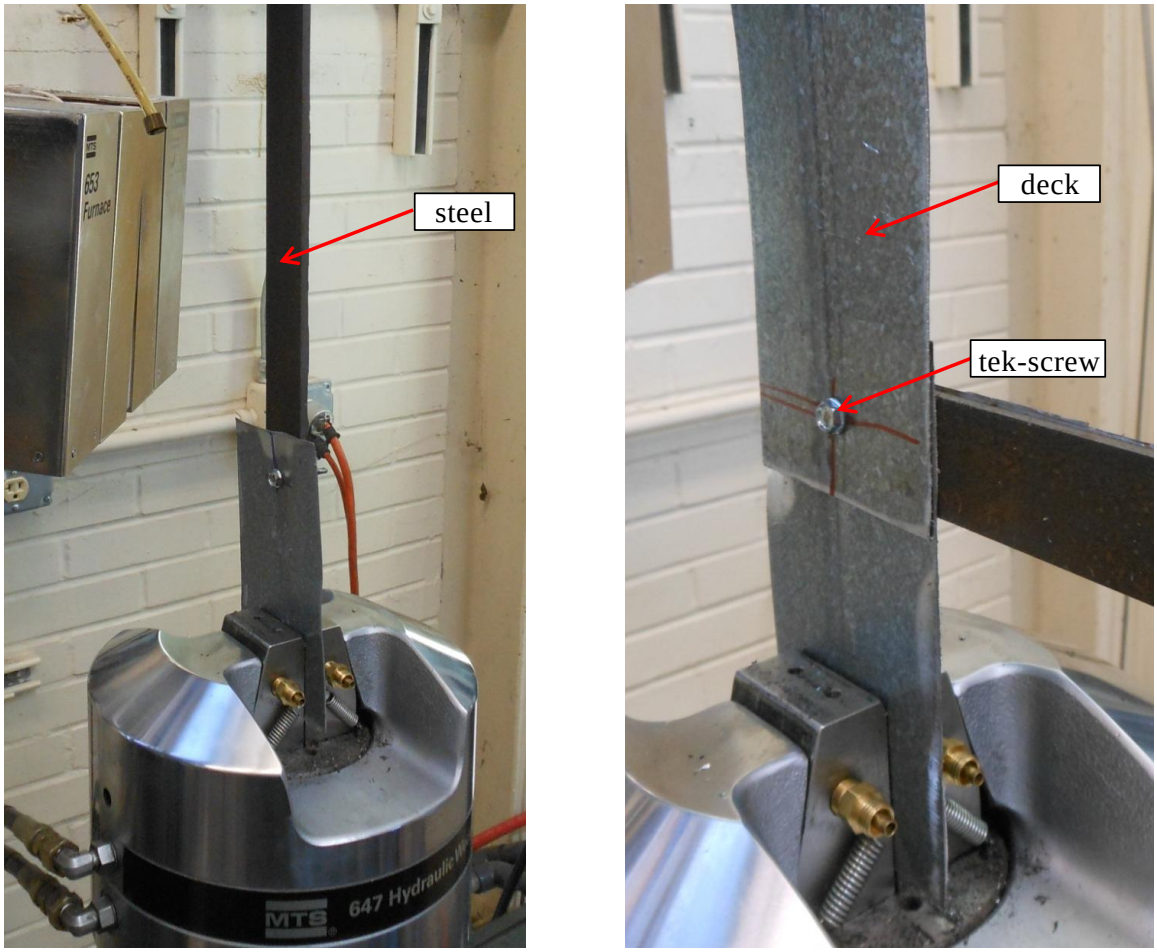

(a) (b)

Figure 4.47: Tension test specimens of tek-screws, (a) Deck-to-steel, (b) Deck-to-deck

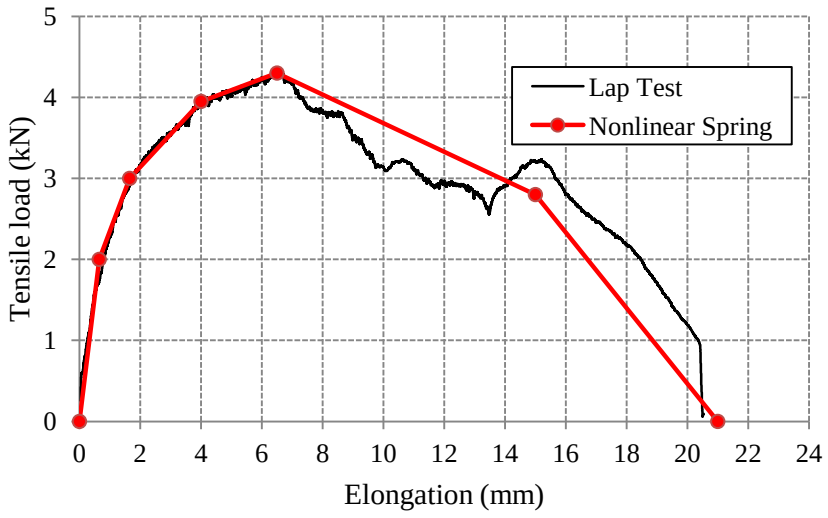

Figure 4.48: Load-elongation relationship of a tek-screw splicing two metal deck sheets

4.3.3 Solution and Loading Parameters

All analyses were conducted using the explicit solution scheme, which is suitable for highly non-linear simulations using LS-DYNA. The selective mass-scale option was enabled for computational efficiency (*CONTROL_TIMESTEP, dt2ms = < 0). Similarly to the experimental tests, the analyses were performed over long times to ensure quasi-static loading conditions. A loading rate of 5 kN/m^2/s was found to be adequate after performing a series of analyses using various loading rates and then comparing the load versus mid-span displacement curves. Load rates higher than 5 kN/m^2/s resulted in a "stiffer" response due to the significant contribution of inertial effect, whereas for lower loading rates, the response was practically identical.

The loads in the simulations were specified as nodal loads on the top surface of the concrete slab (*LOAD_NODE_SET). The procedure followed during the experimental tests was precisely simulated. Thus, the analyses were performed in three

stages, as in the actual tests, aiming to mimic the test procedure so as to allow direct comparisons between the computational results and measured data. At the end of each stage, the loads were held constant until the deformations stabilized. Even if load rates were low enough so that inertial effects were negligible, some kinetic energy was stored in the model due to its dynamic response. By keeping the load constant, this kinetic energy would drop to zero after the deformations stabilized (i.e., until the motion damped out).

For the first stage of analysis, the slab was loaded with a uniformly distributed load, equal to the initial load of the specimens prior to testing. A load equal to the reaction of the center column (column under removal) was applied simultaneously. At the end of this loading stage, the slab was loaded with the initial load applied to the specimen prior to column removal. During the second stage of analysis, column removal was simulated by allowing the reaction at this column to drop to zero while maintaining the initially applied nodal loads on the slab. At the end of this analysis stage, the reaction at the center column was zero, allowing the vertical deformations to start increasing. During the third and final analysis stage, the load on the entire area of the slab was increased until the specimen collapsed. Figure 4.49 provides a schematic representation of the three loading stages.

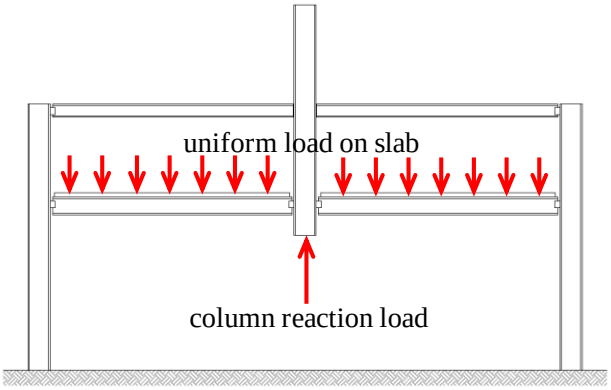

(a)

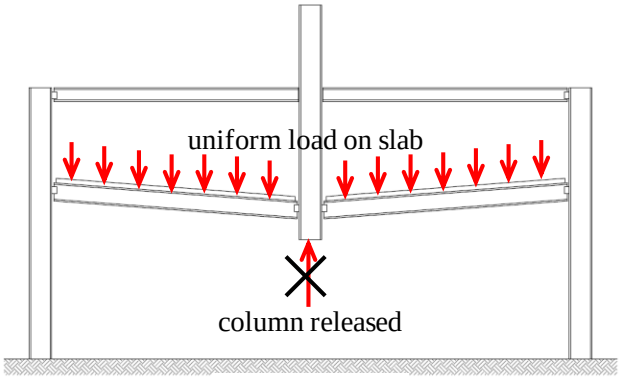

(b)

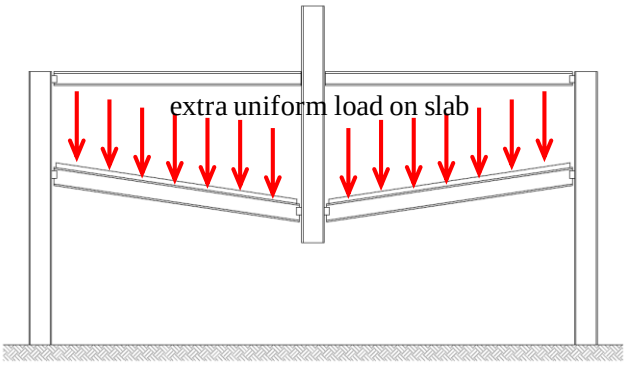

(c)

Figure 4.49: Load sequence of the computational models, (a) Stage 1: Initial slab load and corresponding column reaction. (b) Stage 2: Column reaction drops to zero, (c) Stage 3: Load on the slab increases until collapse

4.3.4 Simulation Results

This section presents a comparison between the response obtained from the computational analyses and those measured during the physical tests. All the deformations mentioned in this section refer to the vertical deflection at the location of the removed column.

4.3.4.1 ICL Specimen Response

The first test specimen, representing the loss of an interior column, had a total load of 5.75 kN/m^2 (120 psf) uniformly distributed over the entire area of the slab during the first stage of loading. Under this load, the interior column support was removed, resulting in a deflection of 52 mm. This value is marginally smaller than the predicted displacement of 55 mm obtained from the FE simulation. The complete column-reaction versus displacement curve is shown in Figure 4.50. Under the absence of the support at the interior column, the load on the floor slab increased to 8 kN/m^2 (167 psf), raising the vertical displacement to 110 mm. This value is slightly smaller than the predicted value of 114 mm obtained from the FE simulation**.** Figure 4.51 shows the complete superimposed load versus deformation curve. Overall, good agreement is observed between the experimental and computational results. The stiffening that is observed at a deformation of 110 mm is attributed to the development of in-plane membrane action within the floor slab. Because of the limited capacity of the loading system used in this specimen coupled with a floor slab capacity that was greater than anticipated, collapse did not occur under the largest load that could be applied. Nonetheless, through the FE simulation, the collapse load is predicted to be 10.90 kN/m^2 (228 psf).

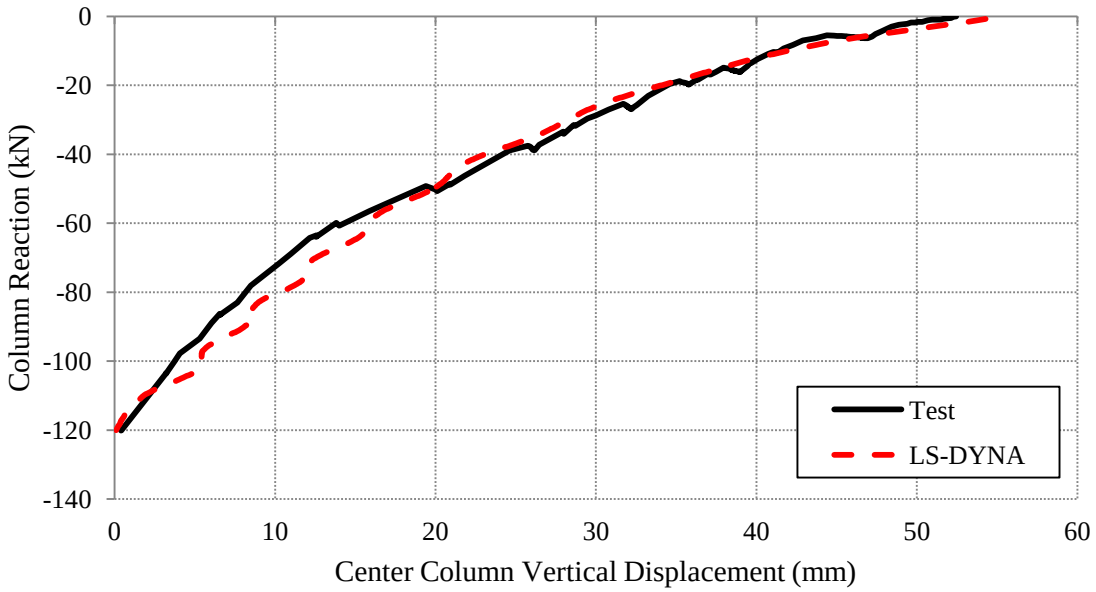

Figure 4.50: ICL Specimen: Column reaction versus vertical displacement

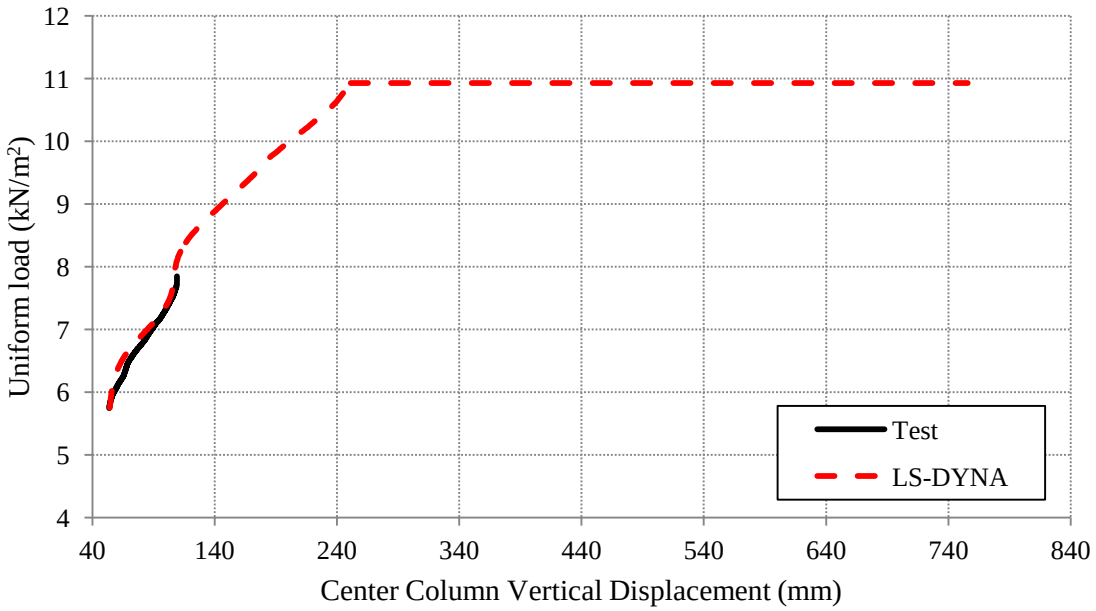

Figure 4.51: ICL Specimen: Superimposed load versus displacement after the removal of the support at the center column

As described in the previous chapter, the final test of the ICL specimen had all the bolts removed from the steel grillage. In this weakened condition, the specimen eventually collapsed. In the FE model, bolt removal was simulated at the end of the second stage of loading (Figure 4.49) by deleting all the solid elements (*DEFINE_ELEMENT_DEATH_SOLID_SET) that were used to represent the bolts. After these elements were removed from the model, the third stage of loading (Figure 4.49) was initiated, and the load was increased until collapse was achieved. Figure 4.52 shows a comparison of a video snapshot during collapse and the response of the FE model at the same state. It can be observed that the separation of the longitudinal lap is captured from the numerical model, and the overall response of the specimen is quite similar to the experimental one. The complete load-displacement curve is shown in Figure 4.53. The measured specimen collapse load of approximately 8 kN/m^2 (167 psf) is nearly identical to the predicted collapse load from the FE simulation.

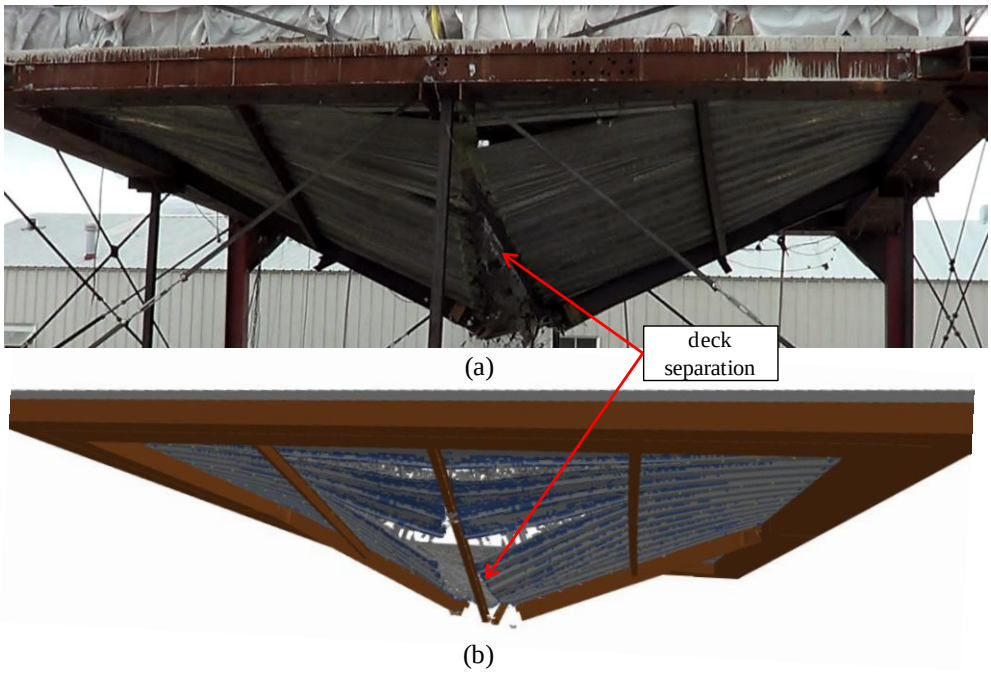

Figure 4.52: ICL Specimen during collapse: (a) Experimental test, (b) FE simulation

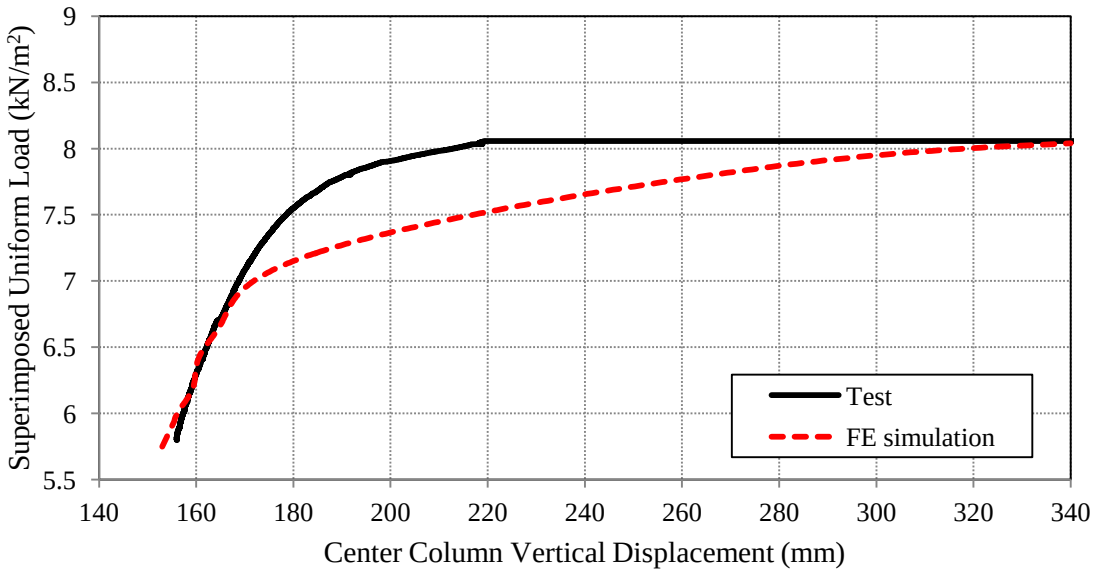

Figure 4.53: ICL Specimen: Superimposed load versus displacement after the removal of the support at the center column and all the bolts removed from the steel grillage

The ultimate collapse load of about 8 kN/m^2 is predicted with good accuracy and there is good agreement in vertical displacements up to a load of approximately 7 kN/m^2. Afterwards, the computational simulation predicts significant softening before total collapse. This difference can be attributed to the bearing failure of the steel deck around the shear studs that pass through and are welded to the top flange of the steel beams. Figure 4.54 shows a detail of the shear stud along the centerline of the specimen. Along this centerline, there was a longitudinal seam between the steel deck panels, which is speculated to have triggered collapse. This hypothesis is supported by video evidence as shown in Figure 4.52(a). As indicated in Figure 4.54, two separate deck panel pieces sit on the top flange of the W6×9 section and overlap over a length that is approximately equal to the width of that section. Then, the shear stud is welded to the beam top flange after melting the metal of the two overlapping deck panels. This construction sequence results in a circle-shape weld as shown in Figure 4.54, which creates circular-shaped holes in the two deck panels. As the deformations increase, the in-plane axial membrane force that is developed in the steel deck increases, causing the deck panels to bear against the shear stud. Figure 4.55(a) shows the deck condition at this location after collapse where the bearing-type failure mode is observed. Also, because of the increased temperatures that are developed during the welding of the shear stud, the steel deck material is speculated to have decreased ductility (Lee 2012), which causes a brittle-type bearing failure, as supported by the load-displacement response in Figure 4.53.

In the FE model, the altered deck material properties due to the increased temperatures were not included. For the FE models depicted in Figure 4.54, at a load of approximately 7.5 kN/m^2, the deck at the nodal locations coincident with the shear studs

experiences significant plastic deformations that in reality might have already caused fracture because of the reduced ductility of the decking material. At a higher load, these elements erode as shown in Figure 4.55(b), simulating the tear-out failure (Figure 4.55(a)). The effect of the welded shear stud through the deck panels was included by merging four coincident nodes at the location of each shear stud: (1) Base node of the shear stud, (2) Node at the top flange of the W6×9 section, (3&4) Nodes of the two deck panels. Therefore, the different material properties and the different fixity of the shear studs are speculated to cause the softening behavior (Figure 4.53) before collapse. Future research should investigate alternative modeling approaches to capture this effect.

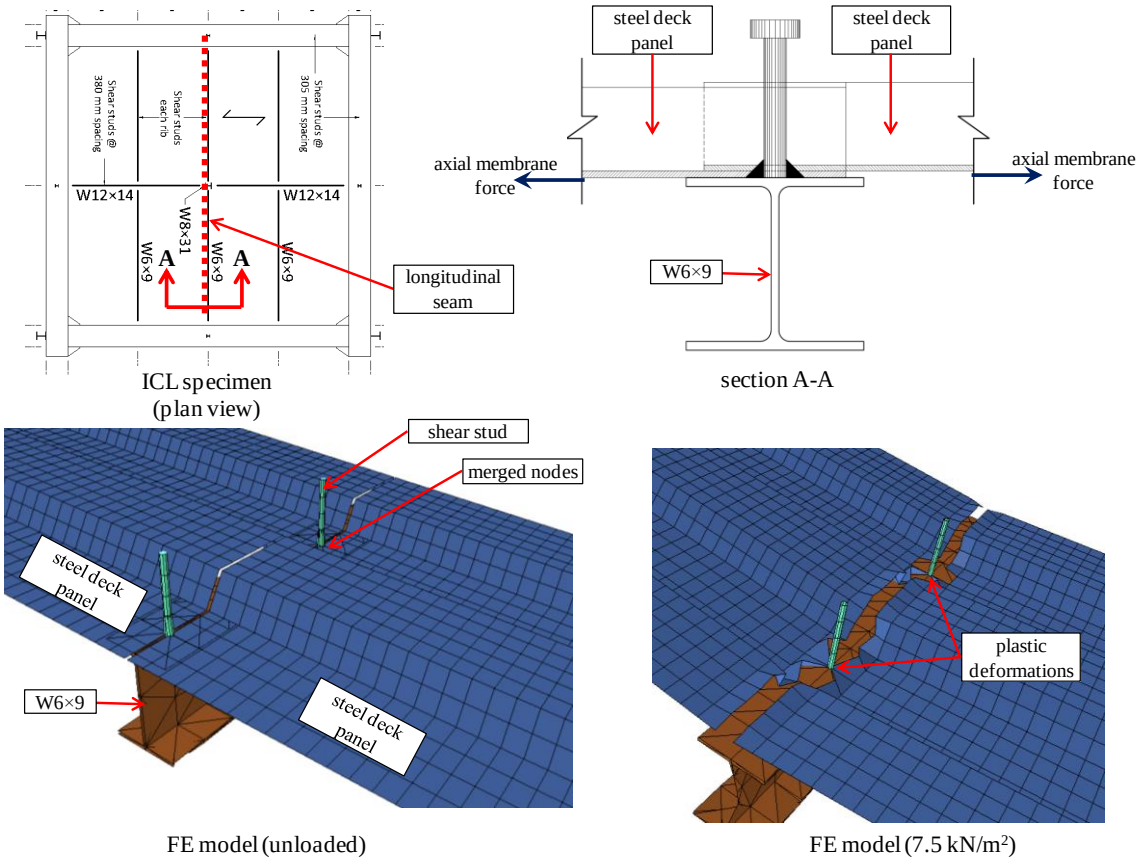

Figure 4.54: Steel deck longitudinal seam detail and implementation in the FE model (concrete slab is omitted for clarity)

(a)

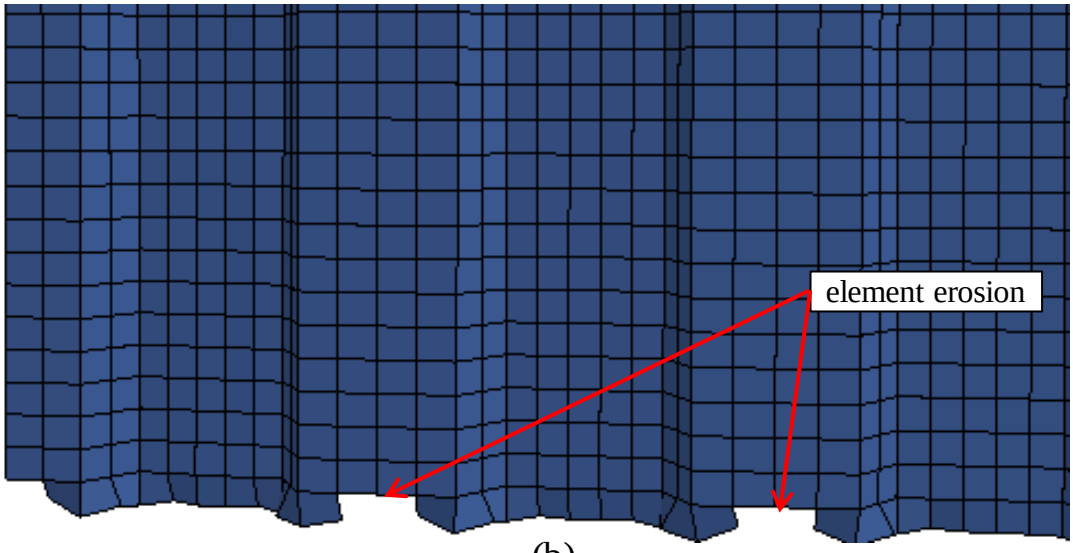

(b)

Figure 4.55: Tear-out failure of the steel deck around the shear studs caused by in-plane tensile forces, (a) Test specimen, (b) Captured in FE model with element erosion

4.3.4.2 ECL Specimen Response

The second test specimen, representing the removal of an exterior (façade) column, was initially loaded with a total load of 5.50 kN/m^2 uniformly distributed over the entire area of the floor slab. To represent the façade, a line load of 4.67 kN/m was applied along the exterior edge of the specimen. After the support at the exterior column was removed (Figure 4.49), the deflection increased to 120 mm, which similar to the deflection obtained from the FE simulation. Figure 4.56 shows the experimental column-reaction versus displacement curve and the one obtained from the FE analysis. The difference in the initial stiffness observed in Figure 4.56 up to a deflection of 35 mm is mainly attributed to preexisting cracking of the concrete slab of the specimen along the interior edge of the perimeter beam (Figure 4.29).

Under the absence of the perimeter column, the load on the slab slowly increased to 9.10 kN/m^2, causing total collapse of the specimen. A few seconds before collapse, the displacement was approximately 350 mm. The predicted collapse load from the FE simulation is 9.50 kN/m^2 at a deflection of 365 mm. The complete superimposed load versus deformation curve is shown in Figure 4.57. The flat parts on the experimental curve correspond to the incremental increase of the superimposed load, as described in the previous chapter. The load was raised in increments of 1 kN/m^2, and loading was reinitiated only after the deformations stabilized. For computational efficiency, the load in the FE simulation was not applied in increments. Nonetheless, good agreement can be observed between the measured and predicted response, and the overall behavior is similar.

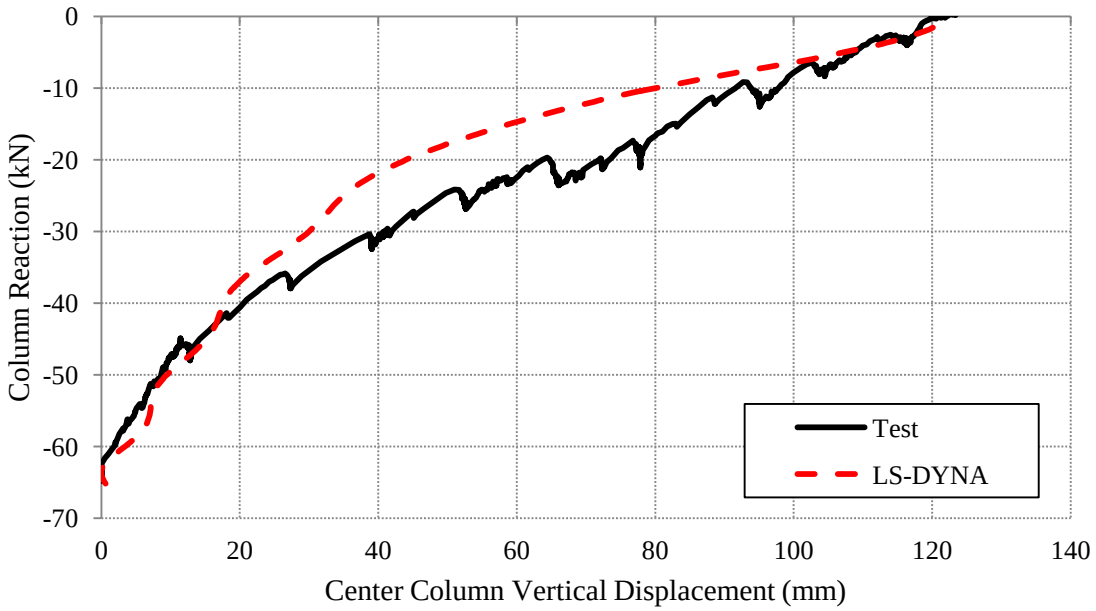

Figure 4.56: ECL Specimen: Column reaction versus vertical displacement

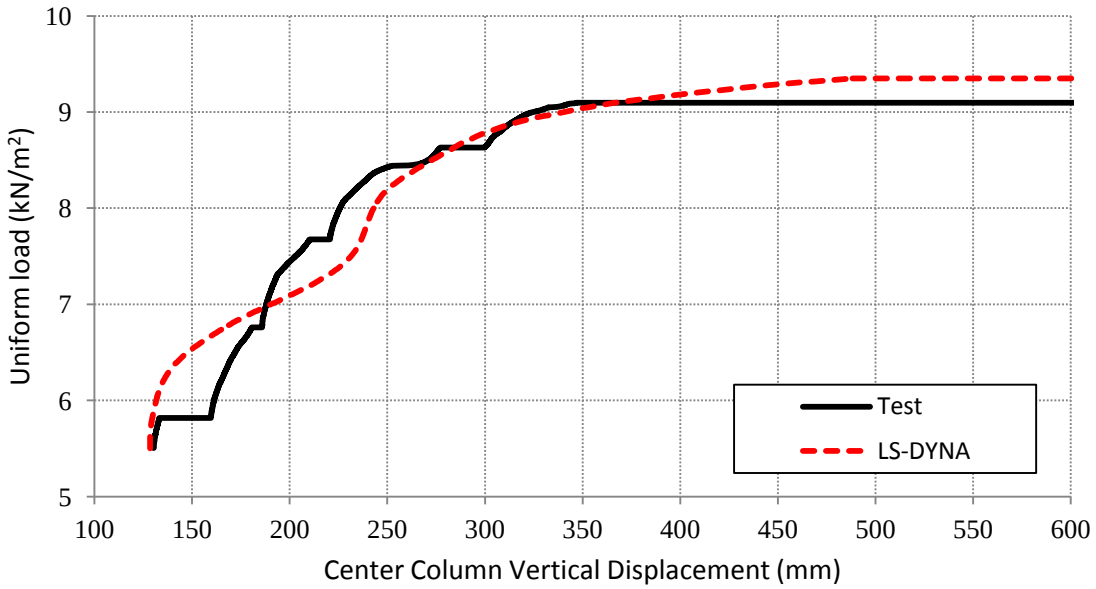

Figure 4.57: ECL Specimen: Superimposed load versus displacement after the removal of the support at the center column

Based on the FE model, the collapse of the slab was triggered by tensile fracture of the bolts that connected the floor beams to the middle column (i.e., the column that was removed). Verification of this failure mode cannot be made with certainty from the experimental tests because close observations during the tests were prohibited due to safety concerns. Nonetheless, videos of the collapse and the simulated collapse from the computational simulations show good correlation. In addition, observations made after the specimen collapsed are quite similar to those indicated by the FE simulation. The following figures provide evidence that further support these arguments.

Figure 4.58(a) shows a snapshot of video footage taken during collapse, and Figure 4.58(b) is a picture from the FE simulation at approximately the same state of collapse. Globally, comparing the two parts of the figure, the deflected shape and condition of the slab are in good agreement. Figure 4.59 shows the condition of the specimen during collapse from a different point of view. Again, it can be seen that the observed and predicted responses are quite similar. The separation of the steel decking because of failure at the side-lap is depicted in this figure, which is also captured in the FE simulation.

(a)

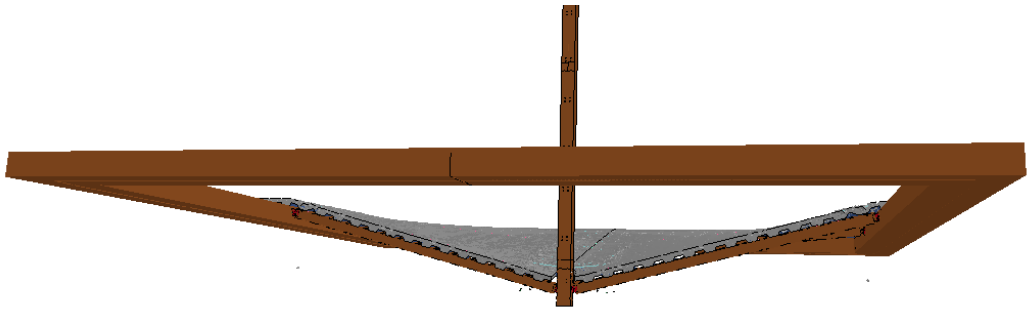

(b)

Figure 4.58: ECL Specimen during collapse, north view, (a) Experimental test, (b) FE simulation

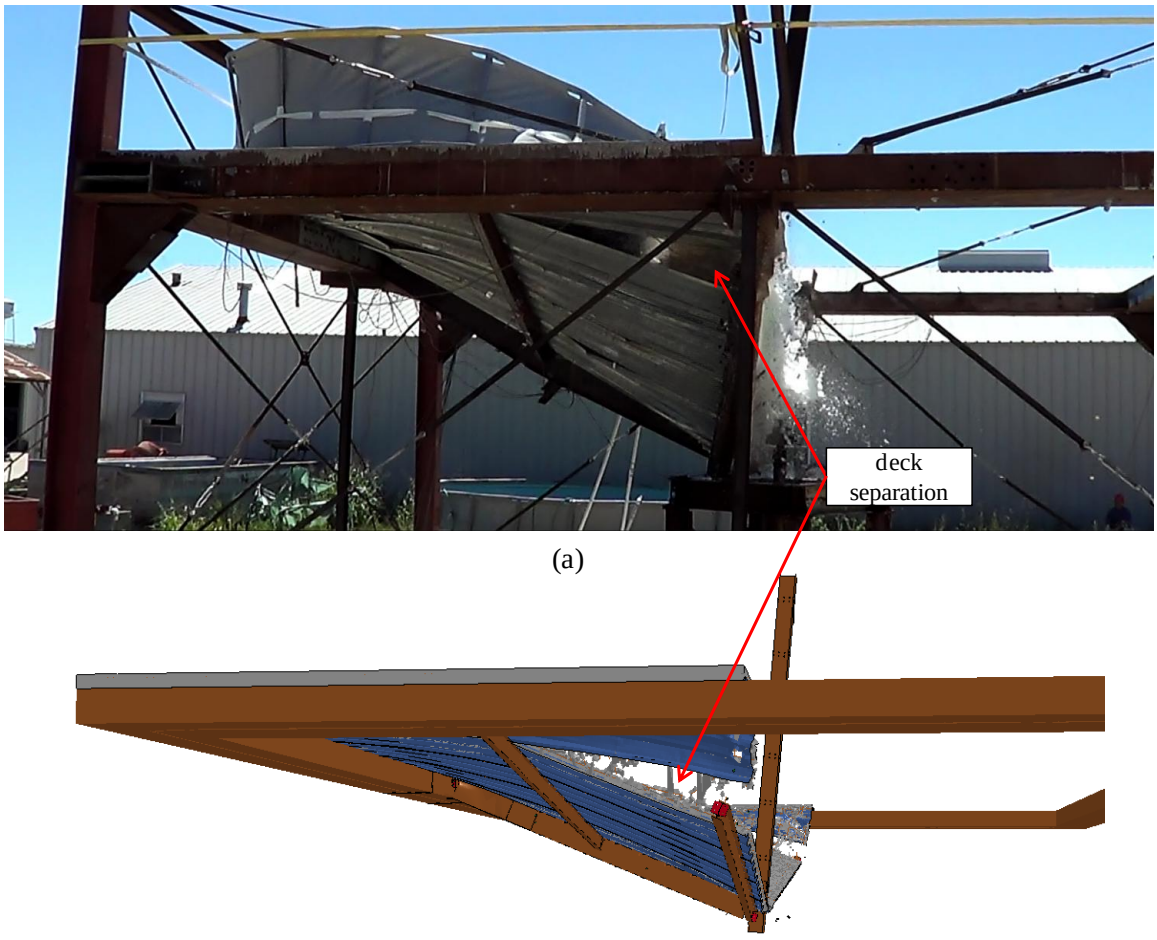

Figure 4.59: ECL Specimen during collapse, east view, (a) Experimental test, (b) FE simulation

In Figure 4.60, certain locations of the ECL specimen are depicted, and failure modes at these locations are compared with those from the FE simulations. Figure 4.61 provides a set of pictures for each one of these locations for comparison of their post-collapse condition. Figure 4.61(a) shows the post-collapse condition of the double angle connection of the main girder to perimeter beam connection. The failure modes of the test specimen and the FE model compare quite well; in both cases, the bolts did not fracture

because failure occurred in the other leg of the angle section, which was welded to the girder web. The condition of the shear tab connection between the secondary floor-beam to the perimeter beam is shown Figure 4.61(b). The shear tab plate fractured (not shown in the picture), while the two bolts remained intact. This response was also captured with the FE analyses. Contrary to the other double angle connection shown in Figure 4.61(a), the failure mode of the double angle connection of the floor beam to the perimeter beam was different, as shown in Figure 4.61(c). In this case, the bolts fractured while the angle sections remained intact, which is in agreement with the FE analyses. The residual plastic deformations that can be observed in the actual section are speculated to occur because of the falling debris during collapse and are not directly associated with the failure mode that caused the connection to fail.

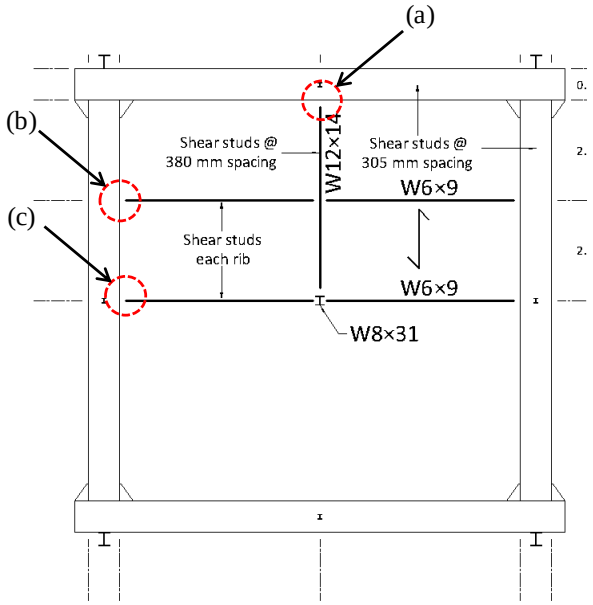

Figure 4.60: Locations of post-collapse pictures shown in subsequent figure

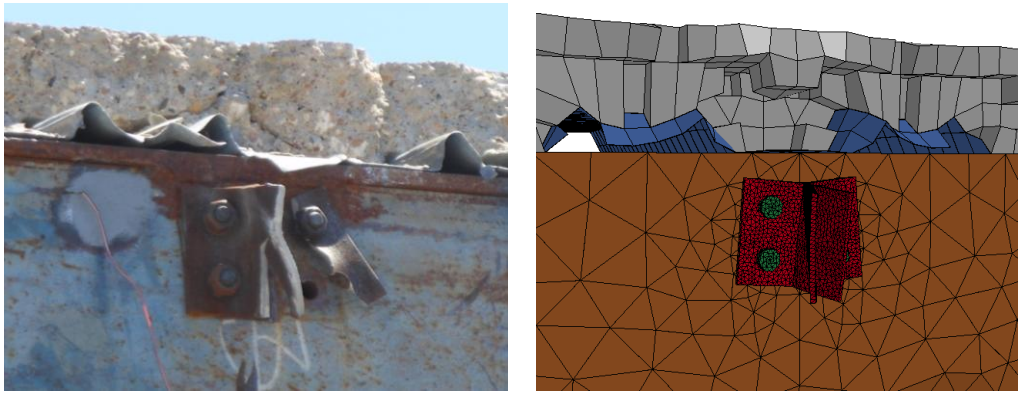

(a)

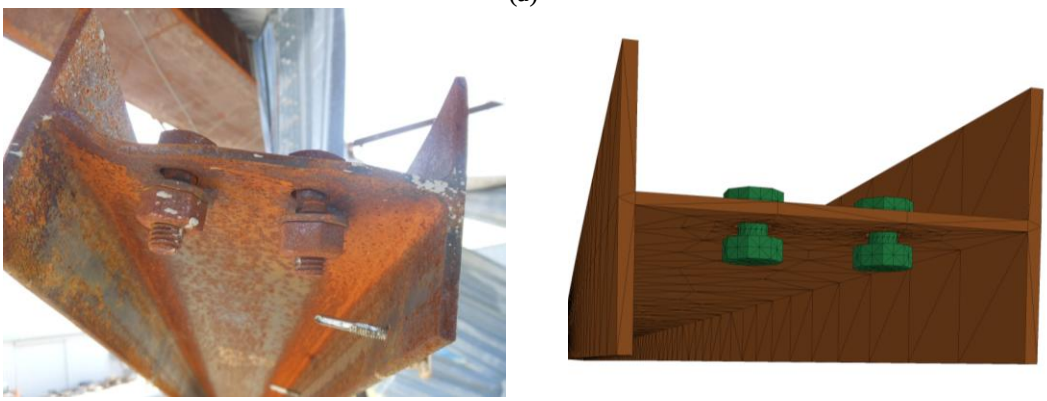

(b)

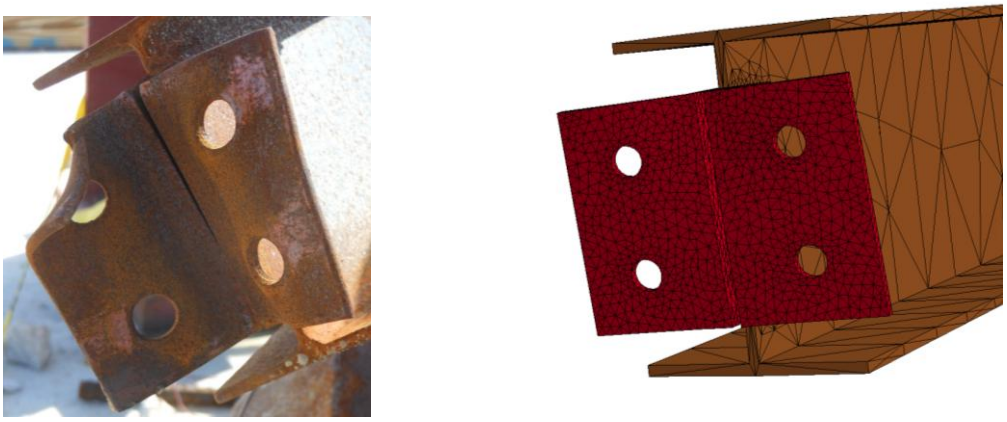

(c)

Figure 4.61: Comparison of post-collapse condition of ECL specimen with LS-DYNA analysis, (a) Double angle connection, (b) Shear tab connection, (c) Double angle connection (refer to previous figure)

4.3.5 Overview

This section presented the development and analysis of detailed computational models capable of simulating the physical tests conducted on the ICL and ECL specimens. All components in the experimental specimens were included in the computational models. Overall, the models were shown to be capable of capturing the experimental response with good accuracy. The strength and stiffness of the computational models were in good agreement with the experimental data. It is also important that the ultimate capacities of the floor slabs prior to collapse were predicted with less than 10% error. Comparisons of the observed failure modes at specific locations, both during and after collapse, agree well with those predicted by the FE models. Because these models were validated against experimental results, they are believed to provide an accurate representation of the key response modes exhibited by composite floor systems during collapse. Additional analyses are presented in the next section to identify the contribution of the various components of the floor system and to examine potential improvements that can enhance the resiliency of composite floor systems under abnormal loading conditions.

4.4 SENSITIVITY STUDY

Several parameters were altered in the computational models to obtain a better understanding of the contribution made by different components in the collapse behavior and capacity of the specimens. The model representing the ICL specimen was chosen for the study presented in this section. The analyses were performed by assuming the column was not supported from the beginning of the loading. This condition corresponds to the

third loading stage of the previous analyses as shown in Figure 4.49(c), with the difference being that there was no preexisting load on the slab. Therefore, the load was ramped from zero to a certain value and then held constant. The total applied load acting on the specimen was incrementally increased until collapse occurred. The FE model representing the ICL specimen was analyzed with the new loading scheme, but no other modifications were made to the baseline analysis. This benchmark model was compared with five different scenarios:

(a) Bolt ductility: The ductility of the bolts was increased by 50% while their ultimate strength was kept the same.

(b) Deck continuity: The steel deck was assumed to be continuous in the direction perpendicular to its flutes. As observed during the ICL test, separation of the longitudinal seam (Figure 4.52) was speculated to trigger the collapse of this specimen.

(c) WWM size: The WWM diameter was increased from 3.175-mm to 12.7-mm, which corresponds to the size of #4 reinforcing bars. It is noted that the material properties were similar to those obtained from the tension tests of the WWM shown in Figure 4.42.

(d) No steel deck: The steel deck was removed from the model, though the concrete topping was not.

(e) No concrete: The concrete topping with all the associated steel reinforcement was removed from the model, but the steel deck remained in the model.

Figure 4.62 shows the load-displacement response for each scenario considered. For comparison purposes, the response of the benchmark model is also included. The benchmark model has an ultimate capacity of 10.90 kN/m^2 (228 psf). By increasing the bolt ductility by 50%, the ultimate collapse load increases by approximately 10% to an ultimate load of 12.10 kN/m^2 (253 psf). Providing deck continuity increases the ultimate capacity of the specimen by more than 40%, resulting in an ultimate collapse load of 15.50 kN/m^2 (324 psf). Using 12.7-mm diameter reinforcing bars instead of the 3.175-mm diameter WWM at the same spacing of 150-mm orthogonally placed, the collapse load increases considerably to nearly three times the ultimate capacity of the benchmark model, which corresponds to a total load of approximately 33 kN/m^2 (690 psf). These results suggest that deck continuity and additional structural reinforcement can potentially improve the resiliency of such structures. Deck continuity especially can be implemented in such structures with very little cost, with the addition of enough tek-screws between the adjacent deck panels so they can develop their full in-plane axial capacity.

It is also interesting to compare the ultimate capacities of the last two scenarios: (a) no steel deck, (b) no concrete. The collapse load of these two cases is considerably less than the benchmark model. Specifically, the model without the concrete slab collapses at a load of approximately 2.90 kN/m^2 (60 psf), and the model with the concrete slab only collapses at a load of 6.90 kN/m^2 (144 psf). The additive capacities of the two models, however, results in a load of 9.80 kN/m^2 (204 psf), which is close to the collapse load of 10.90 kN/m^2 (228 psf) of the benchmark model. This observation demonstrates that the interaction of these two components (i.e., the concrete slab and the supporting

steel deck) contribute significantly to the ultimate capacities of such floor systems. This finding is consistent with findings from previous computational studies on similar floor slabs performed by Sadek, *et al.* (2008).

In Figure 4.62, it can be also observed that models (a) through (c) (i.e., those with design enhancements) have a higher capacity than the benchmark model after a deformation of approximately 300-mm. Significant softening starts to occur at this deformation level, which is attributed to the failure of the center beam-to-column connection due to bolt fracture, eventually causing the models to collapse. The only model that softens at this deformation level but can sustain additional load before collapse is the one with the 12.7-mm diameter reinforcing bars. The increased capacity provided from the reinforcing bars, due to their cable-like action under the increased deformations, is able to arrest collapse after the failure of the center connection. At a deformation of approximately 430-mm, the model can sustain additional load, and the model eventually collapses due to fracture of these reinforcing bars.

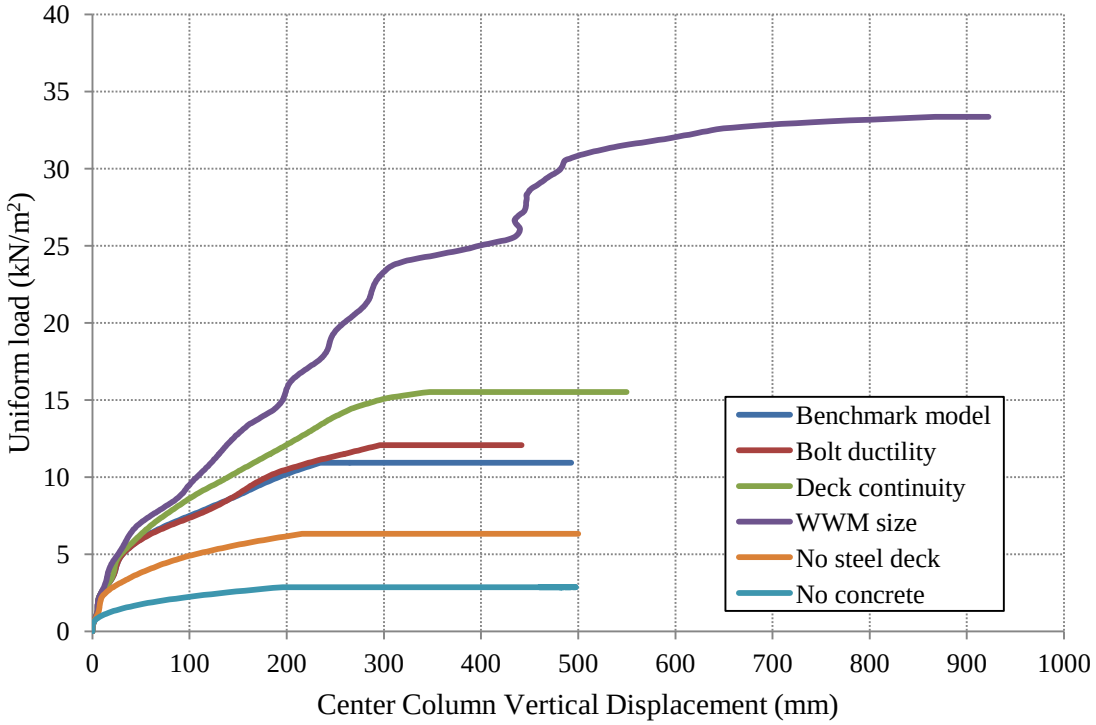

Figure 4.62: Load-displacement curves for the ICL specimen analyses

4.5 CHAPTER OVERVIEW

This chapter provided a thorough description of the computational modeling performed to simulate the response of the experimental tests. The ultimate goal of the computational studies was to gain confidence in modeling procedures that can be used to predict the response of entire structural systems under scenarios associated with abnormal loading conditions, such as the loss of a column. Prior to analyzing the test specimens, high-fidelity FE models of individual structural components were analyzed to ensure the various modeling parameters used for these components provided sufficiently accurate

results. The results from these analyses were validated and verified with previous experimental data.

Following similar procedures, detailed three-dimensional computational models of the ICL and ECL specimens were developed. The experimental procedure followed during the physical tests was numerically simulated, and comparisons were made with the experimental data. Agreement between the predicted and measured responses was good. The FE models were capable of predicting the overall response of the two specimens and the ultimate collapse load with good accuracy. The failure modes that triggered collapse were identified, and comparisons with the post-collapse condition of the tests also showed good agreement.

The sensitivity of the FE models to changes in several important design parameters was also investigated. These studies were used to evaluate improved design provisions for composite floor slabs subjected to abnormal loading conditions. Appendix A includes the input cards used in the FE models. The following chapter summarizes the experimental and computational work performed in this study. Conclusions and areas needing further investigation are also identified.

CHAPTER 5

SUMMARY, CONCLUSIONS AND FUTURE WORK

5.1 SUMMARY OF COMPLETED WORK

This dissertation presented an investigation on the response of steel-concrete composite floor systems under single column removal scenarios. The study included large-scale physical testing of two different specimens, each with its own unique column removal case. Detailed finite element models of these composite floor slabs were developed, and they were able to provide valid predictions of each specimen's response following the removal of a single column.

The two specimens represented isolated portions of the gravity-load resisting system of a typical steel-framed building with simple shear connections. A single column was removed during each test. One test represented an interior column loss case, while the other represented an exterior (façade) column loss case. Upon the successful removal of the designated column, additional load was added to the slab of both specimens until total collapse was achieved. The experimental data gathered from these tests provide valuable information on the response and ultimate capacity of such floor systems after the loss of a single column.

The experimental data from these tests were subsequently used to develop and validate high-fidelity finite element models using the general purpose, multi-physics code LS-DYNA (Hallquist 2013). A thorough validation study of the individual components that make up a typical composite floor system was performed to ensure that the modeling procedure followed provided valid results. Subsequently, the test specimens were

analyzed by explicitly modeling all of their components. The numerical models were capable of predicting the response and ultimate collapse load of the specimens with acceptable accuracy. Further investigations on the numerical models were performed to identify the parameters that most strongly influence the computed response of these floor systems.

5.2 CONCLUSIONS

The conclusions from this work are divided into two different sections, reflecting the two major parts of this study—the physical testing and computational modeling.

5.2.1 Test Specimen Response

Observations from the experimental tests lead to the following conclusions:

1. Although the specimens did not have any special design provisions for increased resiliency to resist progressive collapse, they sustained the removal of a mid-span column under the DoD-recommended (2013) design load for progressive collapse.
2. Prior to their collapse, the specimens sustained additional superimposed load under the absence of the mid-span column. The collapse load was higher than the required progressive collapse design load, including dynamic effects associated with actual damage events (DoD 2013).
3. The specimens had enough capacity to resist the collapse scenario without the need to apply special design provisions to resist progressive collapse as suggested in UFC 4-03-23 (2013). Application of the tie force method would result in an increased, but no required capacity, since the specimens already

had adequate capacity with their current design. This indicates that these provisions might be conservative in some cases, since the inherit capacity in certain structural systems and configurations is adequate to resist extreme loading scenarios.

4. Despite the absence of single mid-span column, both specimens eventually sustained a load that was higher than their ultimate design load.
5. Deck continuity in the direction perpendicular to the deck corrugations was found to be an important parameter in the ultimate capacity of the floor slab. Based on video evidence from the ICL specimen, collapse initiated when separation of the corrugated steel decking occurred due to the development of tensile in-plane forces large enough to cause separation of the longitudinal lap. It is expected that the floor system capacity would be higher if this lap joint was detailed appropriately to allow for the development of larger in-plane tensile forces.
6. In some cases, creep effects raised the vertical displacements as much as 20% several hours after column removal took place. Applying this result to actual structures, collapse might potentially occur several hours after one or more load-carrying members suffer localized damage, emphasizing the importance of continued monitoring of damaged buildings.

5.2.2 Numerical Modeling

After developing detailed finite element models and performing multiple numerical analyses capable of capturing the response of the specimens with reasonable accuracy, the following conclusions are made:

1. The high-fidelity numerical modeling procedure developed during this study showed good correlation with the measured test data. These results suggest such an approach can be extended to predict the response of similar floor systems with different geometries and design properties.
2. Response predictions were sensitive to the specified material properties. Using nominal values based on ASTM standards, particularly for the steel components, led to inaccurate predictions of structural response. Only when measured lab values were used for the material properties did the computed results correlate well with those observed during the large-scale testing.
3. Deck continuity was confirmed to have an appreciable influence on the ultimate capacity of the floor slab after column removal. The ultimate load-carrying capacity of the floor slab increased by 40% when the corrugated steel deck was assumed to be continuous over the entire area of the floor slab. In an actual structure, deck continuity can be enhanced by increasing the overlap distance between adjacent panels and by increasing the number of tek-screws used to fasten the panels together.
4. Substituting the WWM with appropriately anchored reinforcing bars had a significant influence on the ultimate load-carrying capacity of the floor system. After replacing the 3.175-mm diameter WWM with 12.7-mm

diameter reinforcing bars of equal 150-mm spacing, the ultimate capacity of the slab increased by approximately 300%.

5. The 300% increase in the load carrying capacity of the slab after increasing the diameter of the reinforcement indicates that the tie force method (DoD 2013) might result in conservative designs. More relaxed design requirements might still be sufficient in some cases.
6. The numerical analyses showed that a great part of the load-carrying capacity of the composite floor system is provided by the corrugated steel deck acting in conjunction with the concrete slab.

5.3 FUTURE WORK

Based on the observations and conclusions presented in this work, areas that require further investigation have been identified. The list below includes opportunities for both experimental and computational investigations:

1. Additional research is needed to characterize the time-dependent phenomena observed during testing. Recall that, in some tests, vertical deformations continued to increase while the load was held constant. Slipping between the bolted steel components and relative displacement at the interface between the concrete slab and steel decking are speculated to be the primary causes of increasing displacement under constant load, but additional tests are required to confirm this hypothesis.
2. Further study is needed to evaluate the suitability of the perimeter beam used in the tests. The perimeter beam was designed to approximate the

boundary conditions provided by adjacent bays in an actual building. Using the numerical modeling guidelines developed during the current research, the adjacent bays of the prototype building can be modeled explicitly to determine how the floor system in the directly affected bays compares with the one restrained by the perimeter beam.

3. Experimental testing is needed to evaluate design/construction details that are capable of ensuring continuity is maintained between adjacent corrugated deck panels. The primary goal would be the development of connection details that allow the deck to develop its full axial capacity.
4. Additional tests are needed to evaluate the response of floor systems with different configurations and geometries from those tested in the current study.
5. Numerical studies are needed to simulate the loss of a column dynamically so the accuracy of the dynamic increase factors specified in the DoD (2013) design criteria for progressive collapse can be evaluated in light of the research results obtained during the current project.
6. Examine the efficiency of certain design provisions for buildings to resist progressive collapse, such as the tie force method. Possible relaxation of these provisions might lead to significant cost reductions since results indicate that they can be overly conservative.

It is evident that many complex behaviors are developed in steel structures when reaching their ultimate collapse load, where these complexities are mainly attributed to material and geometrical non-linearities. This study provides valuable experimental data

and a valid numerical modeling approach that can be used in future research studies to gain a better understanding of the collapse behavior of structures under various damage scenarios. Safer and more resilient structures can be designed as a result of on-going research studies in this field.

APPENDIX A

LS-DYNA INPUT MATERIAL CARDS

A.1 INPUT PARAMETERS

The input material cards used in LS-DYNA for the numerical models that were simulating the physical tests are given below.

```
*KEYWORD
*TITLE
$#                                                                         title
TEST_SPECIMEN
$#########################################################################
$                                  CONTROL
$#########################################################################
*CONTROL_SHELL
$#  wrpang      esort      irnxx     istupd     theory        bwc      miter       proj
 20.000000          1         -1          0          2          2          1          0
$# rotascl     intgrd     lamsht     cstyp6     tshell
  1.000000          0          0          1          0          1          1          0
$# psstupd   sidt4tu      cntco     itsflg     irquad
          0          0          0          0          2
*CONTROL_SOLID
$#   esort    fmatrix    niptets      swlocl     psfail    t10jtol
          0          0          4          2          0      0.000
$#    pm1       pm2       pm3       pm4       pm5       pm6       pm7       pm8       pm9      pm10
        0         0         0         0         0         0         0         0         0         0
*CONTROL_TERMINATION
$#  endtim     endcyc      dtmin     endeng     endmas
 12.000000          0      0.000      0.000      0.000
*CONTROL_TIMESTEP
$#  dtinit     tssfac       isdo     tslimt      dt2ms       lctm      erode      mslst
     0.000   0.900000          0      0.000 -4.000E-6          0          0          0
$#  dt2msf    dt2mslc      imscl     unused     unused      rmscl
     0.000          0          0                           0.000
$#########################################################################
$                                  DATABASE
$#########################################################################
*DATABASE_NODOUT
$#       dt     binary       lcur      ioopt    option1    option2
 1.0000E-2          0          0          1      0.000          0
*DATABASE_RCFORC
$#       dt     binary       lcur      ioopt
 1.0000E-2          0          0          1
*DATABASE_SPCFORC
$#       dt     binary       lcur      ioopt
 1.0000E-2          0          0          1
*DATABASE_BINARY_D3PLOT
$#       dt       lcdt       beam      npltc     psetid
 1.0000E-2          0          0          0          0
$#
ioopt
          0
*DATABASE_HISTORY_NODE
$#     id1        id2        id3        id4        id5        id6        id7        id8
     25089          0          0          0          0          0          0          0
$#########################################################################
$                                  CONTACT
$#########################################################################
#### *CONTACT_AUTOMATIC_SINGLE_SURFACE_ID
$#     cid                                                                 title
```

```
$#     ssid      msid     sstyp     mstyp    sboxid    mboxid       spr       mpr
        88         0         6         0         0         0         0         0
$#       fs        fd        dc        vc       vdc    penchk        bt        dt
  0.400000  0.300000     0.000     0.000     0.000         0    0.0001.0000E+20
$#      sfs       sfm       sst       mst      sfst      sfmt       fsf       vsf
  1.000000  1.000000     0.000     0.000  1.000000  1.000000  1.000000  1.000000
$#     soft    sofscl    lcidab    maxpar     sbopt     depth     bsort    frcfrq
        0  0.100000         0  1.025000  2.000000         2         0         1
$#  penmax    thkopt    shlthk     snlog      isym     i2d3d    sldthk    sldstf
     0.000         0         0         0         0         0     0.000     0.000
$#     igap    ignodprfac/mpadtstif/mpar2   unused      unused    flangl   cid_rcf
        1         1     0.000     0.000                          0.000         0
$#########################################################################################
$                                      MATERIALS
$#########################################################################################
*MAT_PIECEWISE_LINEAR_PLASTICITY_TITLE
Steel.Beams_Parts
$#     mid        ro         e        pr      sigy      etan      fail      tdel
         6 7.8000E-9 2.1000E+5  0.290000 245.00000     0.000  0.350000     0.000
$#       c         p      lcss      lcsr        vp
     0.000     0.000         0         0     0.000
$#    eps1      eps2      eps3      eps4      eps5      eps6      eps7      eps8
     0.000 1.2953E-2 4.1244E-2  0.179800  0.200000     0.000     0.000     0.000
$#     es1       es2       es3       es4       es5       es6       es7       es8
 250.30000 258.64001 438.60001 528.00000 540.00000     0.000     0.000     0.000
$
*MAT_PIECEWISE_LINEAR_PLASTICITY_TITLE
Steel.ShearTab_RingBeam
$#     mid        ro         e        pr      sigy      etan      fail      tdel
        17 7.8000E-9 2.1000E+5  0.290000 300.00000     0.000  0.575000     0.000
$#       c         p      lcss      lcsr        vp
     0.000     0.000         0         0     0.000
$#    eps1      eps2      eps3      eps4      eps5      eps6      eps7      eps8
     0.000 1.5000E-2 5.8000E-2  0.140000  0.300000  0.570000     0.000     0.000
$#     es1       es2       es3       es4       es5       es6       es7       es8
 300.00000 305.00000 370.00000 420.00000 500.00000 360.00000     0.000     0.000
$
*MAT_PIECEWISE_LINEAR_PLASTICITY_TITLE
Steel.W12X14
$#     mid        ro         e        pr      sigy      etan      fail      tdel
        15 7.8000E-9 2.1000E+5  0.290000 382.00000     0.000  0.500000     0.000
$#       c         p      lcss      lcsr        vp
     0.000     0.000         0         0     0.000
$#    eps1      eps2      eps3      eps4      eps5      eps6      eps7      eps8
     0.000 3.2000E-2 5.5000E-2  0.129000  0.204000  0.385000  0.480000     0.000
$#     es1       es2       es3       es4       es5       es6       es7       es8
 390.00000 400.00000 471.00000 551.00000 594.00000 620.00000 645.00000     0.000
$
*MAT_PIECEWISE_LINEAR_PLASTICITY_TITLE
Steel.Angle
$#     mid        ro         e        pr      sigy      etan      fail      tdel
        16 7.8000E-9 2.1000E+5  0.290000 290.00000     0.000  0.465000     0.000
```

```
$#       c         p      lcss      lcsr        vp
     0.000     0.000         0         0     0.000
$#     eps1      eps2      eps3      eps4      eps5      eps6      eps7      eps8
     0.000 1.1000E-2 4.4000E-2  0.110000  0.240000  0.460000     0.000     0.000
$#      es1       es2       es3       es4       es5       es6       es7       es8
 291.00000 405.00000 512.00000 595.00000 655.00000 520.00000     0.000     0.000
$
*MAT_PIECEWISE_LINEAR_PLASTICITY_TITLE
Steel.W6X9
$#     mid        ro         e        pr      sigy      etan      fail      tdel
        14 7.8000E-9 2.1000E+5  0.290000 382.00000     0.000  0.435000     0.000
$#       c         p      lcss      lcsr        vp
     0.000     0.000         0         0     0.000
$#     eps1      eps2      eps3      eps4      eps5      eps6      eps7      eps8
     0.000 3.2000E-2 7.0000E-2  0.129000  0.204000  0.251900  0.430000     0.000
$#      es1       es2       es3       es4       es5       es6       es7       es8
 385.00000 394.00000 488.00000 551.00000 594.00000 600.00000 665.00000     0.000
$
*MAT_PIECEWISE_LINEAR_PLASTICITY_TITLE
Steel.ShearTab_Girder
$#     mid        ro         e        pr      sigy      etan      fail      tdel
        18 7.8000E-9 2.1000E+5  0.290000 355.00000     0.000  0.430000     0.000
$#       c         p      lcss      lcsr        vp
     0.000     0.000         0         0     0.000
$#     eps1      eps2      eps3      eps4      eps5      eps6      eps7      eps8
     0.000 1.0000E-2 3.4000E-2 8.6000E-2  0.225000  0.425000     0.000     0.000
$#      es1       es2       es3       es4       es5       es6       es7       es8
 356.00000 364.00000 518.00000 620.00000 705.00000 535.00000     0.000     0.000
$
*MAT_CSCM_CONCRETE_TITLE
Concrete
$#     mid        ro     nplot     incre     irate     erode     recov   itretrc
         2 2.5000E-9         1     0.000         0  1.000000     0.000         0
$#    pred
     0.000
$#      fpc      dagg     units
 40.000000     0.000         2
$
*MAT_PIECEWISE_LINEAR_PLASTICITY_TITLE
Steel.Studs
$#     mid        ro         e        pr      sigy      etan      fail      tdel
         3 7.8000E-9 2.1000E+5  0.290000 440.00000 250.00000  0.300000     0.000
$#       c         p      lcss      lcsr        vp
     0.000     0.000         0         0     0.000
$#     eps1      eps2      eps3      eps4      eps5      eps6      eps7      eps8
     0.000     0.000     0.000     0.000     0.000     0.000     0.000     0.000
$#      es1       es2       es3       es4       es5       es6       es7       es8
     0.000     0.000     0.000     0.000     0.000     0.000     0.000     0.000
$
*MAT_PIECEWISE_LINEAR_PLASTICITY_TITLE
Steel.Deck
$#     mid        ro         e        pr      sigy      etan      fail      tdel
         4 7.8000E-9 2.1000E+5  0.290000 325.00000     0.000  0.255000     0.000
```

```
$#       c         p      lcss      lcsr        vp
     0.000     0.000         0         0     0.000
$#    eps1      eps2      eps3      eps4      eps5      eps6      eps7      eps8
     0.000 2.7000E-2 4.5990E-2 5.5360E-2   0.125000  0.165000  0.220000     0.000
$#     es1       es2       es3       es4       es5       es6       es7       es8
 330.00000 337.00000 368.00000 378.00000 414.00000 423.00000 423.00000     0.000
$
*MAT_PIECEWISE_LINEAR_PLASTICITY_TITLE
#WWM
$#     mid        ro         e        pr      sigy      etan      fail      tdel
        21 7.8000E-9 2.1000E+5   0.290000 700.00000     0.000 4.0000E-2     0.000
$#       c         p      lcss      lcsr        vp
     0.000     0.000         0         0     0.000
$#    eps1      eps2      eps3      eps4      eps5      eps6      eps7      eps8
     0.000 4.0000E-2     0.000     0.000     0.000     0.000     0.000     0.000
$#     es1       es2       es3       es4       es5       es6       es7       es8
 700.00000 740.00000     0.000     0.000     0.000     0.000     0.000     0.000
$
*MAT_PIECEWISE_LINEAR_PLASTICITY_TITLE
#3Rebars
$#     mid        ro         e        pr      sigy      etan      fail      tdel
        20 7.8000E-9 2.1000E+5   0.290000 580.00000     0.000  0.149000     0.000
$#       c         p      lcss      lcsr        vp
     0.000     0.000         0         0     0.000
$#    eps1      eps2      eps3      eps4      eps5      eps6      eps7      eps8
     0.000 1.7840E-2 6.7600E-2   0.148000     0.000     0.000     0.000     0.000
$#     es1       es2       es3       es4       es5       es6       es7       es8
 580.00000 580.00000 740.00000 780.00000     0.000     0.000     0.000     0.000
$
*MAT_PIECEWISE_LINEAR_PLASTICITY_TITLE
Steel.Bolts
$#     mid        ro         e        pr      sigy      etan      fail      tdel
         7 7.8000E-9 2.1000E+5   0.290000 830.00000     0.000  0.135000     0.000
$#       c         p      lcss      lcsr        vp
     0.000     0.000         0         0     0.000
$#    eps1      eps2      eps3      eps4      eps5      eps6      eps7      eps8
     0.000 1.3300E-2 2.8000E-2 4.6000E-2   0.109700  0.110000     0.000     0.000
$#     es1       es2       es3       es4       es5       es6       es7       es8
 830.00000 850.00000 860.00000 850.00000 850.00000 850.00000     0.000     0.000
$
*MAT_GENERAL_NONLINEAR_6DOF_DISCRETE_BEAM_TITLE
TEK_Screws
$#     mid        ro        kt        kr   unldopt    offset     dampf     iflag
        12 7.8000E-9     0.000     0.000         0     0.000     0.000         0
$#  lcidtr    lcidts    lcidtt    lcidrr    lcidrs    lcidrt
         6         6         7         0         0         0
$# lcidtur   lcidtus   lcidtut   lcidrur   lcidrus   lcidrut
         0         0         0         0         0         0
$# lcidtdr   lcidtds   lcidtdt   lcidrdr   lcidrds   lcidrdt
         0         0         0         0         0         0
$# lcidter   lcidtes   lcidtet   lcidrer   lcidres   lcidret
         0         0         0         0         0         0
$# utfailr   utfails   utfailt   wtfailr   wtfails   wtfailt
```

```
 11.000000 11.000000  2.500000     0.000     0.000     0.000
$# ucfailr   ucfails   ucfailt   wcfailr   wcfails   wcfailt
 11.000000 11.000000  2.500000     0.000     0.000     0.000
$#     iur       ius       iut       iwr       iws       iwt
     0.000     0.000     0.000     0.000     0.000     0.000
*DEFINE_CURVE_TITLE
TEK_Screw_Shear_Full
$#    lcid      sidr       sfa       sfo      offa      offo    dattyp
         4         0  1.000000  1.000000     0.000     0.000         0
$#                al                  ol
              0.000               0.000
             0.650000         2000.000000
             1.650000         3000.000000
             4.000000         3950.000000
             6.500000         4300.000000
            15.000000         2800.000000
            21.000000               0.000
            25.000000               0.000
*DEFINE_CURVE_TITLE
TEK_Screw_Tensile_Full
$#    lcid      sidr       sfa       sfo      offa      offo    dattyp
         5         0  1.000000  1.000000     0.000     0.000         0
$#                al                  ol
              0.000               0.000
             1.000000         1200.000000
             2.000000         1500.000000
             2.200000               0.000
             2.500000               0.000
$
$#########################################################################################
$                                      PARTS
$#########################################################################################
*PART
$#                                                                                  title
RING_BEAM
$#     pid      secid        mid      eosid       hgid       grav     adpopt       tmid
         1          1          6          0          0          0          0          0
*PART
$#                                                                                  title
SHEAR_TAB_RINGBEAM
$#     pid      secid        mid      eosid       hgid       grav     adpopt       tmid
         2          1         17          0          0          0          0          0
*PART
$#                                                                                  title
COLUMN
$#     pid      secid        mid      eosid       hgid       grav     adpopt       tmid
         3          1          6          0          0          0          0          0
*PART
$#                                                                                  title
MAIN_GIRDER
$#     pid      secid        mid      eosid       hgid       grav     adpopt       tmid
         4          1         15          0          0          0          0          0
```

```
*PART
$#                                                                    title
ANGLES
$#     pid     secid       mid     eosid      hgid      grav    adpopt      tmid
         5         1        16         0         0         0         0         0
*PART
$#                                                                    title
SECONDARY_BEAM
$#     pid     secid       mid     eosid      hgid      grav    adpopt      tmid
         6         1        14         0         0         0         0         0
*PART
$#                                                                    title
SHEAR_TAB_GIRDER
$#     pid     secid       mid     eosid      hgid      grav    adpopt      tmid
         7         1        18         0         0         0         0         0
*PART
$#                                                                    title
FLOOR_BEAM
$#     pid     secid       mid     eosid      hgid      grav    adpopt      tmid
         8         1        14         0         0         0         0         0
*PART
$#                                                                    title
Concrete
$#     pid     secid       mid     eosid      hgid      grav    adpopt      tmid
        31         2         2         0         0         0         0         0
*PART
$#                                                                    title
Shear Studs
$#     pid     secid       mid     eosid      hgid      grav    adpopt      tmid
        57         3         3         0         0         0         0         0
*PART
$#                                                                    title
Shear Studs Symmetry
$#     pid     secid       mid     eosid      hgid      grav    adpopt      tmid
        58         4         3         0         0         0         0         0
*PART
$#                                                                    title
Deck
$#     pid     secid       mid     eosid      hgid      grav    adpopt      tmid
        59         5         4         0         0         0         0         0
*PART
$#                                                                    title
WWM
$#     pid     secid       mid     eosid      hgid      grav    adpopt      tmid
       110        11        21         0         0         0         0         0
*PART
$#                                                                    title
Negative_Moment_Bars
$#     pid     secid       mid     eosid      hgid      grav    adpopt      tmid
       111        12        20         0         0         0         0         0
*PART
$#                                                                    title
```

```
TEK_Screws_Symmetry
$#     pid     secid       mid     eosid      hgid      grav    adpopt      tmid
       112        13        12         0         0         0         0         0
*PART
$#                                                                         title
TEK_Screws_Full
$#     pid     secid       mid     eosid      hgid      grav    adpopt      tmid
       113        13        13         0         0         0         0         0
*PART
$#                                                                         title
Bolts
$#     pid     secid       mid     eosid      hgid      grav    adpopt      tmid
       116        24         7         0         0         0         0         0
*PART
$#                                                                         title
W12X14.web
$#     pid     secid       mid     eosid      hgid      grav    adpopt      tmid
       122        23        15         0         0         0         0         0
*PART
$#                                                                         title
W12X14.flange
$#     pid     secid       mid     eosid      hgid      grav    adpopt      tmid
       123        22        15         0         0         0         0         0
$#########################################################################################
$                                      SECTIONS
$#########################################################################################
*SECTION_SOLID_TITLE
Steel_Tetrahedron.Elements
$#   secid    elform       aet
         1        10         0
*SECTION_SOLID_TITLE
Slab_8 Noded Elements
$#   secid    elform       aet
         2         1         0
*SECTION_SOLID_TITLE
bolts
$#   secid    elform       aet
        24        10         0
*SECTION_BEAM_TITLE
Shear Studs
$#   secid    elform      shrf   qr/irid       cst     scoor       nsm
         3         1  1.000000         2         1     0.000     0.000
$#     ts1       ts2       tt1       tt2     nsloc     ntloc
 12.700000 12.700000     0.000     0.000     0.000     0.000
*SECTION_BEAM_TITLE
Shear Studs_Symmetry
$#   secid    elform      shrf   qr/irid       cst     scoor       nsm
         4         1  1.000000         2         1     0.000     0.000
$#     ts1       ts2       tt1       tt2     nsloc     ntloc
  9.000000  9.000000     0.000     0.000     0.000     0.000
*SECTION_SHELL_TITLE
Deck
```

```
$#   secid     elform      shrf       nip     propt   qr/irid     icomp     setyp
         5          2  1.000000         4         1         0         0         1
$#      t1         t2        t3        t4      nloc     marea      idof    edgset
  0.762000   0.762000  0.762000  0.762000     0.000     0.000     0.000         0
*SECTION_SHELL_TITLE
Girder.Web
$#   secid     elform      shrf       nip     propt   qr/irid     icomp     setyp
        23          4  1.000000         4         1         0         0         1
$#      t1         t2        t3        t4      nloc     marea      idof    edgset
  2.540000   2.540000  2.540000  2.540000     0.000     0.000     0.000         0
*SECTION_SHELL_TITLE
Girder.Flange
$#   secid     elform      shrf       nip     propt   qr/irid     icomp     setyp
        22          4  1.000000         4         1         0         0         1
$#      t1         t2        t3        t4      nloc     marea      idof    edgset
  5.700000   5.700000  5.700000  5.700000     0.000     0.000     0.000         0
*SECTION_BEAM_TITLE
WWM
$#   secid     elform      shrf   qr/irid       cst     scoor       nsm
        11          1  1.000000         2         1     0.000     0.000
$#     ts1        ts2       tt1       tt2     nsloc     ntloc
  3.175000   3.175000     0.000     0.000     0.000     0.000
*SECTION_BEAM_TITLE
Negative_Moment_Bars
$#   secid     elform      shrf   qr/irid       cst     scoor       nsm
        12          1  1.000000         2         1     0.000     0.000
$#     ts1        ts2       tt1       tt2     nsloc     ntloc
  9.525000   9.525000     0.000     0.000     0.000     0.000
*SECTION_BEAM_TITLE
TEK_Screws
$#   secid     elform      shrf   qr/irid       cst     scoor       nsm
        13          6  1.000000         2         1     0.000     0.000
$#     vol       iner       cid        ca    offset     rrcon     srcon     trcon
 300.00000 1.7000E-5         0     0.000     0.000     0.000     0.000     0.000
*END
```

REFERENCES

[1] Hallquist, J. (2013). *LS-DYNA keyword user's manual, Version R7.0*, Livermore, California.

[2] Hewitt, C. M. (2006). "Simpler Shear Connections." *Modern Steel Construction*, American Institute of Steel Construction.

[3] Tamboli, A. R. (2010). *Handbook of Structural Steel Connection Design and Details*, McGraw-Hill, New York.

[4] SDI (2006). *SDI Manual of Steel Construction with Steel Deck*, Steel Deck Institute.

[5] Mullett, D. (1998). *Composite Floor Systems*, Wiley.

[6] Arthur, J., and McGraw-Hill (2005). *Concise Encyclopedia of Engineering*.

[7] FEMA (1996). "The Oklahoma City Bombing: Improving Building Performance Through Multi-Hazard Mitigation." *FEMA 277*, Federal Emergency Management Agency, ed., ASCE, Washington, DC.

[8] Shyam-Sunder, S. (2005). "Final Report on the Collapse of the World Trade Center towers." National Institute of Standards and Technology.

[9] Sozen, M., Thornton, C., Corley, W., and Sr, P. (1998). "The Oklahoma City Bombing: Structure and Mechanisms of the Murrah Building." *Journal of Performance of Constructed Facilities*, 12(3), 120-136.

[10] Wisniewski, B., and Peraza, D. (2008). "Evaluation of Building with Severe Impact Damage: The Banker's Trust Building." *Structures Congress 2008*, American Society of Civil Engineers, 1-7.

[11] FEMA (2002). "World Trade Center Building Performance Study: Data Collection, Preliminary Observations, and Recommendations." *FEMA 403*, Federal Emergency Management Agency, ed.Washington, DC.

[12] DoD (2013). *UFC 4-023-03: Design of Buildings to Resist Progressive Collapse*, Department of Defense, Washington, DC.

[13] GSA (2013). *Alternative Path Analysis & Design Guidelines for Progressive Collapse*, U.S. General Services Administration Washington, DC.

[14] GSA (2003). *Progressive Collapse Analysis and Design Guidelines for New Federal Office Buildings and Major Modernization Projects*, U.S. General Services Administration Washington, DC.

[15] Starossek, U. (2006). "Progressive Collapse of Structures: Nomenclature and Procedures." *Structural Engineering International*, 16(2), 113-117.

[16] Kanno, Y., and Ben-Haim, Y. (2011). "Redundancy and Robustness, or When Is Redundancy Redundant?" *Journal of Structural Engineering*, 137(9), 935-945.

[17] ECS, E. C. f. S. (2006). "EN 1991 - Eurocode 1: Actions on Structures." *Part 1-7: General Actions - Accidental Actions*Brussels.

[18] Sasani, M., Bazan, M., and Sagiroglu, S. (2007). "Experimental and Analytical Progressive Collapse Evaluation of Actual Reinforced Concrete Structure." *ACI Structural Journal*, 104(6), 731-739.

[19] Sasani, M., and Sagiroglu, S. (2010). "Gravity Load Redistribution and Progressive Collapse Resistance of 20-Story Reinforced Concrete Structure following Loss of Interior Column." *ACI Structural Journal*, 107(6), 636-644.

[20] Sasani, M., Kazemi, A., Sagiroglu, S., and Forest, S. (2011). "Progressive Collapse Resistance of an Actual 11-Story Structure Subjected to Severe Initial Damage." *Journal of Structural Engineering*, 137(9), 893-902.

[21] Sasani, M., and Sagiroglu, S. (2008). "Progressive Collapse Resistance of Hotel San Diego." *Journal of Structural Engineering*, 134(3), 478-488.

[22] Sasani, M. (2008). "Response of a Reinforced Concrete Infilled-frame Structure to Removal of Two Adjacent Columns." *Engineering Structures*, 30(9), 2478-2491.

[23] Liu, R., Davison, B., and Tyas, A. (2005). "A Study of Progressive Collapse in Multi-Storey Steel Frames." *Structures Congress 2005*, American Society of Civil Engineers, 1-9.

[24] Giriunas, K. A., and Sezen, H. (2011). "Progressive Collapse Analysis of an Existing Building." *The Journal of Undergraduate Research at Ohio State*, 1(40).

[25] Song, B. I., and Sezen, H. (2013). "Experimental and Analytical Progressive Collapse Assessment of a Steel Frame Building." *Engineering Structures*, 56(0), 664-672.

[26] Xiao, Y., Zha, Y. B., Li, F. W., Kunnath, S. K., and Lew, H. S. "Collapse Test of a 3-story Half-Scale RC Frame Structure." *Proc., Structures Congress 2013*, 11-19.

[27] Chen, J., Huang, X., Ma, R., and He, M. (2011). "Experimental Study on the Progressive Collapse Resistance of A Two-storey Steel Moment-frame." *Journal of Performance of Constructed Facilities*.

[28] Sasani, M., and Kropelnicki, J. (2008). "Progressive collapse analysis of an RC structure." *The Structural Design of Tall and Special Buildings*, 17(4), 757-771.

[29] Tsai, M.-H., and Huang, T.-C. (2013). "Progressive collapse analysis of an RC building with exterior partially infilled walls." *The Structural Design of Tall and Special Buildings*, 22(4), 327-348.

[30] Yu, J., and Tan, K.-H. (2013). "Experimental and Numerical Investigation on Progressive Collapse Resistance of Reinforced Concrete Beam Column Sub-Assemblages." *Engineering Structures*, 55(0), 90-106.

[31] Yi, W.-J., He, Q.-F., Xiao, Y., and Kunnath, S. K. (2008). "Experimental Study on Progressive Collapse-Resistant Behavior of Reinforced Concrete Frame Structures." *ACI Structural Journal*, 105(4), 433-439.

[32] Sadek, F. H., Main, J. A., Lew, H. S., and Bao, Y. (2011). "Testing and Analysis of Steel and Concrete Beam-Column Assemblies under a Column Removal Scenario." *Journal of Structural Engineering*, 137(9), 881-892.

[33] Kai, Q., and Li, B. (2012). "Dynamic Performance of RC Beam-Column Substructures Under the Scenario of the Loss of a Corner Column—Experimental Results." *Engineering Structures*, 42(0), 154-167.

[34] Tsitos, A. (2009). "Experimental and Numerical Investigation of the Progressive Collapse of Steel Frames." PhD, University of Buffalo, Buffalo, NY.

[35] Sadek, F. H., Main, J. A., Lew, H. S., Robert, S. D., Chiarito, V. P., and El-Tawil, S. (2010). "An Experimental and Computational Study of Steel Moment Connections under a Column Removal Scenario." *NIST Technical Note 1669*, National Institute of Standards and Technology.

[36] Guo, L., Gao, S., Fu, F., and Wang, Y. (2013). "Experimental Study and Numerical Analysis of Progressive Collapse Resistance of Composite Frames." *Journal of Constructional Steel Research*, 89(0), 236-251.

[37] Weigand, J., and Berman, J. (2013). "Integrity of Steel Single Plate Shear Connections Subjected to Simulated Column Removal." *Journal of Structural Engineering*, 140(5), 04013114.

[38] Yang, B., and Tan, K. H. (2013). "Robustness of Bolted-Angle Connections Against Progressive Collapse: Mechanical Modelling of Bolted-Angle Connections Under Tension." *Engineering Structures*, 57(0), 153-168.

[39] Williamson, E., and Stevens, D. (2009). "Modeling Structural Collapse Including Floor Slab Contributions." *Structures Congress 2009*, American Society of Civil Engineers, 1-9.

[40] Alashker, Y., Li, H., and El-Tawil, S. (2011). "Approximations in Progressive Collapse Modeling." *Journal of Structural Engineering*, 137(9), 914-924.

[41] Park, R. (1964a). "Tensile Membane Behavior of Uniformly Loaded Rectangular Reinforced Concrete Slabs with Fully Restrained Edges." *Magazine of Concrete Research*, 16(46), 39-44.

[42] Park, R. (1964b). "Ultimate Strength of Rectangular Concrete Slabs Under Short-Term Uniform Loading with Edges Restrained Against Lateral Movement." *ICE Proceedings*, 125-150.

[43] Mitchell, D., and Cook, W. (1984). "Preventing Progressive Collapse of Slab Structures." *Journal of Structural Engineering*, 110(7), 1513-1532.

[44] Yi, W., Zhang, F., and Kunnath, S. (2014). "Progressive Collapse Performance of RC Flat Plate Frame Structures." *Journal of Structural Engineering*, 140(9), 04014048.

[45] Li, H., and El-Tawil, S. (2012). "Role of Composite Action in Collapse Resistance of Steel Frame Buildings." *Structures Congress 2012*, American Society of Civil Engineers, 225-234.

[46] Foley, C. M., Martin, K., and Schneeman, C. (2007). "Robustness in Structural Steel Framing Systems." American Institute of Steel Construction, Inc., Chicago, IL, 273.

[47] Sadek, F. H., El-Tawil, S., and Lew, H. S. (2008). "Robustness of Composite Floor Systems with Shear Connections: Modelling, Simulation, and Evaluation." *Journal of Structural Engineering*, 134(11), 1717-1725.

[48] Alashker, Y., El-Tawil, S., and Sadek, F. H. (2010). "Progressive Collapse Resistance of Steel-Concrete Composite Floors." *Journal of Structural Engineering*, 136(10), 1187-1196.

[49] Tan, S., and Astaneh-Asl, A. (2003). "Cable-Based Retrofit of Steel Building Floors to Prevent Progressive Collapse." University of California at Berkeley, Berkeley, CA.

[50] Johnson, E. S. (2014). "Large-Scale Testing of a Steel-Concrete Composite Floor System Under Column Loss Scenarios." Master of Science, University of Illinois at Urbana-Champagn, Urbana, Illinois.

[51] Mohamed, O. (2006). "Progressive Collapse of Structures: Annotated Bibliography and Comparison of Codes and Standards." *Journal of Performance of Constructed Facilities*, 20(4), 418-425.

[52] ASCE (2007). "Seismic rehabilitation of existing buildings." America Society of Civil Engineers, Reston, VA.

[53] Stevens, D., Crowder, B., Sunshine, D., Marchand, K., Smilowitz, R., Williamson, E., and Waggoner, M. (2011). "DoD Research and Criteria for the Design of Buildings to Resist Progressive Collapse." *Journal of Structural Engineering*, 137(9), 870-880.

[54] Arup (2011). "Review of International Research on Structural Robustness and Disproportionate Collapse." Centre for the Protection of National Infrastructure (CPNI).

[55] ASCE (2010). "Minimum Design Loads for Buildings and Other Structures, ASCE/SEI 7-10." American Society of Civil Engineers, Virginia.

[56] AISC (2005). "Specification for Structural Steel Buildings." American Institute of Steel Construction, Inc, Chicago, IL.

[57] Fisher, J. M., and West, M. A. (1990). *Design Guide 3: Serviceability Design Considerations for Low-rise Buildings*, American Institute of Steel Construction, Chicago, IL.

[58] Murray, T. M., Allen, D. E., and Ungar, E. E. (1997). *Deisgn Guide 11: Floor Vibrations Due to Human Activity*, American Institute of Steel Construction, Chicago, IL.

[59] Hoffman, S. T., and Fahenstock, L. A. (2011). "Behavior of Multi-Story Steel Buildings Under Dynamic Column Loss Scenarios." *Steel and Composite Structures*, 11(2), 149-168.

[60] Alashker, Y., and El-Tawil, S. (2011). "A Design-Oriented Model for the Collapse Resistance of Composite Floors Subjected to Column Loss." *Journal of Constructional Steel Research*, 67(1), 84-92.

[61] Daneshvar, H., and Driver, R. (2011). "Behavior of Shear Tab Connections under Column Removal Scenario." *Structures Congress 2011*, American Society of Civil Engineers, 2905-2916.

[62] Bailey, C. G. (2001). "Membrane Action of Unrestrained Lightly Reinforced Concrete Slabs at Large Displacements." *Engineering Structures*, 23(5), 470-483.

[63] Chen, S., and Shi, X. (2011). "Discussion of "Progressive Collapse Resistance of Steel-Concrete Composite Floors" by Yasser Alashker, Sherif El-Tawil, and Fahim Sadek." *Journal of Structural Engineering*, 137(12), 1627-1628.

[64] Vulcraft (2008). "Vulcraft Steel Roof & Floor Deck." A Division of Nucor Corporation, ed.

[65] Starossek, U. (2007). "Typology of Progressive Collapse." *Engineering Structures*, 29(9), 2302-2307.

[66] Hull, L. A. (2013). "Experimental Testing of a Steel Gravity Frame with a Composite Floor Under Interior Column Loss." Master of Science in Engineering, The University of Texas at Austin, Austin.

[67] Moutsanidis, G. (2014). "Progressive Collapse Resistance of Steel-Framed Structures with Composite Floor Systems." Master of Science in Engineering, The University of Texas at Austin, Austin, TX.

[68] Lewitt, C. W., Chesson Jr., W. H., and Munse, W. H. (1966). "Restraint Characteristics of Flexible Riveted and Bolted Beam-to-Column Connections." University of Illinois, College of Engineering, Urbana, Illinois.

[69] AISC (2014). *Steel Construction Manual*, American Institute of Steel Construction, INC., Chicago, IL.

[70] Guanyu, H. (2011). "Behavior of Beam Shear Connections in Steel Buildings Subject to Fire." PhD, The University of Texas at Austin, Austin.

[71] ASTM (2012). "Standard Test Methods and Definitions for Mechanical Testing of Steel Products." American Society for Testing and Materials, West Conhohocken, PA.

[72] Beer, F., Johnson, R., Dewolf, J., and Mazurek, D. (2011). *Mechanics of Materials*, McGraw-Hill New York.

[73] Main, J. A., and Sadek, F. H. (2011). "Modelling of Bolted Connections for Collapse Analysis of Steel Structures." *14th International Symposium on Interaction of the Effects of Munitions with Structures*Seattle, WA.

[74] Murray, Y. D. (2007). "Users Manual for LS-DYNA Concrete Material 159." 89.

[75] Gere, J., and Goodno, B. (2012). *Mechanics of Materials*, Cengage Learning.

[76] (2015). *LS-DYNA Theory Manual*, Livemore, CA.

[77] ASTM (2014). "Standard Test Method for Compressive Strength of Cylindrical Concrete Specimens." American Society for Testing and Materials, West Conhohocken, PA.

[78] ASTM (2008). "Standard Test Methods of Tension Testing of Metallic Foil." American Society for Testing and Materials, West Conshohocken, PA.

[79] ECS, E. C. f. S. (2005). "EN 1993 - Eurocode 3: Design of Steel Structures."Brussels.

[80] Nelson (2010). "General Material Spefications." Nelson Stud Welding, ed.

[81] Kulak, G. L., Fisher, J. W., and Struik, J. H. A. (2001). *Guide to Design Criteria for Bolted and Riveted Joints*, American Institute of Steel Construction, Chicago, IL.

[82] Lee, J. (2012). "Elevated-Temperature Properties of ASTM A992 Steel for Structural-Fire Engineering Analysis." Ph.D, The University of Texas at Austin, Austin, TX.

VITA

Michalis Hadjioannou grew up in Nicosia, Cyprus with his parents, Panikos and Eleni. After graduating from Apostolos Varnavas Lyceum, he attended the National University of Athens, Greece and received Diploma in Civil Engineering with focus in Structural Engineering in 2010. After graduation, he came to The University of Texas at Austin to work as a Teaching Assistant and as a Graduate Research Assistant at the Phil M. Ferguson Structural Engineering Laboratory. He received a Master's of Science in Structural Engineering in 2012. His PhD was completed in 2015.

Permanent email: hadjioannou.m@gmail.com

This dissertation was typed by the author.